
EXPERIMENTAL AND ANALYTICAL DEMONSTRATION OF INERTIAL AMPLIFIER CONCEPTS

Emily Georgina Nar (BEng)



Swansea University
Prifysgol Abertawe
College of Engineering
Coleg Peirianeg

Submitted to Swansea University in fulfilment of the requirements for the Degree of
Master of Science by Research

May 2023

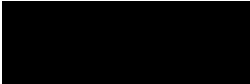
Copyright: The Author, Emily G. Nar, 2023.

Abstract

An inertial amplifier is a dynamic tuning device, which works to increase the effective mass of a resonator without proportionally augmenting the physical mass of the system. This thesis presents six inertial amplifier mechanisms, namely the single-stage, single-stage truss, compound, compound truss, nested, and nested truss inertial amplifiers. The configuration of each inertial amplifier is conceived through a series of link-bar mechanisms. Based on the configurations of each inertial amplifier, the kinematic relationships and the equations of motion are derived. The analytical analysis demonstrates that through geometrical adjustments, and proof mass alterations to each system, it is possible to manipulate the effective mass of each system, respectively. To support the analytical analysis, an experimental demonstration of each inertial amplifier is provided, whereby a series of electrodynamic shaker tests are conducted. These tests assess the pure mass effects of each inertial amplifier, the behaviour of a cantilever beam, and the impact of the single-stage, single-stage truss, compound and compound truss inertial amplifiers on the dominant single-degree-of-freedom mode of the cantilever beam. Through frequency response plots it is shown that the single-stage, single-stage truss, compound, and compound truss inertial amplifiers, all have the ability to enhance the effective mass characteristics of the cantilever beam, thereby causing changes to its the underlying natural frequency, damping ratio, and Q-factor properties. The inertial amplifiers presented in this paper, provide a step improvement for applications that require dynamic tuning.

Declarations and Statements

This work has not previously been accepted in substance for any degree and is not being concurrently submitted in candidature for any degree.

Signed..... 

Date..... *19/05/2023*

This thesis is the result of my own investigations, except where otherwise stated. Other sources are acknowledged by footnotes giving explicit references. A bibliography is appended.

Signed..... 

Date..... *19/05/2023*

I hereby give consent for my thesis, if accepted, to be available for photocopying and for inter-library loan, and for the title and summary to be made available to outside organisations.

Signed..... 

Date..... *19/05/2023*

The University's ethical procedures have been followed and, where appropriate, that ethical approval has been granted.

Signed..... 

Date..... *19/05/2023*

Table of Contents		Page
Acknowledgements		v
List of Figures		v
List of Tables		x
Abbreviations		xi
Nomenclature		xii
Keywords		xiii
1. Introduction		1
1.1 Background		1
1.2 Aim		5
1.3 Methodology		6
1.4 Contributions.....		6
1.5 Paper Outline		7
2. Applications of a Tunable Mass Inertial Amplifier.....		7
2.1 Atomic Force Microscopy		7
2.1.1 AFM Imaging Modes		9
2.1.2 Applications of an AFM.....		9
2.1.3 Tunable Mass Amplifier for an AFM.....		9
2.2 Vibration-Based Energy Harvesting.....		12
2.2.1 Transduction Mechanisms for a VBEH.....		12
2.2.1.1 Piezoelectric Transducer.....		13
2.2.1.2 Electrostatic Transducer		13
2.2.1.3 Electromagnetic Transducer		14
2.2.1.4 Magnetostrictive Transducer		14
2.2.2 Applications for a VBEH		15
2.2.3 Limitations of a VBEH.....		15
2.2.4 Tunable Mass Amplifier for a VBEH.....		16
3. Equations of Motion for the proposed IA Mechanisms.....		17
3.1 Single-Stage Inertial Amplifier		18
3.1.1 System Considered and Kinematic Relations.....		18
3.1.2 Lagrangian Analysis of the Single-Stage Inertial Amplifier		21
3.1.3 Linearised Equation of Motion for the Single-Stage Inertial Amplifier.....		27
3.2 Compound Inertial Amplifier.....		28
3.2.1 System Considered and Kinematic Relations.....		28
3.2.2 Lagrangian Analysis of the Compound Inertial Amplifier.....		31
3.2.3 Linearised Equation of Motion for the Compound Inertial Amplifier		38

3.3	Nested Inertial Amplifier	39
3.3.1	System Considered and Kinematic Relations	39
3.3.2	Lagrangian Analysis of the Nested Inertial Amplifier.....	43
3.3.3	Linearised Equation of Motion for the Nested Inertial Amplifier	47
4.	Design, Manufacturing and Assembly Process	48
4.1	Component Parts of Each Inertial Amplifier	50
4.1.1	Arms	50
4.1.2	Deep Groove Ball Bearings	55
4.1.3	Pins	56
4.1.4	Brackets	58
4.1.5	Cantilever Beam	59
4.1.6	Proof Mass.....	61
4.2	Assembly.....	62
5.	Experimental Analysis of the Inertial Amplifiers.....	65
5.1	Experimental Set-up.....	66
5.2	Experimental Results	70
5.2.1	Pure Mass Inertial Amplifier Tests.....	70
5.2.1.1	Single-Stage Inertial Amplifier.....	70
5.2.1.2	Single-stage Truss Amplifier	73
5.2.1.3	Compound Inertial Amplifier	75
5.2.1.4	Compound Truss Inertial Amplifier	78
5.2.1.5	Nested Inertial Amplifier.....	80
5.2.1.6	Nested Truss Inertial Amplifier.....	82
5.2.2	Cantilever Beam	84
5.2.3	Inertial Amplifier Coupled to a Cantilever Beam.....	87
5.2.3.1	Single-Stage Inertial Amplifier Coupled to a Cantilever Beam	87
5.2.3.2	Single-Stage Inertial Amplifier Coupled to a Cantilever Beam with Tip Mass	90
5.2.3.3	Single-Stage Inertial Amplifier with Joint Mass Coupled to a Cantilever Beam.....	91
5.2.3.4	Single-Stage Truss Inertial Amplifier Coupled to a Cantilever Beam	94
5.2.3.5	Single-Stage Truss Inertial Amplifier Coupled to a Cantilever Beam with Tip Mass.....	96
5.2.3.6	Single-Stage Truss Inertial Amplifier with Joint Mass Coupled to a Cantilever Beam	98
5.2.3.7	Compound Inertial Amplifier Coupled to a Cantilever Beam.....	100

5.2.3.8	Compound Inertial Amplifier Coupled to a Cantilever Beam with Tip Mass	103
5.2.3.9	Compound Inertial Amplifier with Joint Mass Coupled to a Cantilever Beam	105
5.2.3.10	Compound Truss Inertial Amplifier Coupled to a Cantilever Beam	108
5.2.3.11	Compound Truss Inertial Amplifier Coupled to a Cantilever Beam with Tip Mass	110
5.2.3.12	Compound Truss Inertial Amplifier with Joint Mass Coupled to a Cantilever Beam	112
6.	Discussion	114
6.1	Limitations	120
6.2	Future Work	121
7.	Conclusion	122
8.	Appendix	124
8.1	Equations	124
8.2	Natural frequency, damping ratio, and Q-factor characteristics for each system shown in Subsections 5.2.1 and 5.2.3	130
9.	Bibliography	132

Acknowledgements

The author would like to thank her academic supervisors – Doctor Alexander Shaw of Swansea University and Professor Sondipon Adhikari of the University of Glasgow. The expertise and guidance offered have been a key driving force in achieving novel outcomes.

List of Figures

Figure 1:	A schematic diagram of the classical inerter – A flywheel gear mechanism [35]	4
Figure 2:	A Schematic diagram showing a) the single-stage IA, b) the compound IA, and c) the nested IA. Where m is the loaded mass, θ signifies the amplifier angle of the mechanism, and x and z denote the directions of displacement for the IA. Note that a subscript 1, 2, or 3, following a variable indicates its association with a specific sub-mechanism	6
Figure 3:	A schematic diagram of the basic AFM system, modified from [63]	8

Figure 4: a) The single-stage inertial amplifier, showing relative displacements. b) One-half of the single-stage inertial amplifier. c) Coupling to a mass-spring system. d) Coupling to a general finite element structure.....	19
Figure 5: a) Effective mass as a function of the displacement z for the single-stage IA. b) Non-linear velocity coefficient as a function of the displacement z for the single-stage IA. Six different values for the initial amplifier angle \emptyset are shown in each plot.....	26
Figure 6: Conversion of the compound inertial amplifier into one-half system.....	29
Figure 7: a) Effective mass as a function of the displacement z for the compound IA. b) non-linear velocity coefficient as a function of the displacement z for the compound IA. Six different values for the initial amplifier angle of the primary mechanism \emptyset_1 are shown in each plot.....	37
Figure 8: Conversion of the nested inertial amplifier to one-half system.....	41
Figure 9 a) Effective mass as a function of the displacement z for the nested IA. b) Non-linear velocity coefficient as a function of the displacement z for the nested IA. Six different values for the initial amplifier angle \emptyset are shown in each plot.....	46
Figure 10: A flowchart outlining the design process followed to model each IA.....	49
Figure 11: a) One outer arm of the single-stage, compound and nested IAs. b) One outer arm of the single-stage truss, compound truss and nested truss IAs.....	52
Figure 12: a) One short arm of the compound IA. b) One short arm of the compound truss IA.....	52
Figure 13: a) One long arm of the compound IA. b) One long arm of the compound truss IA.....	53
Figure 14: a) One secondary arm of the nested IA. b) One secondary arm of the nested truss IA.....	54
Figure 15: a) One tertiary arm of the nested IA. b) One tertiary arm of the nested truss IA....	54
Figure 16: a) An image which indicates the width of a 694ZZ deep groove ball bearing. b) An image which shows the inner and outer diameters of a 694ZZ deep groove ball bearing.....	55
Figure 17: A 4mm diameter ABS pin, which is used to form each joint in each IA.....	57
Figure 18: CAD model of the designed bracket, with the part dimensions specified.....	59
Figure 19: A CAD model of the cantilever beam used in this work, with the dimensions explicitly defined.....	60
Figure 20: An image of one 12g circular lead disk, with a diameter of 25mm [125].....	62
Figure 21: a) A front view CAD assembly model of the single-stage IA attached to a cantilever beam. b) A side view CAD assembly model of the single-stage IA. c) A front view CAD assembly model of the single-stage truss IA.....	64

Figure 22: a) A front view CAD assembly model of the compound IA affixed to a cantilever beam. b) A side view CAD assembly model of the compound IA. c) A front view CAD assembly model of the compound truss IA.....	64
Figure 23: a) A front view CAD assembly model of the nested IA affixed to a cantilever beam. b) A side view CAD assembly model of the nested IA. c) A front view CAD assembly model of the nested truss IA.....	65
Figure 24: a) Schematic diagram of the experimental set-up to test each distinct IA. b) Photograph of the experiment for the compound IA.....	68
Figure 25: a) Schematic diagram of the experimental set-up for the cantilever beam. b) Photograph of the experimental set-up for the cantilever beam.....	68
Figure 26: a) Schematic diagram of the experimental setup for each IA coupled to a cantilever beam. b) Photograph of the single-stage IA coupled to a cantilever beam.....	69
Figure 27: A photograph of the single-stage IA with an initial amplifier angle of 20 degrees.....	71
Figure 28a) A frequency response plot of the single-stage IA. b) A coherence plot of the single-stage IA.....	71
Figure 29: A photograph of the single-stage truss IA with an initial amplifier angle of 5 degrees.....	73
Figure 30: a) A frequency response plot of the single-stage truss IA. b) A coherence plot of the single-stage truss IA.....	74
Figure 31: a) A frequency response plot of the compound IA. b) A coherence plot of the compound IA.....	76
Figure 32: a) a) A frequency response plot of the compound truss IA. b) A coherence plot of the compound truss IA.....	78
Figure 33: A photograph of the nested IA with an initial amplifier angle of 25 degrees.....	80
Figure 34: a) A frequency response plot of the nested IA. b) A coherence plot of the nested IA.....	81
Figure 35: a) A frequency response plot of the nested truss IA. b) A coherence plot of the nested truss IA.....	83
Figure 36: A photograph of the cantilever beam with 48g of tip mass attached.....	85
Figure 37: a) A frequency response plot of the cantilever beam. b) A coherence plot of the cantilever beam.....	85
Figure 38: a) A bar chart to show the damping ratio of the cantilever beam for different test conditions. b) A bar chart to show the Q-factor of the cantilever beam for different test conditions.....	86

Figure 39: a) A frequency response plot of the single-stage IA coupled to a cantilever beam.	
b) A coherence plot of the single-stage IA coupled to a cantilever beam.....	88
Figure 40: a) A bar chart to show the damping ratio of the single-stage IA coupled to a cantilever beam, for different test conditions. b) A bar chart to show the Q-factor of the single-stage IA coupled to a cantilever beam, for different test conditions. Note that the cantilever beam is displayed for comparison.....	89
Figure 41: A frequency response plot of the single-stage IA coupled to a cantilever beam with a) 12g, b)24g, c)36g, and d)48g of proof mass added to the tip of the cantilever....	90
Figure 42: a) A bar chart to show a) the damping ratio, and b) the Q-factor of the single-stage IA coupled to a cantilever beam, when 12g, 24g, 36g and 48g of proof mass has been added to the tip of the cantilever.....	91
Figure 43: A photograph of the single-stage IA coupled to a cantilever beam, with 12g of proof mass at each specified joint of the mechanism.....	92
Figure 44: A frequency response plot of the single-stage IA coupled to a cantilever beam with a) 12g, b) 24g, c) 36g, and d) 48g of proof mass added to each specified joint of the mechanism.....	92
Figure 45: a) A bar chart to show a) the damping ratio, and b) the Q-factor of the single-stage IA coupled to a cantilever beam, when 12g, 24g, 36g and 48g of proof mass has been added to each specified joint of the mechanism.....	93
Figure 46: A photograph of the single-stage truss IA with an initial amplifier angle of 20 degrees, coupled to a cantilever beam.....	94
Figure 47: a) A frequency response plot of the single-stage truss IA coupled to a cantilever beam. b) A coherence plot of the single-stage truss IA coupled to a cantilever beam.....	94
Figure 48: A bar chart to show a) the damping ratio, and b) the Q-factor of the single-stage truss IA coupled to a cantilever beam, for different test conditions.....	95
Figure 49: A frequency response plot of the single-stage truss IA coupled to a cantilever beam with a)12g, b)24g, c)36g, and d) 48g of proof mass added to the tip of the cantilever.....	97
Figure 50: A bar chart to show a) the damping ratio, and b) the Q-factor of the single-stage truss IA coupled to a cantilever beam, when 12g, 24g, 36g and 48g of proof mass has been added to the tip of the cantilever.....	98
Figure 51: A frequency response plot of the single-stage truss IA coupled to a cantilever beam with a) 12g, b) 24g, c) 36g, and d)48g of proof mass added to each specified joint of the mechanism.....	99

Figure 52: A bar chart to show a) the damping ratio, and b) the Q-factor of the single-stage truss IA coupled to a cantilever beam, when 12g, 24g, 36g and 48g of proof mass has been added to each specified joint of the mechanism.....	100
Figure 53: A photograph of the compound IA coupled to a cantilever beam.....	101
Figure 54: a) A frequency response plot of the compound IA coupled to a cantilever beam. b) A coherence plot of the compound IA coupled to a cantilever beam.....	101
Figure 55: A bar chart to show a) the damping ratio, and b) the Q-factor of the compound IA coupled to a cantilever beam, for different test conditions.....	102
Figure 56: A frequency response plot of the compound IA coupled to a cantilever beam with a) 12g, b) 24g, c) 36g, and d) 48g of proof mass added to the tip of the cantilever.....	103
Figure 57: A bar chart to show a) the damping ratio, and b) the Q-factor of the compound IA coupled to a cantilever beam, when 12g, 24g, 36g and 48g of proof mass has been added to the tip of the cantilever.....	104
Figure 58: A photograph of the compound IA coupled to a cantilever beam, with 18g of proof mass at each specified joint of the mechanism.....	105
Figure 59: A frequency response plot of the compound IA coupled to a cantilever beam with a) 6g, b) 12g, c) 18g, and d) 24g of proof mass added to each specified joint of the mechanism.....	106
Figure 60: A bar chart to show a) the damping ratio, and b) the Q-factor of the compound IA coupled to a cantilever beam, when 6g, 12g, 18g and 24g of proof mass has been added to each specified joint of the mechanism.....	107
Figure 61: a) A frequency response plot of the compound truss IA coupled to a cantilever beam. b) A coherence plot of the compound truss IA coupled to a cantilever beam.....	108
Figure 62: A bar chart to show a) the damping ratio, and b) the Q-factor of the compound truss IA coupled to a cantilever beam, for different test conditions.....	109
Figure 63: A frequency response plot of the compound truss IA coupled to a cantilever beam with a) 12g, b)24g, c)36g), and d)48g of proof mass added to the tip of the cantilever.....	110
Figure 64: A bar chart to show a) the damping ratio, and b) the Q-factor of the compound truss IA coupled to a cantilever beam, when 12g, 24g, 36g and 48g of proof mass has been added to the tip of the cantilever.....	111
Figure 65: A photograph of the compound truss IA with 18g of proof mass at each specified joint of the mechanism.....	112

Figure 66: A frequency response plot of the compound truss IA coupled to a cantilever beam with a) 6g, b) 12g, c) 18g, and d) 24g of proof mass added to each specified joint of the mechanism.....113

Figure 67: A bar chart to show a) the damping ratio, and b) the Q-factor of the compound truss IA coupled to a cantilever beam, when 6g, 12g, 18g and 24g of proof mass has been added to each specified joint of the mechanism..... 114

Figure 68: A graph to show the natural frequency of the single-stage, single-stage truss, compound, and compound truss IAs when coupled to a cantilever beam, for varying initial amplifier angles.....116

Figure 69: A graph to show a) the damping ratio, and b) the Q-factor of the single-stage, single-stage truss, compound, and compound truss IAs when coupled to a cantilever beam, for varying initial amplifier angles.....117

Figure 70: A graph to show the damping ratio and natural frequency characteristics for each IA coupled to a cantilever beam, corresponding to different initial amplifier angles for each IA and varying quantities of proof mass added to tip of the cantilever.....118

Figure 71: A graph to show a) the damping ratio characteristics, and b) the natural frequency characteristics for each IA when coupled to a cantilever beam, corresponding to different initial amplifier angles and varying quantities of proof mass added to the specified joints of each mechanism.....119

List of Tables

Table 1: A table to show the values for the parameters l_1 and h_1 , for different initial amplifier angles. Six cases are shown..... 25

Table 2: A table to show the values for the parameters l_1 , l_2 , h_1 and w_1 , for different initial amplifier angles of the primary mechanism. Six cases are shown. 36

Table 3: A table to show the values for the parameters l_1 , l_2 , l_3 and h_1 , for different initial amplifier angles. Six cases are shown. 46

Table 4: Pin specifications for the single-stage and single-stage truss IAs 57

Table 5: Pin specifications for the compound and compound truss IAs..... 57

Table 6: Pin specifications for the nested and nested truss IAs 57

Table 7: A Table to show the analytical magnitude of response values, for the single stage IA with different initial amplifier angles. 72

Table 8: A Table to show the analytical magnitude of response values, for the single stage truss IA with different initial amplifier angles.	75
Table 9: A Table to show the analytical magnitude of response values, for the compound IA with different initial amplifier angles.	77
Table 10: A Table to show the analytical magnitude of response values, for the compound truss IA with different initial amplifier angles.	79
Table 11: A Table to show the analytical magnitude of response values, for the nested IA with different initial amplifier angles.	82
Table 12: A Table to show the analytical magnitude of response values, for the nested truss IA with different initial amplifier angles.	84
Table 13: A table to show the natural frequencies, damping ratios and Q-factor values for each IA coupled to a cantilever beam, corresponding to different initial amplifier angles for each IA and varying quantities of proof mass added to the tip of the cantilever. It is worth noting that the data for the cantilever beam is included for comparative analysis.	130
Table 14: A table to show a comprehensive breakdown of the natural frequencies, damping ratios, and Q-factor values for each IA coupled to a cantilever beam. The table is arranged according to the initial amplifier angles measured for each IA and the varying quantities of proof mass added to each specified joint of the IA. It is worth noting that the data for the cantilever beam is included for comparative analysis.	131

Abbreviations

ABS: acrylonitrile butadiene styrene

AFM: atomic force microscope

CAD: computer aided design

DAVI: dynamic anti-resonant vibration isolator

DVA: dynamic vibration absorber

FEA: finite element analysis

IA: inertial amplifier

Q: quality factor

TMD: tuned mass damper

VBEH: vibration-based energy harvester

3D: three-dimensional

Nomenclature

A : area

b : breadth of the cantilever

β : strength of the magnetic field or velocity squared coefficient

C : capacitance

d : distance

δ : deflection of cantilever

E : young's modulus

ϵ_0 : permittivity of free space

ϵ_r : permittivity of a relative medium

f_n : natural frequency

G : gain

h : height of the cantilever

h_1 : height of each proposed inertial amplifier

h_2 : height of the secondary mechanism for the compound, compound truss, nested and nested truss IAs or height of the tertiary mechanism for the nested and nested truss IAs.

I : second moment of area

k : spring constant (stiffness)

k_1 : first fundamental mode of vibration

L : lagrangian function

l : length

l_1 : length of the outer arms for each proposed inertial amplifier

l_2 : length of the arms of the secondary mechanism for the compound, compound truss, nested and nested truss IAs

l_3 : length of the arms of the tertiary mechanism for the nested and nested truss IAs

m : proof/discrete mass

m^* : effective mass of the cantilever

m_b : proof/discrete mass at joint b of the single-stage and single-stage truss IAs

m_e : proof/discrete mass at joint e of the compound and compound truss IAs

m_f : proof/discrete mass at joint f of the compound and compound truss IAs

m_i : proof/discrete mass at joint i of the nested and nested truss IAs

N : number of loops of coil

Φ : amplifier angle

ϕ_1 : amplifier angle of the primary mechanism for the compound and compound truss IAs

ϕ_2 : amplifier angle of the secondary mechanism for the compound, compound truss, nested and nested truss IAs
 ϕ_3 : amplifier angle of the tertiary mechanism for the nested and nested truss IAs
 Q : quality-factor
 Q^* : effective quality-factor
 q : charge
 ρ : density
 T : kinetic energy
 t : time
 ϑ : magnetic flux
 V : voltage or potential energy
 v : velocity
 w_1 : width of one half of each proposed inertial amplifier or first natural frequency
 w_2 : width of one half of the tertiary mechanism
 x : horizontal displacement
 x_x : horizontal displacement of joint x
 \ddot{y} : second order derivative of the base vibration with respect to time
 \overline{Y}_m : effective mass of each proposed inertial amplifier
 \ddot{z} : acceleration
 z : vertical displacement
 \dot{z} : velocity
 z_x : vertical displacement of joint x
 \bar{z}_e : vertical distance between joint e and joint b
 \bar{z}_f : vertical distance between joint f and joint b
 \bar{z}_g : vertical distance between joint g and joint b
 \bar{z}_j : vertical distance between joint j and joint b
 ζ : damping coefficient/ratio
 $^\circ$: degrees
 $\%$: percentage

Keywords

Dynamic Response, Effective Mass, Inertial Amplifier, Natural frequency, Single-Degree-of-Freedom System, Vibration Control.

1. Introduction

This work is an attempt to experimentally validate a new class of inertial amplifier (IA) mechanisms. IAs are mechanical devices that provide a magnification of the effective inertia of a resonator.

1.1 Background

Vibrations can cause a variety of unwanted effects. One significant concern relating to vibrations is the potential for structural damage. Over time, vibrations can cause cracks and fractures to buildings, bridges, and other types of structures, leading to a compromise in their safety and stability. In addition, prolonged exposure to vibrations can cause wear and tear of machinery and equipment, leading to premature failure and downtime. Furthermore, vibrations can generate noise which can be irritating and harmful to health. Overall, it is important to be aware of the potential negative effects of vibrations and take measures to mitigate them when possible [1].

Engineers have been seeking methods to reduce unwanted vibrations, particularly from resonances, since the late 1800s. One of the earliest solutions was proposed by Frahm in October 1909 [2]. Frahm invented a passive oscillating device namely a dynamic vibration absorber (DVA), which consists of two key elements, a spring and a mass. The device came to fruition based on the work of Watts in 1883 [3]; Frahm realised that the resonance of an oscillating system could be reduced by coupling a smaller oscillator to the system [4]. The first application of the DVA was to reduce the rolling motion of ships as well as ship hull vibrations [3]. It was shown that the DVA could be extremely effective in reducing the response of an undamped structure, but only at a select tuned frequency [5].

In 1928, Den Hartog and Ormondroyd conducted an analytical optimization study on the DVA [6]. Den Hartog and Ormondroyd proposed that adding a viscous damper to Frahm's device could broaden the frequency range of effectiveness. The inclusion of a damper was thought to slightly increase the bandwidth around the tuned frequency, and also decrease the system's response in mistuned conditions [5]. Soon after the proposal, the concept gained traction, and the DVA evolved into the tuned mass damper (TMD), which consists of three components: a spring, a mass, and a viscous damper. It should be noted that the terminology TMD and DVA are often used synonymously. In 1940, Den Hartog published a book titled 'Mechanical Vibrations', which outlines an approach for finding the optimal tuning and damping

parameters for the TMD [7]. Following that, Brock derived a more simplistic method for the optimal damping ratio [8]. Den Hartog included Brock's derivation in the late edition of 'Mechanical Vibrations' [9]. The theory of the TMD has since been extensively researched, with significant contributions from Thompson [10], Randall et al [11], Warburton [12], Warburton and Ayorinde [13], and Tsai and Lin [14].

Today, the TMD is largely employed across a wide range of engineering fields, including but not limited to civil [15], [16], [17], mechanical [18], [19], wind [20], and aerospace [21], [22]. An example of one of the most famous applications of the TMD is in the Taipei 101 skyscraper [23]. Taipei 101 which stands at 508m, held the record for the tallest building in the world between 2004 and 2008. The building is located in northern Taiwan, 201 meters from a major fault line; this means that adverse weather conditions such as strong winds and earthquakes pose a serious threat to the structure. To help mitigate the effects of such weather conditions, a TMD with a 660-tonne mass element is installed within the upper stories of the building. When external forces influence the TMD, eight steel cables allow the device to sway 5m in any direction. This swaying motion is tuned to the first modal frequency of the building, to cancel out the largest vibrations [4].

The TMD in Taipei 101 has proven to work extremely well [24], albeit the device does suffer from several significant limitations. One limitation is that due to the sharp nature of the resonance peak of a primary system, minor tuning errors result in a rapid loss of performance. Another limitation is that the TMD can only suppress vibrations from one resonance peak in systems with multiple resonances. Aside from these two drawbacks, the requirement for a 660-tonne mass highlights the major flaw of the device. As a structure gets larger or as a greater damping effect is required, then the quantity of mass must increase. This has several implications in terms of cost and interior space within a structure [4].

By exploiting inertial amplification, it is possible to overcome the mass restrictions of the TMD. Inertial amplification employs a mass element that represents a higher mass (effective mass) without actually increasing the physical mass. The concept of inertial amplification was first presented by Flannelly in 1967. Flannelly invented a device called a 'Dynamic Antiresonant Vibration Isolator' (DAVI), to attenuate the vibrations in helicopters [25]. The device furthers a classical mass-spring system, by adding a lever with an isolated tip mass. The lever is interposed between the primary mass of the classical system and the ground. The isolated mass generates an inertial force, which the lever serves to amplify. When the inertial force counteracts the spring force, antiresonance occurs [26]. By lengthening the lever, the

inertial force of the isolated mass increases, which leads to a higher effective mass of the overall system and a shift of the antiresonance frequency, to a lower operating range [27].

Based on Flannelly's concept of inertial amplification, Smith developed a device to advance vibration mitigation. Traditional vibration mitigation methods employ a spring-damper system; however, such a system lacks inertial characteristics [28]. In the spring-damper system, the damper produces a direct proportionality between force and velocity, and the spring produces a direct proportionality between force and the integral of velocity. This means that the spring lags the damper by 90 degrees. By applying a force-current analogy between electrical and mechanical networks, Smith introduced an element namely the 'inertor', that can lead by 90 degrees. The inertor is a mechanical device that generates an inertial force proportional to the acceleration between its two terminals. At the expense of adding the inertor, an additional component to the traditional spring-damper system, significant improvements are demonstrated for vibration isolation [29], [30], [31] vibration absorption [32], [33], and vibration suppression [34] applications [35].

The inertor may be configured in a variety of ways, to suit a broad range of applications. The composition can include pneumatic or hydraulic elements, with concentrated masses and levers, or a combination of racks, pinions, gears, and inertia flywheels [36]. It is worth highlighting that an alteration in the composition and/or amalgamation of components will provide a tunable effective mass. The classical inertor utilised a flywheel gear mechanism, which can be seen in Figure 1. Here, the rotating flywheels act as isolated mass elements, that induce a higher mass effect without actually increasing the physical mass. The principle corresponds to the work produced by Flannelly. The classical inertor saw its first practical application in Formula One racing when the device was implemented into an MP4-20 McLaren race car to improve mechanical grip. It was later shown that the inertor can be used in the same context to improve the damping ratio of essential suspension modes [35].

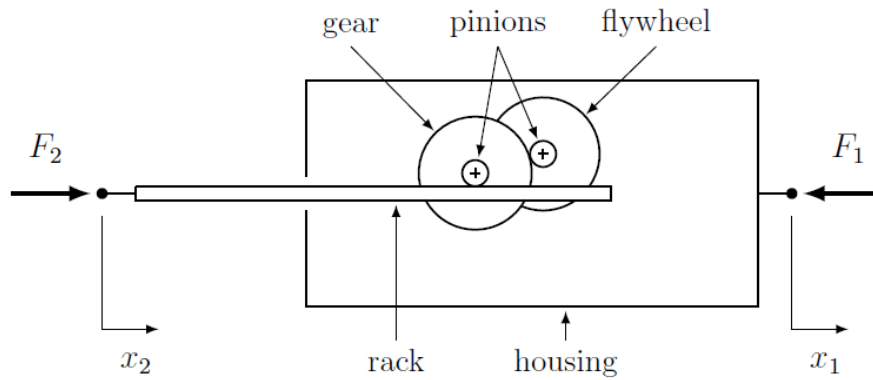


Figure 1: A schematic diagram of the classical inerter – A flywheel gear mechanism [35]

Initial applications of the inerter were in the automotive industry, to reduce the noise and vibrations in automobiles [37], [38]. Since then, the inerter has been applied to improve performance characteristics across a variety of fields. In the rail industry, inerters are used to advance suspension systems [39] as well as pantograph-catenary dynamic performance [40]. Inerters are employed in the aerospace industry to mitigate landing gear shimmy [41] and to further the capabilities of landing gear suspensions [42]. In the civil engineering industry, the inerter is exploited to optimise the seismic resilience of base-isolated buildings [43], [44], and for passive vibration control of structural dynamics applications [45]. More recently the inerter is employed in the marine industry, to dampen tower side-side vibrations in floating offshore wind turbines [46]. The tremendous inertial effects of the inerter are demonstrated to continuously open up new possibilities for engineering applications.

Although extremely successful, the inerter is a complex approach to inertial amplification. A simpler alternative route is through the use of an IA mechanism, which is a dynamic tuning device. Like the inerter, an IA delivers to increase the effective mass of a system, without proportionally augmenting the physical mass of the system [47]. The traditional device structure used to achieve this is a four-link-bar mechanism loaded with symmetric masses. Different from the inerter, IAs are commonly grounded at one end to give a mass-like effect, which is the case in this study. Another variance is that the mass amplification effect results from the geometrical amplification effect of the system.

Mathematically it has been shown that with the passive attachment of an IA, the effective mass of a system can be easily adjusted through variation of the amplifier angle [47], [48]. With current realized systems, it can be much harder to alter the effective mass of the system, an example lies with the ball-screw inerter [49]. To tune mass in the ball screw inerter the flywheel is required to be unthreaded from the system and modified. Thus, the IAs proposed in this work could offer a more practical and more efficient solution for dynamic tuning by mass modification.

In recent years, IAs have been used for vibration absorption and attenuation [50], [51], band gap generation in structured media [52], and to enhance the performance of mechanical systems [53]. Although, all of the work on IAs is purely theoretical, due to the difficulties associated with design, fabrication, and experimental validation. Nonlinearities often exist within IAs, so minor changes to the systems parameters or force values can result in unexpected behavioural outcomes [54]. Furthermore, frictional interfaces are unpredictable, so it is hard to interpret how a structure made up of multiple components will vibrate. Simulation software can handle most physical models, but as model complexity increases an experimental base is required to validate the simulations. Therefore, physical realization and experimental validation of an IA could provide a step improvement for applications that require dynamic tuning.

1.2 Aim

Motivated by the practical boundaries of IAs, the aim of this thesis is to physically realise and experimentally validate six IA mechanisms. Cheng et al [48] pioneered the single-stage IA. The single-stage IA demonstrates how the amplifier angle influences inertial amplification. To enhance the inertial amplification effects of the single-stage IA, Adhikari proposed two IAs with more design freedom namely compound and nested [47]. Adhikari's work demonstrates that, under certain design conditions, it is possible to obtain significantly higher control of the natural frequency of a resonant dynamic system. Based on the work of Cheng et al and Adhikari, the single-stage, compound, and nested IAs will be prototyped and experimentally tested. Figure 2, depicts the device structure for these three IAs. In addition to the aforementioned IAs, three unique truss structure counterparts will be developed: single-stage truss, compound truss, and nested truss. This is to see if an additional design variant can improve dynamic control.

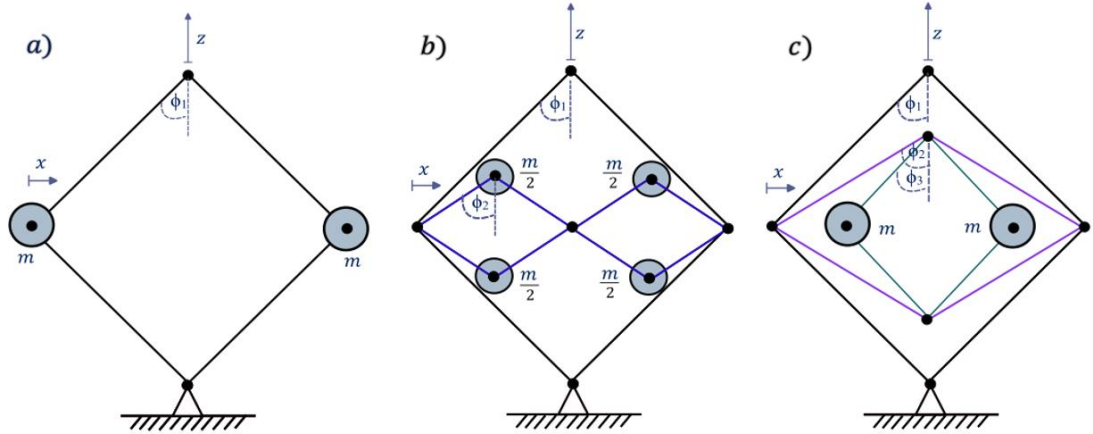


Figure 2: A Schematic diagram showing a) the single-stage IA, b) the compound IA, and c) the nested IA. Where m is the loaded mass, θ signifies the amplifier angle of the mechanism, and x and z denote the directions of displacement for the IA. Note that a subscript 1, 2, or 3, following a variable indicates its association with a specific sub-mechanism.

1.3 Methodology

Each IA will be designed using Solidworks, a 3-dimensional (3D) modelling software. Following the design stage, the models will be manufactured and assembled to form prototypes. The prototypes will then undergo two types of experiment: first, each IA will be directly mounted to a shaker, in order to determine the effective mass of the system; second, each IA will be coupled to a cantilever beam and attached to a shaker, to determine the inertial amplification effects on the dominant single-degree-of-freedom mode. The first mode of vibration for a cantilever beam carries the most energy, so keeping the first mode as the predominant mode, should enhance the energy capture of the underlying dynamics [54]. To exhibit and understand the dynamic behavior of each IA, changes to the isolated mass elements and the amplifier angle will be made for each device.

1.4 Contributions

The thesis makes two main contributions:

1. It offers both a linear and nonlinear analysis for each IA.
2. It provides a novel experimental demonstration for each IA.

1.5 Paper Outline

The work proceeds as follows: In Section 2, two applications that require dynamic tuning are reviewed; in Subsection 2.1 atomic force microscopy (AFM) is discussed and in Subsection 2.2 vibration-based energy harvesting (VBEH) is considered. In Section 3 the single-stage, compound, and nested IAs are presented through Subsections 3.1, 3.2, and 3.3, respectively. Here the systems are explored, and the equations of motion are established using Lagrangian mechanics. In Section 4 the design, manufacturing, and assembly process is stated for each IA and the cantilever beam. In Subsection 4.1, the component parts used to prototype each IA are discussed and in Subsection 4.2 a description of how the parts assemble is given. An experimental demonstration is then applied in Section 5. Dynamic tests are demonstrated on the IAs, the cantilever beam, and both the IAs and the cantilever beam coupled together as one system. In Subsection 5.1 the experimental setup and the decisions leading to the chosen framework are introduced, and in Subsection 5.2 the experimental results are presented. In Section 6 the significance of the raw data is discussed, and interpretations are formed. Finally, in Section 7 conclusions regarding the performance of each IA are drawn, and a general summary is offered.

2. Applications of a Tunable Mass Inertial Amplifier

Numerous applications necessitate dynamic tuning through mass modification. For instance, atomic force microscopy [55], vibration-based energy harvesting [56], machine milling [57], [58], mechanical gearbox resonances [59], and wave energy converters[60]. With the passive attachment of a tunable mass inertial amplifier, dynamic performance characteristics could be improved for these applications. In this Section, the applications atomic force microscopy and vibration-based energy harvesting will be reviewed. An overview of each application will be presented, followed by an explanation of how a tunable mass inertial amplifier could improve their performances.

2.1 Atomic Force Microscopy

The atomic force microscope (AFM) is a highly advanced imaging instrument, invented in 1986 by Gerd Binnig, Calvin. F Quate and Christopher Gerber [61]. The technology facilitates the visualisation and quantification of a materials surface structure down to the nanometre scale. Moreover, the method is versatile in its capability, allowing users to analyse all material types in gas, liquid, and vacuum environments [62]. Figure 3 depicts the general configuration of an AFM.

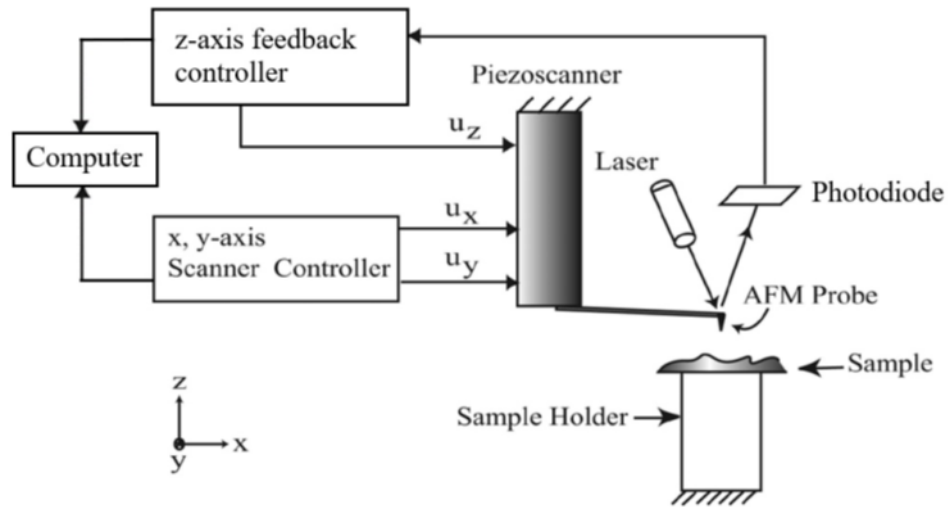


Figure 3: A schematic diagram of the basic AFM system, modified from [63].

The probe is the heart of an AFM, it consists of two fundamental components: a cantilever beam, and a very sharp tip. The behaviour of the cantilever beam is considered dynamically equivalent to an elastic spring, making the force generated through cantilever-tip-sample interactions directly proportional to the cantilever deflection. This relationship is described by Hooke's law [64].

$$F = k\delta \quad 1$$

Where F is the cantilever-tip-sample force, k is the spring constant (stiffness) of the cantilever, and δ is the deflection of the cantilever. Any bumps or depressions on the surface of a sample will alter the deflection of the cantilever. The instrumentation used to sense the deflection is traditionally a laser component and a four-quadrant photodiode. The photodiode tracks and records the movement of a laser beam that is reflected from the flat top of the cantilever. To monitor and control the deflections of the cantilever, a feedback system is used in real-time. Within the control system, signals from the photodiode are fed to drive the z position of a piezoelectric scanner, and a separate scanner system is used to drive the x and y directions of the piezoelectric scanner. Note that the piezoelectric scanner is secured to the fixed end of the cantilever beam, thus influencing its position. Simultaneous to this process, the signals from the photodiode and the scanner system are fed into a computer, allowing all raw data to be

captured. The raw data can be processed to offer a visual image of a materials topography [65], [66].

2.1.1 AFM Imaging Modes

An AFM has three operational modes: contact, tapping, and non-contact. Each mode varies in the nature of the tip-sample interaction [62]. In contact mode, the tip maintains constant contact with the sample surface, in tapping mode, the tip intermittently touches the sample surface and in non-contact mode, the tip is always kept at a short distance away from the sample surface [67]. The chosen mode of operation is dependent on the application and subject matter.

2.1.2 Applications of an AFM

Applications of an AFM can be divided into three main areas: imaging, measuring properties, and structural manipulation. An AFM can image all material types, ranging from metals [68], [69], polymers [70], [71], ceramics [72], [73], to biomolecules [74], [75] and cells [76], [77]. Users can determine both physical characteristics like size, morphology, and surface texture, as well as local mechanical properties such as strength, ductility, hardness, and fracture toughness of these materials [78]. Different AFM modes can be utilised to establish different sample properties. For example, in tapping mode, measuring the phase of the cantilever with respect to the driving signal can provide adhesion and stiffness properties [79], and in non-contact mode sample hardness properties can be obtained [80]. An AFM can also manipulate structures by adjusting the tip-sample force, modifying energy barriers for atom positioning [81], [82]. This contributes to the exploration of the fundamental properties of matter.

2.1.3 Tunable Mass Amplifier for an AFM

While the AFM is a highly advanced imaging device, which exceeds the capabilities of any other imaging instrument, it is not without a major limitation. There is an inherent trade-off between scanning speed and imaging resolution when operating in tapping mode [83]. In atomic force microscopy, tapping mode emerges as the predominant operational mode, as it combines the merits of both contact and non-contact modes.

In this thesis six IAs are proposed which have the potential to provide a control strategy to overcome the trade-off between high scanning speeds and high imaging resolution. This control strategy involves dynamic tuning through effective mass modification. However, before exploring how the IAs can address the trade-off in atomic force microscopy, it is important to understand how a high scanning speed can be achieved. For this, the response of the AFM probe must be analyzed, which can be expressed in terms of its bandwidth as follows:

$$f_{n_2} - f_{n_1} = \frac{f_n}{Q} \quad 2$$

Where $f_{n_2} - f_{n_1}$ is the bandwidth (difference between the upper and lower half power frequencies) of the cantilever, f_n is the natural frequency response of the cantilever measured in Hz, and Q is the quality (Q)-factor of the cantilever. Note that the Q-factor is a measure of the sharpness of the resonance peak in the cantilever's response. In many cases, an AFM cantilever can be approximated as a linear harmonic oscillator, therefore the Q-factor is inversely proportional to the damping ratio ζ of the cantilever.

$$Q = \frac{1}{2\zeta} \quad 3$$

To obtain a high scan speed, the cantilever is required to have a high bandwidth, as a high bandwidth provides superior stability margins of the z-axis feedback loop. Greater stability margins of the z-axis feedback loop expedite the tracking of sample features. Since the bandwidth of the cantilever is inversely proportional to its Q-factor, it is possible to achieve a high scan speed by lowering the Q-factor [55]. However, in tapping mode, a reduction in the Q-factor leads to a decline in force sensitivity, which ultimately results in a lower image resolution. Furthermore, a low Q-factor cantilever generates a large amount of tapping force, which can cause image distortion through both sample and probe damage. This trade-off is the key driving force for research in Q-factor control of AFM cantilevers [55].

The ideal Q-factor for an AFM cantilever depends on the specific application. To determine the optimal value, it is important to consider not only the impact of the cantilevers Q-factor on the operational AFM mode, but also any factors that might influence its dynamic nature such as environmental influence. For instance, when operating in an ultra-high vacuum, the cantilever's Q-factor is significantly increased due to the absence of damping by atmospheric air [84]. Thus, the approach taken to alter the Q-factor of the AFM cantilever should be easily adaptable to accommodate the needs of different applications.

The IAs prototyped and experimentally analysed in this thesis have the potential to contribute to the Q-factor control of AFM cantilevers. The IAs are designed to tune the effective mass of a dynamic system upon passive attachment. In this work the dynamic system used to demonstrate the capabilities of each IA is a cantilever beam. It is widely acknowledged that altering the effective mass of a dynamic system will in turn modify its natural frequency. As natural frequency and Q-factor characteristics are inversely proportional, effective mass modifications will lead to Q-factor alterations. The effective mass of the cantilever will primarily be controlled by adjusting the initial amplifier angle of each IA. The initial amplifier angle of the device is the angle measured between the vertical plane of symmetry of the mechanism and the axis of the adjoining rigid arm when stationary.

Applying the IAs to a cantilever will provide valuable insights on how alterations to the geometry of each IA could impact the Q-factor of an AFM probe. The IAs could be passively attached to the microscope between the fixed end of the AFM cantilever and the piezoelectric scanner. As the z-position of the scanner changes, it will consequently adjust the initial amplifier angle of the chosen IA, influencing both the effective mass and Q-factor characteristics of the probe. Such dynamic tuning could optimize the Q-factor for specific application requirements. For example, scenarios involving intricate surface features, a slower scanning speed and enhanced image resolution may be preferred, while faster scanning speeds could suffice for other situations. Therefore, passive Q-factor control, could effectively help manage the trade-off between scanning speed and imaging resolution in atomic force microscopy.

Active Q-factor control is the current approach employed to tune the effective Q factor of an AFM cantilever operating in tapping mode. The effective Q-factor characterizes how effectively the AFM cantilever responds to external forces and maintains resonance under the influence of active control. The principle of active Q-factor control is based on the use of velocity feedback, which involves monitoring the velocity of the AFM cantilever's oscillations. As the deflection signal of the cantilever is nearly perfectly sinusoidal, an estimate of the velocity signal can be obtained by electronically adding a 90° phase shift to the signal at resonance [85]. By multiplying the velocity signal by a gain and combining it with the drive signal, the effective Q-factor of the cantilever can be adjusted.

The effective Q-factor of the cantilever can be expressed as [86]:

$$Q^* = \frac{1}{\left(\frac{1}{Q} + m^* \omega_n\right)} \quad 4$$

Where m^* is the effective mass of the cantilever and G is the gain. The effective Q-factor can be altered by changing the value of the gain, as the gain amplifies or attenuates the velocity signal from the cantilever's oscillations.

To estimate the velocity signal, a controller is needed in the feedback loop. In commercial AFMs, two common controllers are used: time delay and simple differentiator. However, both controllers have limitations. Time delay controllers can lead to spill-over effects at high frequencies, due to a 90° phase shift [87]. Simple differentiator controllers can amplify high-frequency noise in the feedback loop. Both thermal and optical noise affect the active Q-feedback loop [86]. Proposed solutions like positive position feedback, state feedback, resonant, and piezoelectric shunt controllers aim to address these limitations but are complex and challenging to implement. Therefore, the proposed IAs in this work could provide a simpler alternative to Q-factor control for AFM applications, through passive rather than active means.

2.2 Vibration-Based Energy Harvesting.

Energy harvesting has attracted considerable attention over the last decade, evident from the number of product prototypes and publications available [88], [89], [90], [91]. Energy harvesters capture, convert and circulate small amounts of readily available ambient energy (e.g., chemical [92], kinetic [93], solar [94], and thermal [95]) from a host structure into useable electrical energy. The energy is then manipulated to be either used directly or stored for later use. Each ambient energy source requires a different method of conversion, so a range of harvesting devices exist, which vary in terms of design and composition. In this thesis, vibration-based energy harvesters (VBEHs) are of interest.

Residual vibrations from a wide range of sources, including but not limited to household goods [96], moving vehicles [97], and mechanical machinery [98], are continuously discharged into our environment. VBEHs, which can be thought of as simple mass-spring systems [99], scavenge these unwanted vibrations and convert the stored mechanical energy into electrical energy by means of a transduction mechanism.

2.2.1 Transduction Mechanisms for a VBEH

To convert the mechanical energy from a vibration into electrical energy, a transduction mechanism is required. A VBEH typically employs one of four transduction mechanisms:

piezoelectric, electrostatic, electromagnetic, or magnetostrictive [100]. A fifth mechanism known as triboelectricity is a more recent development, however, it still remains largely theoretical [101]. Note that the chosen transduction mechanism will vary depending on the requirements of the application at hand.

2.2.1.1 Piezoelectric Transducer

A piezoelectric transducer is a material that uses the piezoelectric effect to convert one type of energy into another. In the context of VBEHs, a piezoelectric transducer can be incorporated into the device structure, to allow the conversion of mechanical energy into electrical energy. The transducer works when a mechanical stress or strain is exerted upon it. The stress or strain causes the material to deform, which results in an imbalance in its charge [102]. The charge imbalance influences a voltage and furthermore an electric field.

2.2.1.2 Electrostatic Transducer

In vibration-based energy harvesting, a variable capacitor is used as an electrostatic transducer [103]. A variable capacitor is an energy storage device, that consists of two metallic plates with a dielectric material between them. The amount of energy that a capacitor is able to store is defined by the capacitance, C as follows:

$$C = \frac{A\epsilon_0\epsilon_r}{d} \quad 5$$

Where A is the area of the plates, ϵ_0 is the permittivity of free space, and ϵ_r is the permittivity of the relative medium between the plates (commonly air), and d is the distance between the two plates. In VBEH, the variable capacitor is subjected to mechanical vibrations, which causes the separation distance between the two plates to change.

If a voltage, V , is applied across the plates of the capacitor, then an electric field will be induced. The electric field will cause a positive charge to accumulate on one plate, and a negative charge to accumulate on the other [101]. This is known as the electrostatic effect. If the voltage source disconnects from the capacitor, then the charge, q , that is stored will remain, until discharged by some means. The relationship between charge, capacitance, and voltage is given by

$$q = CV \quad 6$$

For a capacitor to release the charge it must be connected to an external circuit. When a conductive path is established between the two plates, the stored charge begins to flow as an electric current.

2.2.1.3 Electromagnetic Transducer

An electromagnetic transducer, which contains a coil of wire and a magnet, utilizes Faraday's law of electromagnetic induction to generate electrical energy. When external vibrations are present upon the transducer, the wire and magnet move relative to one other, which causes a change in magnetic flux, in turn inducing a voltage between the two ends of the coil wire. The amount of voltage that can be produced depends on the number of loops in the coil and the rate of change of the magnetic flux. The principle is summarised by Faraday's law of electromagnetic induction [104]:

$$\varepsilon = -N \frac{\Delta\vartheta}{\Delta t} \quad 7$$

Where ε is the voltage produced, N is the number of loops of the coil, ϑ is the magnetic flux, and t is the time. Further analysis of equation (7) yields:

$$\varepsilon = \beta l v \quad 8$$

In equation (8), β represents magnetic field strength, l is the wire's length, and v is the relative velocity between the magnet and the wire. The equation shows that to boost voltage generation, increasing β , l or v is necessary [105].

2.2.1.4 Magnetostrictive Transducer

A magnetostrictive transducer is a ferromagnetic material coiled with wire that operates on Faraday's law of electromagnetic induction, employing either the joule effect or the Villari effect [106]. In the context of vibration-based energy harvesting (VBEH), the Villari effect is employed. The Villari effect converts mechanical energy into electrical energy when a vibration-induced stress or strain acts on an active magnetostrictive material. This stress or strain alters the magnetic flux density within the material, generating an alternating voltage across the surrounding coil wire. Note that the joule effect is the reversal of the Villari effect.

2.2.2 Applications for a VBEH

At present VBEHs only offer relatively low levels of power, within the range of mW to μ W [100], albeit this is sufficient to power small wireless autonomous devices like those in wearable electronics and wireless sensor networks [107]. Wearable electronics include both external devices such as wristwatches [108] and jewellery, and internal implantable devices like cardiac pacemakers [109] and neuro-prosthetics. Wireless sensor networks are made up of small sensor nodes that can collect, communicate, and compute data. The internet of things [110], industrial automation [111], and aircraft health monitoring [112] are some of the applications in which wireless sensor networks can be used. Batteries are the current dominant power source for this category of application; however, they present a number of problems.

Batteries are unsustainable due to their reliance on limited natural resources [113]. They also have a relatively low power density, limiting their power output per unit mass [114]. Batteries come with a finite lifespan, influenced by usage, application, type, and size, requiring periodic maintenance that can be costly and time-consuming [115]. Additionally, batteries contain hazardous chemicals that can harm both health and the environment if not disposed of properly [116]. In light of these limitations, VBEHs are recognized as a promising alternative technology.

2.2.3 Limitations of a VBEH

VBEHs face a significant challenge in generating substantial power output. Fundamentally VBEHs only operate in the vicinity of their resonance [117]. This means that there is a very limited bandwidth over which vibration-based mechanical energy can be harvested. Ambient vibrations are often constrained by this condition, as they are made up of random and broadband resonant frequencies which have low excitation levels [102].

To improve the performance of VBEHs, there are two general approaches that may be taken. The first approach is to amplify and tune any input vibration, to meet not only the resonant requirements of the harvester but also the harvesting demands of the transduction mechanism. The second approach is to widen the bandwidth of the harvester to accommodate a larger range of excitation frequencies. The most common device structure used for tuning, in both approaches, is an oscillating device that resonates at a characteristic frequency [56], [118].

Although both approaches are practicable, the underlying mechanism behind each approach raises a notable concern. The bandwidth of the resonant oscillator is narrow [56]. In principle,

the bandwidth of the oscillator can be broadened by changing either the effective mass, stiffness, or damping characteristics [119]. To alter such characteristics different techniques may be used, which can include controlling the geometrical properties of the device, using an oscillator of multiple degrees of freedom, electrical tuning, magnetic tuning, and the application of external forces. Furthermore, one could exploit the effects of nonlinearities to provide a broader resonant peak, this is a technique that has gained a lot of traction in recent years [56].

2.2.4 Tunable Mass Amplifier for a VBEH

In vibration based energy harvesting it is necessary to tune or extend the bandwidth of the harvester to improve performance capabilities, as mentioned in section 2.2.3. To achieve this, a tunable device, such as an oscillator, can be employed [118].

A lot of research has been conducted on oscillators that work to change either the effective stiffness [120], [121] or damping characteristics of a dynamic system [122], but in the context of vibration-based energy harvesting, oscillators that work on either of these accounts could potentially defeat the purpose of the application. To alter the effective stiffness characteristics of a VBEH, and in turn the frequency characteristics, an oscillator must exert and maintain a mechanical straining force on the harvester, this is likely to consume power, often generated by the harvester itself [119]. To change the effective damping properties of a VBEH, an oscillator is required to provide and sustain a damping force on the system. The damping force will expand the resonant region of the harvester, but it will also sacrifice the availability of power. Oscillators that use less power for frequency tuning are preferable, particularly in vibration-based energy harvesting applications, as the performance of the harvester is in some regards proportional to the generation of net power [123].

In literature, less emphasis has been placed on oscillators that work to adjust the effective mass characteristics of a dynamic system. Oscillators that work based on this principle are likely to consume less power during tuning, than oscillators that work to alter the effective stiffness or damping characteristics. This is because no mechanical straining force or damping force is to be applied and maintained. Instead, the oscillator must either redistribute the mass within its structure, change its boundary conditions, or change its effective dimensions [119]. By altering either of these properties, the effective mass moment of inertia will change, which in turn will alter the natural frequency of the dynamic system to which the oscillator is attached.

Energy is kept to a minimum in this technique, as the only effort required is to move the position or orientation of the oscillator.

This work presents six different oscillators, known as IAs. Each IA will be prototyped and passively attached to a cantilever beam. The IAs will work to alter the effective mass, and thus natural frequency characteristics of the beam. The effective mass will be altered first and foremost by controlling the effective dimensions of each oscillator; then additional tests will be conducted to redistribute a set of discrete masses placed upon each IA. Note that the dynamic response will vary amongst each mechanism, due to differences in design.

Through the fabrication and experimental analysis of these IAs, valuable insights will be gained into effective mass amplification, particularly through geometrical changes. This knowledge can subsequently guide the optimization of oscillators for integration into vibration energy harvesting systems. Furthermore, if successful, the IAs presented in this thesis hold the potential to enhance the power generation capabilities of VBEHs. They may be passively attached to a VBEH, providing a means to fine-tune the resonance for improved performance.

3. Equations of Motion for the proposed IA Mechanisms

In this thesis, six IAs are proposed. The IAs can be classified into two sets, the first set constitutes the single-stage, compound, and nested IAs, and the second set represents their corresponding truss-structured counterparts, single-stage truss, compound truss, and nested truss. In this Section, the first set of IAs will be presented. The systems will be considered, and their equations of motion will be determined. It is crucial to understand the equations of motion for each IA, not just to comprehend their behaviour, but also to predict their performance within a real-life application. Note that although there is a slight design variation between the two sets of IAs, detailed in Section 4, the configuration between corresponding mechanisms remains the same (e.g., single-stage and single-stage truss). For this reason, and due to the assumptions made during the analysis, the derived dynamic equations will be equivalent amongst corresponding IAs.

3.1 Single-Stage Inertial Amplifier

3.1.1 System Considered and Kinematic Relations

The single-stage IA is shown in Figure 4a). Four rigid arms are connected together by four pin joints to form the rhombus shape structure of the mechanism. The arms move freely around each joint, which are represented by black dots in Figure 4a) and Figure 4b). At the furthest left and furthest right joints of the structure, masses m are located. Note that for this analysis all the components which constitute the single-stage IA are assumed to have negligible mass, such as the rigid arms, bearings, pins, and brackets. The top and the bottom joints of the structure have a free and a fixed connection, respectively. The vertical line of symmetry of the mechanism, through the top and bottom joints, to the axis of the adjoining arms defines the amplifier angle of the system, ϕ , which is shown in Figure 4a) and Figure 4b). When a force is applied to the vertical plane of the system, the amplifier will move, and a change in ϕ will occur. The motion of the system is characterized by the vertical displacement z , which induces the motion of the two proof masses. The masses move vertically as $\frac{z}{2}$ and horizontally by x .

Due to the symmetric nature of the single-stage IA the mechanism can be divided vertically in half, which will allow for a more straightforward mathematical analysis of the system. Figure 4b) shows the reduced model of the single-stage IA. The structure has height, h_1 , width, w_1 , and each arm of the mechanism has length, l_1 . The model has three joints which are denoted by the letters a, b, and c, a is the free end of the structure, b is the joint where mass m_b is housed, and c is the fixed end of the system. Note that m_b in Figure 4b) is equivalent to m in Figure 4a). It should also be made clear that the reduced model in Figure 4b) will experience the same motion as the single-stage IA, and so the characterization will be alike.

For this analysis, the reduced model will be examined, and the derived equation of motion will be multiplied by a factor of two upon founding, this is to account for the full dynamics of the single-stage IA. Once the properties of the single-stage IA are established, the IA can be coupled to any dynamic system, such systems may include a mass-spring network or a general finite element structure, as displayed in Figure 4c) and Figure 4d), respectively. By passively attaching the IA to such a system its underlying characteristics can be altered.

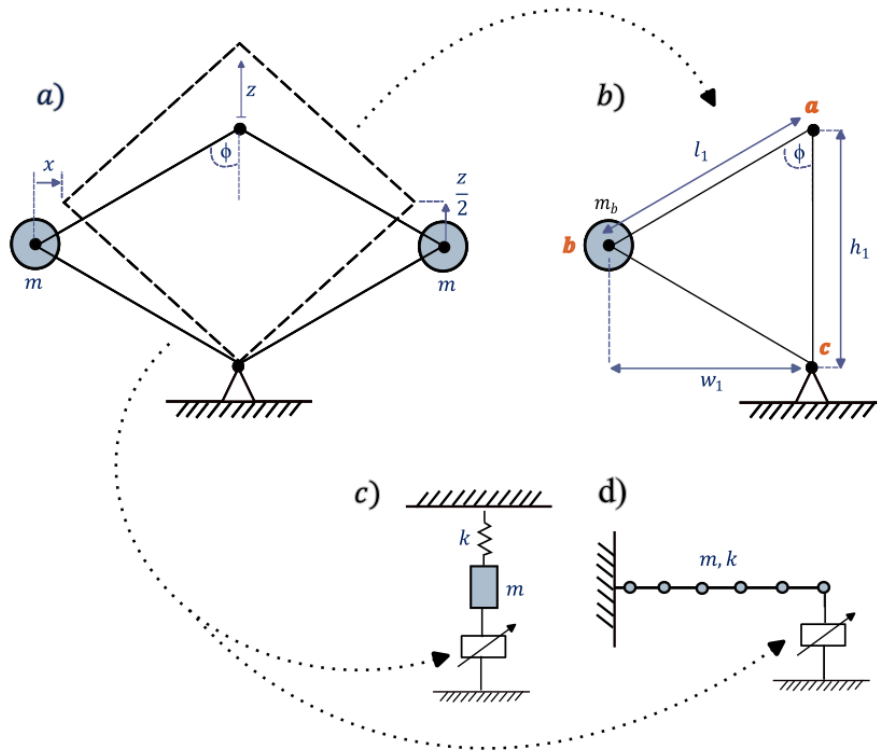


Figure 4: a) The single-stage inertial amplifier, showing relative displacements. b) One-half of the single-stage inertial amplifier. c) Coupling to a mass-spring system. d) Coupling to a general finite element structure.

The analysis proceeds as follows: firstly, the kinematics at each joint will be established. Once known, the kinematics are to be mapped in terms of the vertical displacement of the system, z , as required for the Lagrangian analysis in Subsection 3.1.2. To obtain the kinematics at each joint in terms of the motion z , a chain of functions will be formed. Therefore, joint a is written as it is foundational.

Joint a)

The vertical displacement of joint a) is given by

$$z_a = z \tag{9}$$

The horizontal displacement of joint a) is given by

$$x_a = 0 \tag{10}$$

Equation (9) written as a function of z is obtained as

$$z_a = z_a(z) \tag{11}$$

Joint b)

The vertical displacement of joint b) is given by

$$z_b = \frac{z_a}{2} = \frac{z}{2} \quad 12$$

To find the horizontal displacement x_b at joint b, Pythagorean theorem is applied to members a-b in Figure 4b).

$$l_1^2 = (w_1 - x_b)^2 + \left(\frac{h_1}{2} - z_b + z_a\right)^2 \quad 13$$

Which on substitution of equation (12) becomes

$$l_1^2 = (w_1 - x_b)^2 + \left(\frac{h_1}{2} + z_b\right)^2 \quad 14$$

Which rearranges to give

$$x_b = w_1 - \sqrt{l_1^2 - \left(\frac{h_1}{2} + z_b\right)^2} \quad 15$$

Equation (12) written as a function of z becomes

$$z_b = z_b(z) \quad 16$$

Equation (15) written as a function of z is

$$x_b = x_b(z_b(z)) \quad 17$$

Joint c)

Although there is no displacement at joint c) due to the fixed boundary condition, the kinematics are stated for completeness.

$$z_c = 0 \quad 18$$

3.1.2 Lagrangian Analysis of the Single-Stage Inertial Amplifier

In this Subsection, the equations of motion for the single-stage IA will be derived using the Lagrangian function. The Lagrangian function, characterizes the state of a dynamic system based on position coordinates and their time derivatives, and it is equivalent to the difference between the potential energy and the kinetic energy of a system. The kinematic relationships obtained in the previous Subsection (3.1.1.) will be used in the Lagrangian function.

The Lagrangian function is defined by

$$L = T - V \quad 20$$

Where T is the kinetic energy of the system and V is the potential energy of the system. The kinetic energy of the single-stage IA is expressed based on the assumption that the mass of the system (constituent components) is negligible, except for the mass at joint b), denoted by m_b .

$$T = \frac{1}{2} (m_b (\dot{x}_b^2 + \dot{z}_b^2)) \quad 21$$

Next, the Euler-Lagrange equation is defined, from which the equations of motion can be calculated.

$$\frac{d}{dt} \left(\frac{\partial L}{\partial \dot{z}} \right) - \frac{\partial L}{\partial z} = 0 \quad 22$$

Where $\frac{\partial L}{\partial z}$ is the negative derivative of the potential energy, and $\frac{d}{dt} \left(\frac{\partial L}{\partial \dot{z}} \right)$ is the time derivative of the generalized momentum of the system. For the single-stage IA the potential energy is assumed to be zero. This is because there are no spring elements contained within the mechanism. In addition, the device is intended for use in the horizontal plane, rather than the vertical plane, thus making the gravitational potential energy of the proof mass negligible. Note that the mechanism is orientated in vertical plane in Figure 4 for illustrative purposes, but it is experimentally analysed in the horizontal plane in Section 5.

$$\frac{\partial L}{\partial z} = \frac{\partial L}{\partial x_b} \frac{\partial x_b}{\partial z} + \frac{\partial L}{\partial z_b} \frac{\partial z_b}{\partial z} = 0 \quad 23$$

The generalized momentum of the system is expressed as

$$\frac{\partial L}{\partial \dot{z}} = \frac{\partial L}{\partial \dot{x}_b} \frac{\partial \dot{x}_b}{\partial \dot{z}} + \frac{\partial L}{\partial \dot{z}_b} \frac{\partial \dot{z}_b}{\partial \dot{z}} \quad 24$$

Which on substitution of the terms $\frac{\partial \dot{x}_b}{\partial \dot{z}} = \frac{\partial x_b}{\partial z}$ and $\frac{\partial \dot{z}_b}{\partial \dot{z}} = \frac{\partial z_b}{\partial z}$, and equation (14), together with expansion using the chain rule and product rule, the equation becomes

$$\frac{\partial L}{\partial \dot{z}} = m_b \left(\dot{x}_b \left(\frac{\partial x_b}{\partial z} \right) + \dot{z}_b \left(\frac{\partial z_b}{\partial z} \right) \right) \quad 25$$

By taking the time derivative of equation (25) the equation evolves to

$$\frac{d}{dt} \left(\frac{\partial L}{\partial \dot{z}} \right) = m_b \left(\ddot{x}_b \left(\frac{\partial x_b}{\partial z} \right) + \dot{x}_b \left(\frac{\partial^2 x_b}{\partial z^2} \dot{z} \right) + \ddot{z}_b \left(\frac{\partial z_b}{\partial z} \right) + \dot{z}_b \left(\frac{\partial^2 z_b}{\partial z^2} \dot{z} \right) \right) \quad 26$$

Which on substitution of the terms $\dot{x}_b = \frac{\partial x_b}{\partial z} \dot{z}$, $\ddot{x}_b = \frac{\partial x_b}{\partial z} \ddot{z} + \frac{\partial^2 x_b}{\partial z^2} \dot{z}^2$, $\dot{z}_b = \frac{\partial z_b}{\partial z} \dot{z}$ and $\ddot{z}_b = \frac{\partial z_b}{\partial z} \ddot{z} + \frac{\partial^2 z_b}{\partial z^2} \dot{z}^2$, and through simplification, the equation becomes

$$\frac{d}{dt} \left(\frac{\partial L}{\partial \dot{z}} \right) = m_b \left(\left(\frac{\partial x_b}{\partial z} \cdot \frac{\partial x_b}{\partial z} + \frac{\partial z_b}{\partial z} \cdot \frac{\partial z_b}{\partial z} \right) \ddot{z} + 2 \left(\frac{\partial x_b}{\partial z} \cdot \frac{\partial^2 x_b}{\partial z^2} + \frac{\partial z_b}{\partial z} \cdot \frac{\partial^2 z_b}{\partial z^2} \right) \dot{z}^2 \right) \quad 27$$

The derivatives required to satisfy equation (27) are given by equations (28-31)

$$\frac{\partial x_b}{\partial z} = \frac{\frac{h_1}{2} + \frac{z}{2}}{2\sqrt{l_1^2 - \left(\frac{h_1}{2} + \frac{z}{2}\right)^2}} \quad 28$$

$$\frac{\partial^2 x_b}{\partial z^2} = \frac{\left(\frac{h_1}{2} + \frac{z}{2}\right)^2}{4\left(l_1^2 - \left(\frac{h_1}{2} + \frac{z}{2}\right)^2\right)^{3/2}} + \frac{1}{4\sqrt{l_1^2 - \left(\frac{h_1}{2} + \frac{z}{2}\right)^2}} \quad 29$$

$$\frac{\partial z_b}{\partial z} = \frac{1}{2} \quad 30$$

$$\frac{\partial^2 z_b}{\partial z^2} = 0 \quad 31$$

It is also useful to have

$$\frac{\partial x_b}{\partial z} \cdot \frac{\partial x_b}{\partial z} = -\frac{\left(\frac{h_1}{2} + \frac{z}{2}\right)^2}{4\left(\left(\frac{h_1}{2} + \frac{z}{2}\right)^2 - l_1^2\right)} \quad 32$$

$$\frac{\partial x_b}{\partial z} \cdot \frac{\partial^2 x_b}{\partial z^2} = \frac{\left(\frac{h_1}{2} + \frac{z}{2}\right)}{8\left(l_1^2 - \left(\frac{h_1}{2} + \frac{z}{2}\right)^2\right)} - \frac{\left(\frac{h_1}{2} + \frac{z}{2}\right)^3}{8\left(l_1^2 - \left(\frac{h_1}{2} + \frac{z}{2}\right)^2\right)^2} \quad 33$$

$$\frac{\partial z_b}{\partial z} \cdot \frac{\partial z_b}{\partial z} = \frac{1}{4} \quad 34$$

$$\frac{\partial z_b}{\partial z} \cdot \frac{\partial^2 z_b}{\partial z^2} = 0 \quad 35$$

Now recall $m_b = m$. Upon substitution of m , and equations (32-35) into equation (27), the equation of motion for the reduced model, shown in Figure 4b), can be found. To find the equation of motion for the full single-stage IA, shown in Figure 4a), it is required that the equation of motion for the reduced model be multiplied by a factor of 2, to account for the symmetry amongst systems. By doing this, the equation of motion for the single-stage IA becomes

$$\frac{d}{dt} \left(\frac{\partial L}{\partial \dot{z}} \right) = m \left(\left(-\frac{\left(\frac{h_1}{2} + \frac{z}{2} \right)^2}{2 \left(\left(\frac{h_1}{2} + \frac{z}{2} \right)^2 - l_1^2 \right)} + \frac{1}{2} \right) \dot{z} \right. \\ \left. + \left(\frac{\left(\frac{h_1}{2} + \frac{z}{2} \right)}{2 \left(l_1^2 - \left(\frac{h_1}{2} + \frac{z}{2} \right)^2 \right)} - \frac{\left(\frac{h_1}{2} + \frac{z}{2} \right)^3}{2 \left(l_1^2 - \left(\frac{h_1}{2} + \frac{z}{2} \right)^2 \right)^2} \right) \dot{z}^2 \right) = 0 \quad 36$$

Equation (36) shows the equation of motion for the single-stage IA. The equation of motion represents the dynamic behaviour of the system. All terms in the equation are non-linear, with the exception of one linear term, $\frac{m}{2}\dot{z}$. This linear term reflects a proportional relationship between the acceleration, \dot{z} , of the discrete mass, m , and its displacement, $\frac{z}{2}$. The remaining terms are non-linear due to the presence of multiple degrees and complex functions of the displacement of the system, z .

It is challenging to predict the exact behaviour of the single-stage IA from the equation of motion, however, a prognosis about the behaviour can be made based on the parameters in the equation. Notably the discrete mass, the displacement, the length of the arms, l_1 , and the height, h_1 , of the mechanism. These parameters are key variables which will influence the natural frequencies and the amplitudes of motion of the single-stage IA. To better understand the effects of these parameters, the equation of motion can be split into two distinct components, which can then be graphically represented.

$$\overline{Y}_m(z)\dot{z} + \beta(z)\dot{z}^2 = 0 \quad 37$$

These components are namely the effective mass term, \overline{Y}_m , and the velocity squared coefficient, β . By separately analyzing each component, a deeper understanding of the full behaviour of the single-stage IA can be achieved.

The effective mass term of the single-stage IA is given by

$$\bar{Y}_m = m \left(-\frac{\left(\frac{h_1}{2} + \frac{z}{2}\right)^2}{2\left(\left(\frac{h_1}{2} + \frac{z}{2}\right)^2 - l_1^2\right)} + \frac{1}{2} \right) \quad 38$$

The velocity squared coefficient of the single-stage IA is given by

$$\beta = m \left(\frac{\left(\frac{h_1}{2} + \frac{z}{2}\right)}{2\left(l_1^2 - \left(\frac{h_1}{2} + \frac{z}{2}\right)^2\right)} - \frac{\left(\frac{h_1}{2} + \frac{z}{2}\right)^3}{2\left(l_1^2 - \left(\frac{h_1}{2} + \frac{z}{2}\right)^2\right)^2} \right) \quad 39$$

In order to show the behaviour of \bar{Y}_m and β , the parameter values l_1 , h_1 , m , and z need to be specified. The parameter l_1 is a fixed physical dimension, and in this work, it is assigned a value of 100mm. To determine the value of the parameter h_1 , trigonometric relations are utilized with reference to Figure 4b). Table 1 presents the calculated values for h_1 , corresponding to different initial amplifier angles \emptyset . The initial amplifier angle is the angle measured between the vertical line of symmetry of the mechanism and the axis of the arm connecting to the line of symmetry, when the mechanism is stationary. Note that different initial amplifier angles are presented, as literature states that effective mass amplification results from the geometrical amplification of the IA [47], [48], i.e. changes to the amplifier angle. The parameter m is chosen as 1g, while the value of z is chosen to range between -10 and 30mm. For the given dimensions of the mechanism, this range of displacement values seems realistic. Figure 5 illustrates the behaviour of \bar{Y}_m and β for the specified values of l_1 , h_1 , m and z .

Table 1: A table to show the values for the parameters l_1 and h_1 , for different initial amplifier angles. Six cases are shown.

Amplifier Angle \emptyset (degrees)	l_1 (mm)	h_1 (mm)
5	100.00	199.24
10	100.00	196.96
15	100.00	193.19
20	100.00	187.94
25	100.00	181.26
30	100.00	173.21

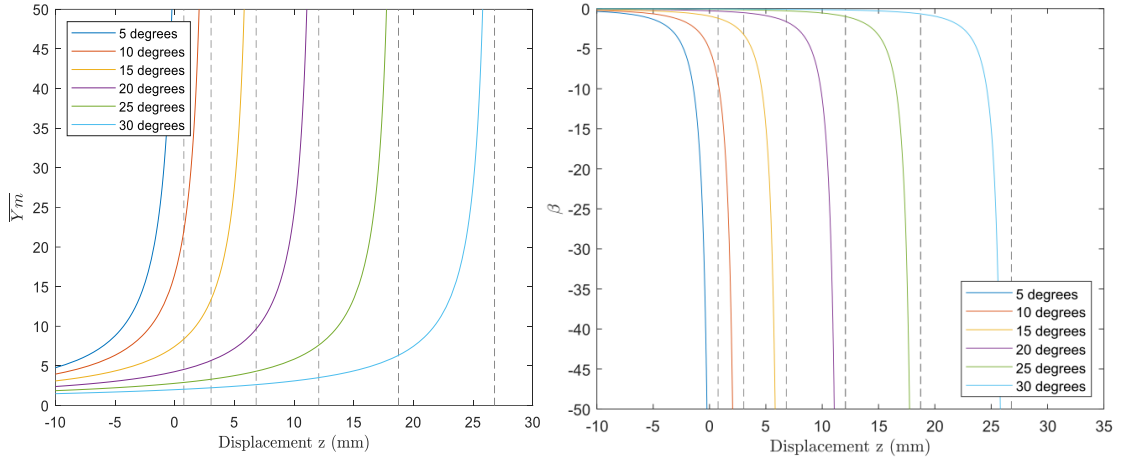


Figure 5: a) Effective mass as a function of the displacement z for the single-stage IA. b) Non-linear velocity coefficient as a function of the displacement z for the single-stage IA. Six different values for the initial amplifier angle Φ are shown in each plot.

The curves depicted in Figure 5a) illustrate the exponential relationship between the single-stage IAs effective mass and displacement for varying initial amplifier angles. The general trend shows that as the displacement of the mechanism increases (indicated by negative displacement values) the effective mass of the system decreases. When the arms of the mechanism meet, the displacement stops, and the curves tend towards infinity. For smaller initial amplifier angles there is a faster rate of change of effective mass with displacement, than for larger initial amplifier angles.

Figure 5b) illustrates an exponential relationship between the velocity squared coefficient and the displacement of the single-stage IA for different initial amplifier angles. The general trend shows that as the displacement of the mechanism increases the velocity squared coefficient rapidly decreases. Note that the velocity squared coefficient is negative. When the arms of the mechanism meet, the displacement stops, and the curves tend towards infinity. For smaller initial amplifier angles there is a faster rate of change of the velocity squared coefficient with displacement, than for larger initial amplifier angles. The exponential rate of change signifies that the behaviour of the single-stage IA is non-linear. The trend may be caused by a restoring force acting on the system which is not directly proportional to the displacement of the system. Understanding this relationship is crucial if the performance of the single-stage IA is to be optimized.

3.1.3 Linearised Equation of Motion for the Single-Stage Inertial Amplifier

As most non-linear dynamic systems exhibit linear behaviours over a small range of motion, or in the vicinity of a particular operating point, it is possible to approximate their behaviours as linear. In this Subsection, the non-linear equation of motion for the single-stage IA (equation (36)) will be transformed into a linear approximation. To linearise the equation of motion, the vertical displacement of the system, z , and the velocity of the system, \dot{z} , will tend to zero.

As z and \dot{z} tend to 0, equation (36) becomes

$$\frac{d}{dt} \left(\frac{\partial L}{\partial \dot{z}} \right) = m \left(-\frac{\left(\frac{h_1}{2}\right)^2}{2 \left(\left(\frac{h_1}{2}\right)^2 - l_1^2 \right)} + \frac{1}{2} \right) \ddot{z} \quad 40$$

Using trigonometry, with reference to Figure 4b) the equation simplifies to

$$\frac{d}{dt} \left(\frac{\partial L}{\partial \dot{z}} \right) = \frac{m}{2} (\cot^2 \phi + 1) \ddot{z} = 0 \quad 41$$

The linearised equation of motion for the single-stage IA, equation (41), is extremely useful because it provides a more straightforward and manageable description of the behaviour of the system, when compared to the non-linear equation of motion. The equation shows that the constant of proportionality is determined by the overall discrete mass, m , and amplifier angle, ϕ , of the system. The constant of proportionality represents the relationship between the rate of change of the state variables, displacement and velocity (z and \dot{z}), and the acceleration of the system (\ddot{z}).

Given the significant influence of the discrete mass and amplifier angle on the dynamic behaviour of the system, these parameters will be carefully adjusted during experimental testing. In Table 1 of Subsection 3.1.2, it is demonstrated that the amplifier angle can be easily modified by adjusting the height of the mechanism. Therefore, effective geometric modifications will be employed to fine-tune the amplifier angle. Conversely, the discrete mass will be tuned by incorporating varying quantities of proof mass into the system. This approach allows for precise control over the discrete mass and facilitates the adjustment of the system's overall behaviour.

3.2 Compound Inertial Amplifier

3.2.1 System Considered and Kinematic Relations

The next mechanism to be considered is the compound IA, which is shown in Figure 6. The compound IA extends the design of the single-stage IA, which is outlined in Section 3.1, and it has been developed to further enhance tuning capabilities. A primary and a secondary mechanism, which respectively are illustrated by the black and purple lines in Figure 6, are linked together to form the structure of the compound IA; the secondary mechanism is housed within the framework of the primary mechanism.

The primary mechanism is largely the same as the single-stage IA discussed in Section 3.1.1, with the only difference being that the masses m have been eliminated from the furthest left and furthest right joints of the structure. Despite this change, the details provided in Section 3.1.1 are still applicable to the primary mechanism. The secondary mechanism is a pantograph linkage of two rhombus shaped IAs, formed by six rigid arms which are connected together by pin joints. The arms move freely around each joint, which are represented by black dots in Figure 6. At the two top and two bottom joints of the secondary mechanism, masses $\frac{m}{2}$ are positioned. Note that for this analysis all the components which constitute the compound IA are assumed to have negligible mass, such as the rigid arms, bearings, pins, and brackets. The mass within each small internal IA is equivalent to m , so that the mass contained within the whole system is equivalent to the mass contained within the single-stage IA. This is necessary to provide a fair comparison between the properties of the different IAs.

The amplifier angle for the primary and secondary mechanisms are given by ϕ_1 and ϕ_2 , respectively. When a force is applied to the vertical plane of the system, the amplifier moves, causing a change to both ϕ_1 and ϕ_2 . Note the primary and secondary mechanisms are arranged in offset vertical planes so that their movements do not intersect. The motion of the compound IA is characterized by displacement z , which induces a horizontal displacement x , to the system.

The compound IA is symmetric amongst its vertical plane, through the fixed end, the linkage of the two internal IAs, and the free end of the system. For this reason, the system can be reduced, as shown in Figure 6. The reduced model will be used in this analysis, to ease complexity. In finding the kinematics at joints a, b, c, d, e, and f, the equations of motion for the reduced system can be found. Duplicating the equations of motion, will fulfil the dynamic

motion of the whole system. Note that in the previous Section the kinematics for the single-stage IA were found at joints a, b, and c, which are directly applicable to joints a, b, and c for the compound IA.

The parameters height, width, and length, denoted by h , w , and l , respectively, characterize the geometry of the reduced system. These parameters are followed by either a subscript number 1 or 2. Subscript 1 indicates that the parameter belongs to the primary mechanism, and subscript 2 indicates that the parameter defines the secondary mechanism. Note that the width of the primary and secondary mechanisms is the same, so both systems use the same notation, w_1 . The masses in the reduced model are located at joints e and f, thus the following notation is used for analysis: $m_e = m_f = \frac{m}{2}$.

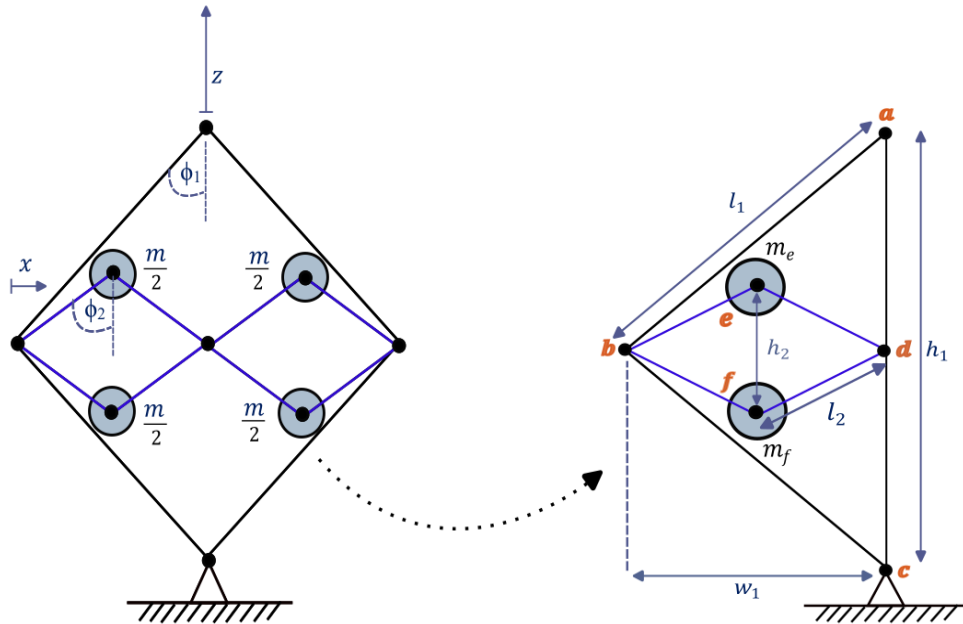


Figure 6: Conversion of the compound inertial amplifier into one-half system.

The analysis proceeds as follows: firstly, the kinematics at joints d, e, and f will be derived. The kinematics at each joint are required for the Lagrangian analysis in Subsection 3.2.2, to determine the equations of motion for the system. The Lagrangian function requires the kinematics at each joint to be expressed in terms of the same common variable. Therefore, a chain of functions will be established for each joint, to map the kinematics in terms of vertical displacement of the system, z . By relating the geometry of the mechanism to the motion of the system, the kinematic relations at joints a, b, c, d, e, and f are as follows:

Joints a), b) and c)

The kinematics at joints a, b and c, are stated in Subsection 3.1.1; refer to equations (9-19).

Joint d)

The vertical displacement of joint d) is given by

$$z_d = \frac{z_a}{2} = \frac{z}{2} \quad 42$$

The horizontal displacement of joint d) is given by

$$x_d = 0 \quad 43$$

Equation (42) written as a function of z becomes

$$z_d = z_d(z) \quad 44$$

Joint e)

The vertical displacement of the mass at joint e) is given by

$$z_e = \sqrt{l_2^2 - \left(\frac{w_1}{2} - x_b\right)^2} - \frac{h_2}{2} + z_b \quad 45$$

The derivation to obtain the vertical displacement of joint e is shown by equations (121-123), which can be found in the appendix, section 8 sub-section 8.1.

The horizontal movement of the mass at joint e) is

$$x_e = \frac{x_b}{2} \quad 46$$

Equations (45 and 46) written as a function of z are of the form

$$z_e = z_e(x_b, z_b) = z_e(x_b(z_b(z)), z_b(z)) \quad 47$$

$$x_e = x_e(x_b(z_b(z))) \quad 48$$

Joint f)

The vertical displacement of joint f is given by

$$z_f = z_b + \frac{h_2}{2} - \sqrt{l_2^2 - \left(\frac{w_1}{2} - x_b\right)^2} \quad 49$$

The derivation to obtain the vertical displacement of joint f is shown by equations (124-126), which can be found in the appendix, section 8 sub-section 8.1.

The horizontal displacement of the mass at joint f) is given by

$$x_f = \frac{x_b}{2} \quad 50$$

Equations (49 and 50) written as a function of z are of the form

$$z_f = z_f(x_b, z_b) = z_f(x_b(z_b(z)), z_b(z)) \quad 51$$

$$x_f = x_f(x_b(z_b(z))) \quad 52$$

3.2.2 Lagrangian Analysis of the Compound Inertial Amplifier

In this Subsection the equations of motion for the compound IA will be derived using the Lagrangian function. The Lagrangian function requires the kinematic relationship at each joint. Thus, the work conducted in Subsection 3.2.1, will be utilized and continued here. The Lagrangian function is defined by equation (20) in Subsection 3.1.2, and it expresses the kinetic energy, T, minus the potential energy, V, of a system. The kinetic energy of the compound IA is stated below by equation (53), based on the assumption that the mass of the system (constituent components) is negligible, except for the mass at joints e) and f), denoted by m_e and m_f , respectively.

$$T = \frac{1}{2} \left(m_e (\dot{x}_e^2 + \dot{z}_e^2) + m_f (\dot{x}_f^2 + \dot{z}_f^2) \right) \quad 53$$

In Section 3.1.2, the Euler-Lagrange equation is defined by equation (22). The Euler-Lagrange equation will be used to calculate the equations of motion for the compound IA. The equation is the time derivative of the generalized momentum of the system, minus, the derivative of the potential energy of the system. For the compound IA the potential energy of the system is considered zero, due to the fact that there are no spring elements contained within the mechanism, and because the device is intended for use in the horizontal plane.

$$\frac{\partial L}{\partial z} = \frac{\partial L}{\partial x_e} \frac{\partial x_e}{\partial z} + \frac{\partial L}{\partial z_e} \frac{\partial z_e}{\partial z} + \frac{\partial L}{\partial x_f} \frac{\partial x_f}{\partial z} + \frac{\partial L}{\partial z_f} \frac{\partial z_f}{\partial z} = 0 \quad 54$$

The generalized momentum of the system is expressed as

$$\frac{\partial L}{\partial \dot{z}} = \frac{\partial L}{\partial \dot{x}_e} \frac{\partial \dot{x}_e}{\partial \dot{z}} + \frac{\partial L}{\partial \dot{z}_e} \frac{\partial \dot{z}_e}{\partial \dot{z}} + \frac{\partial L}{\partial \dot{x}_f} \frac{\partial \dot{x}_f}{\partial \dot{z}} + \frac{\partial L}{\partial \dot{z}_f} \frac{\partial \dot{z}_f}{\partial \dot{z}} \quad 55$$

Which on substitution of terms $\frac{\partial \dot{x}_e}{\partial \dot{z}} = \frac{\partial x_e}{\partial z}$, $\frac{\partial \dot{z}_e}{\partial \dot{z}} = \frac{\partial z_e}{\partial z}$, $\frac{\partial \dot{x}_f}{\partial \dot{z}} = \frac{\partial x_f}{\partial z}$ and $\frac{\partial \dot{z}_f}{\partial \dot{z}} = \frac{\partial z_f}{\partial z}$, and equation (53), together with the use of the chain and product rule, the equation becomes

$$\frac{\partial L}{\partial \dot{z}} = (m_e \dot{x}_e) \left(\frac{\partial x_e}{\partial z} \right) + (m_e \dot{z}_e) \left(\frac{\partial z_e}{\partial z} \right) + (m_f \dot{x}_f) \left(\frac{\partial x_f}{\partial z} \right) + (m_f \dot{z}_f) \left(\frac{\partial z_f}{\partial z} \right) \quad 56$$

Taking the time derivative of equation (56) the resulting equation can be obtained as

$$\begin{aligned} \frac{d}{dt} \left(\frac{\partial L}{\partial \dot{z}} \right) &= (m_e \ddot{x}_e) \left(\frac{\partial x_e}{\partial z} \right) + (m_e \dot{x}_e) \left(\frac{\partial^2 x_e}{\partial z^2} \dot{z} \right) + (m_e \ddot{z}_e) \left(\frac{\partial z_e}{\partial z} \right) + \\ &(m_e \dot{z}_e) \left(\frac{\partial^2 z_e}{\partial z^2} \dot{z} \right) + (m_f \ddot{x}_f) \left(\frac{\partial x_f}{\partial z} \right) + (m_f \dot{x}_f) \left(\frac{\partial^2 x_f}{\partial z^2} \dot{z} \right) + (m_f \ddot{z}_f) \left(\frac{\partial z_f}{\partial z} \right) + \\ &(m_f \dot{z}_f) \left(\frac{\partial^2 z_f}{\partial z^2} \dot{z} \right) \end{aligned} \quad 57$$

Which on substitution of the terms $\dot{x}_e = \frac{\partial x_e}{\partial z} \dot{z}$, $\ddot{x}_e = \frac{\partial x_e}{\partial z} \ddot{z} + \frac{\partial^2 x_e}{\partial z^2} \dot{z}^2$, $\dot{x}_f = \frac{\partial x_f}{\partial z} \dot{z}$, $\ddot{x}_f = \frac{\partial x_f}{\partial z} \ddot{z} + \frac{\partial^2 x_f}{\partial z^2} \dot{z}^2$, $\dot{z}_e = \frac{\partial z_e}{\partial z} \dot{z}$, $\ddot{z}_e = \frac{\partial z_e}{\partial z} \ddot{z} + \frac{\partial^2 z_e}{\partial z^2} \dot{z}^2$, $\dot{z}_f = \frac{\partial z_f}{\partial z} \dot{z}$ and $\ddot{z}_f = \frac{\partial z_f}{\partial z} \ddot{z} + \frac{\partial^2 z_f}{\partial z^2} \dot{z}^2$, and through simplification, equation (57) becomes

$$\begin{aligned} \frac{d}{dt} \left(\frac{\partial L}{\partial \dot{z}} \right) &= m_e \left(\left(\frac{\partial x_e}{\partial z} \cdot \frac{\partial x_e}{\partial z} + \frac{\partial z_e}{\partial z} \cdot \frac{\partial z_e}{\partial z} \right) \ddot{z} + 2 \left(\frac{\partial x_e}{\partial z} \cdot \frac{\partial^2 x_e}{\partial z^2} + \frac{\partial z_e}{\partial z} \cdot \frac{\partial^2 z_e}{\partial z^2} \right) \dot{z}^2 \right) \\ &+ m_f \left(\left(\frac{\partial x_f}{\partial z} \cdot \frac{\partial x_f}{\partial z} + \frac{\partial z_f}{\partial z} \cdot \frac{\partial z_f}{\partial z} \right) \ddot{z} \right. \\ &\left. + 2 \left(\frac{\partial x_f}{\partial z} \cdot \frac{\partial^2 x_f}{\partial z^2} + \frac{\partial z_f}{\partial z} \cdot \frac{\partial^2 z_f}{\partial z^2} \right) \dot{z}^2 \right) \end{aligned} \quad 58$$

The derivatives required to satisfy equation (58) are given by equations (127 -138), which can be found in the appendix, section 8 sub-section 8.1.

Now recall $m_e = m_f = \frac{m}{2}$. Upon substitution of $\frac{m}{2}$, and equations (133-138) into equation (58), the equation of motion for the reduced model, shown in Figure 6, can be found. To find the equation of motion for the full compound IA, it is required that the equation of motion for the reduced model be multiplied by a factor of 2, to account for the symmetry amongst systems. As a result of doing this, the equation of motion for the compound IA becomes

$$\begin{aligned}
\frac{d}{dt} \left(\frac{\partial L}{\partial \dot{z}} \right) = m & \left(\left(-\frac{\left(\frac{h_1+z}{2}\right)^2}{16\left(\left(\frac{h_1+z}{2}\right)^2 - l_1^2\right)} + \left(\frac{\left(\sqrt{l_1^2 - \left(\frac{h_1+z}{2}\right)^2} - \frac{w_1}{2}\right)\left(\frac{h_1+z}{2}\right)}{2\sqrt{l_2^2 - \left(\sqrt{l_1^2 - \left(\frac{h_1+z}{2}\right)^2} - \frac{w_1}{2}\right)^2} \sqrt{l_1^2 - \left(\frac{h_1+z}{2}\right)^2}} + \right. \right. \\
& \left. \left. \frac{1}{2} \right) \right) \ddot{z} + \left(\frac{\left(\frac{h_1+z}{2}\right)^3}{16\left(\left(\frac{h_1+z}{2}\right)^2 - l_1^2\right)^2} - \frac{\frac{h_1+z}{2}}{16\left(\left(\frac{h_1+z}{2}\right)^2 - l_1^2\right)} + \right. \\
& \left. \left(\frac{\left(\sqrt{l_1^2 - \left(\frac{h_1+z}{2}\right)^2} - \frac{w_1}{2}\right)\left(\frac{h_1+z}{2}\right)}{\sqrt{l_2^2 - \left(\sqrt{l_1^2 - \left(\frac{h_1+z}{2}\right)^2} - \frac{w_1}{2}\right)^2} \sqrt{l_1^2 - \left(\frac{h_1+z}{2}\right)^2}} + 1 \right) \right). \\
& \left(\frac{\sqrt{l_1^2 - \left(\frac{h_1+z}{2}\right)^2} - \frac{w_1}{2}}{2\sqrt{l_2^2 - \left(\sqrt{l_1^2 - \left(\frac{h_1+z}{2}\right)^2} - \frac{w_1}{2}\right)^2} \sqrt{l_1^2 - \left(\frac{h_1+z}{2}\right)^2}} + \frac{\left(\sqrt{l_1^2 - \left(\frac{h_1+z}{2}\right)^2} - \frac{w_1}{2}\right)\left(\frac{h_1+z}{2}\right)^2}{2\sqrt{l_2^2 - \left(\sqrt{l_1^2 - \left(\frac{h_1+z}{2}\right)^2} - \frac{w_1}{2}\right)^2} \left(l_1^2 - \left(\frac{h_1+z}{2}\right)^2\right)^{3/2}} - \right. \\
& \left. \frac{\left(\frac{h_1+z}{2}\right)^2}{2\sqrt{l_2^2 - \left(\sqrt{l_1^2 - \left(\frac{h_1+z}{2}\right)^2} - \frac{w_1}{2}\right)^2} \left(l_1^2 - \left(\frac{h_1+z}{2}\right)^2\right)} \right) \dot{z}^2 + m \left(\left(-\frac{\left(\frac{h_1+z}{2}\right)^2}{16\left(\left(\frac{h_1+z}{2}\right)^2 - l_1^2\right)} + \right. \right. \\
& \left. \left(\frac{\left(\frac{w_1}{2} - \sqrt{l_1^2 - \left(\frac{h_1+z}{2}\right)^2}\right)\left(\frac{h_1+z}{2}\right)}{2\sqrt{l_2^2 - \left(\frac{w_1}{2} - \sqrt{l_1^2 - \left(\frac{h_1+z}{2}\right)^2}\right)^2} \sqrt{l_1^2 - \left(\frac{h_1+z}{2}\right)^2}} + \frac{1}{2} \right) \right) \ddot{z} + \left(\frac{\left(\frac{h_1+z}{2}\right)^3}{16\left(\left(\frac{h_1+z}{2}\right)^2 - l_1^2\right)^2} - \right.
\end{aligned}$$

59

$$\begin{aligned}
& \frac{\frac{h_1+z}{2}}{16\left(\left(\frac{h_1+z}{2}\right)^2 - l_1^2\right)} + \left(\frac{\left(\frac{w_1}{2} - \sqrt{l_1^2 - \left(\frac{h_1+z}{2}\right)^2}\right)\left(\frac{h_1+z}{2}\right)}{\sqrt{l_2^2 - \left(\frac{w_1}{2} - \sqrt{l_1^2 - \left(\frac{h_1+z}{2}\right)^2}\right)^2} \sqrt{l_1^2 - \left(\frac{h_1+z}{2}\right)^2}} + 1 \right) \cdot \\
& \left(\frac{\left(\frac{h_1+z}{2}\right)^2}{2\sqrt{l_2^2 - \left(\sqrt{l_1^2 - \left(\frac{h_1+z}{2}\right)^2} - \frac{w_1}{2}\right)^2} \left(l_1^2 - \left(\frac{h_1+z}{2}\right)^2\right)} + \frac{\left(\sqrt{l_1^2 - \left(\frac{h_1+z}{2}\right)^2} - \frac{w_1}{2}\right)^2 \left(\frac{h_1+z}{2}\right)^2}{2\left(l_2^2 - \left(\sqrt{l_1^2 - \left(\frac{h_1+z}{2}\right)^2} - \frac{w_1}{2}\right)^2\right)^{3/2} \left(l_1^2 - \left(\frac{h_1+z}{2}\right)^2\right)} - \right. \\
& \frac{\sqrt{l_1^2 - \left(\frac{h_1+z}{2}\right)^2} - \frac{w_1}{2}}{2\sqrt{l_2^2 - \left(\sqrt{l_1^2 - \left(\frac{h_1+z}{2}\right)^2} - \frac{w_1}{2}\right)^2} \sqrt{l_1^2 - \left(\frac{h_1+z}{2}\right)^2}} - \\
& \left. \frac{\left(\sqrt{l_1^2 - \left(\frac{h_1+z}{2}\right)^2} - \frac{w_1}{2}\right)\left(\frac{h_1+z}{2}\right)^2}{2\sqrt{l_2^2 - \left(\sqrt{l_1^2 - \left(\frac{h_1+z}{2}\right)^2} - \frac{w_1}{2}\right)^2} \left(l_1^2 - \left(\frac{h_1+z}{2}\right)^2\right)^{3/2}} \right) \dot{z}^2
\end{aligned}$$

The equation of motion, presented in equation (59), represents the dynamic behaviour of the compound IA. The equation is inherently non-linear due to the fact it contains several complex functions of the displacement of the system, z , and has 2 or more degrees. A non-linear equation of motion, especially one of a very complex nature like equation (53), can be difficult to interpret. However, by analysing the parameters in the equation some insights can be gained about the behaviour of the system. Notably, the discrete mass of the mechanism, m , the vertical displacement of the system, the length of the arms of the primary mechanism, l_1 , the length of the arms of the secondary mechanism, l_2 , the height of the mechanism, h_1 , and the width of half of the compound IA, w_1 . These parameters are key variables which will influence the natural frequencies, and the amplitudes of motion of the compound IA. To comprehend the influence of these parameters on the mechanism, the equation of motion can be separated into two distinct components: the effective mass term, \overline{Y}_m , and the velocity squared coefficient, β , as shown by equation (37) in Section 3.1.2. Through individual analysis of these two components, a deeper understanding of the behaviour of the compound IA can be obtained.

The effective mass term of the compound IA is given by

$$\bar{Y}_m = m \left(\left(-\frac{2\left(\frac{h_1+z}{2}\right)^2}{16\left(\left(\frac{h_1+z}{2}\right)^2 - l_1^2\right)} \right) + \left(\frac{\left(\sqrt{l_1^2 - \left(\frac{h_1+z}{2}\right)^2} - \frac{w_1}{2}\right)\left(\frac{h_1+z}{2}\right)}{2\sqrt{l_2^2 - \left(\sqrt{l_1^2 - \left(\frac{h_1+z}{2}\right)^2} - \frac{w_1}{2}\right)^2}\sqrt{l_1^2 - \left(\frac{h_1+z}{2}\right)^2}} + \frac{1}{2} \right)^2 \right. \\ \left. + \left(\frac{\left(\frac{w_1}{2} - \sqrt{l_1^2 - \left(\frac{h_1+z}{2}\right)^2}\right)\left(\frac{h_1+z}{2}\right)}{2\sqrt{l_2^2 - \left(\frac{w_1}{2} - \sqrt{l_1^2 - \left(\frac{h_1+z}{2}\right)^2}\right)^2}\sqrt{l_1^2 - \left(\frac{h_1+z}{2}\right)^2}} + \frac{1}{2} \right)^2 \right) \quad 60$$

The velocity squared coefficient of the compound IA is given by

$$\beta = m \left(\left(\frac{\left(\frac{h_1+z}{2}\right)^3}{16\left(\left(\frac{h_1+z}{2}\right)^2 - l_1^2\right)^2} - \frac{\frac{h_1+z}{2}}{16\left(\left(\frac{h_1+z}{2}\right)^2 - l_1^2\right)} + \left(\frac{\left(\sqrt{l_1^2 - \left(\frac{h_1+z}{2}\right)^2} - \frac{w_1}{2}\right)\left(\frac{h_1+z}{2}\right)}{\sqrt{l_2^2 - \left(\sqrt{l_1^2 - \left(\frac{h_1+z}{2}\right)^2} - \frac{w_1}{2}\right)^2}\sqrt{l_1^2 - \left(\frac{h_1+z}{2}\right)^2}} + 1 \right) \cdot \left(\frac{\sqrt{l_1^2 - \left(\frac{h_1+z}{2}\right)^2} - \frac{w_1}{2}}{2\sqrt{l_2^2 - \left(\sqrt{l_1^2 - \left(\frac{h_1+z}{2}\right)^2} - \frac{w_1}{2}\right)^2}\sqrt{l_1^2 - \left(\frac{h_1+z}{2}\right)^2}} + \frac{\left(\sqrt{l_1^2 - \left(\frac{h_1+z}{2}\right)^2} - \frac{w_1}{2}\right)\left(\frac{h_1+z}{2}\right)^2}{2\sqrt{l_2^2 - \left(\sqrt{l_1^2 - \left(\frac{h_1+z}{2}\right)^2} - \frac{w_1}{2}\right)^2}\left(l_1^2 - \left(\frac{h_1+z}{2}\right)^2\right)^{\frac{3}{2}}} - \frac{\left(\frac{h_1+z}{2}\right)^2}{2\sqrt{l_2^2 - \left(\sqrt{l_1^2 - \left(\frac{h_1+z}{2}\right)^2} - \frac{w_1}{2}\right)^2}\left(l_1^2 - \left(\frac{h_1+z}{2}\right)^2\right)} \right) \right) \right) + m \left(\left(\frac{\left(\frac{h_1+z}{2}\right)^3}{16\left(\left(\frac{h_1+z}{2}\right)^2 - l_1^2\right)^2} - \frac{\frac{h_1+z}{2}}{16\left(\left(\frac{h_1+z}{2}\right)^2 - l_1^2\right)} + \left(\frac{\left(\frac{w_1}{2} - \sqrt{l_1^2 - \left(\frac{h_1+z}{2}\right)^2}\right)\left(\frac{h_1+z}{2}\right)}{\sqrt{l_2^2 - \left(\frac{w_1}{2} - \sqrt{l_1^2 - \left(\frac{h_1+z}{2}\right)^2}\right)^2}\sqrt{l_1^2 - \left(\frac{h_1+z}{2}\right)^2}} + 1 \right) \cdot \right) \right) \quad 61$$

$$\left(\frac{\left(\frac{h_1+z}{2}\right)^2}{2\sqrt{l_2^2-\left(\sqrt{l_1^2-\left(\frac{h_1+z}{2}\right)^2}-\frac{w_1}{2}\right)^2}\left(l_1^2-\left(\frac{h_1+z}{2}\right)^2\right)} + \frac{\left(\sqrt{l_1^2-\left(\frac{h_1+z}{2}\right)^2}-\frac{w_1}{2}\right)^2\left(\frac{h_1+z}{2}\right)^2}{2\left(l_2^2-\left(\sqrt{l_1^2-\left(\frac{h_1+z}{2}\right)^2}-\frac{w_1}{2}\right)^2\right)^{3/2}\left(l_1^2-\left(\frac{h_1+z}{2}\right)^2\right)} - \frac{\sqrt{l_1^2-\left(\frac{h_1+z}{2}\right)^2}-\frac{w_1}{2}}{2\sqrt{l_2^2-\left(\sqrt{l_1^2-\left(\frac{h_1+z}{2}\right)^2}-\frac{w_1}{2}\right)^2}\sqrt{l_1^2-\left(\frac{h_1+z}{2}\right)^2}} - \frac{\left(\sqrt{l_1^2-\left(\frac{h_1+z}{2}\right)^2}-\frac{w_1}{2}\right)\left(\frac{h_1+z}{2}\right)^2}{2\sqrt{l_2^2-\left(\sqrt{l_1^2-\left(\frac{h_1+z}{2}\right)^2}-\frac{w_1}{2}\right)^2}\left(l_1^2-\left(\frac{h_1+z}{2}\right)^2\right)^{3/2}} \right)$$

To illustrate the equations \overline{Y}_m and β graphically, it is necessary to specify the parameter values for l_1 , l_2 , h_1 , w_1 , m and z . The parameter l_1 for the compound IA corresponds to the parameter l_1 for the single-stage IA, and thus it is assigned a fixed value of 100mm. The parameter l_2 is another fixed physical dimension of the compound IA, which is assigned a value of 45mm. Through the use of trigonometric relations with reference to Figure 6 the parameter values for h_1 and w_1 can be determined. The calculated values for h_1 and w_1 which correspond to different initial amplifier angles of the primary mechanism ϕ_1 are tabulated in Table 2. Note that different initial amplifier angles are presented as changes to the geometry of IA influence changes to the effective mass of the system. To maintain consistency in the analysis of each IA, the value of m is fixed at 1g. The value of z is selected to vary within the range of -5 and 30mm. This range of displacement is considered realistic, given the dimensions of the compound IA. Figure 7 visually represents the behaviour of \overline{Y}_m and β for the specified values of l_1 , l_2 , h_1 , w_1 , m and z .

Table 2: A table to show the values for the parameters l_1 , l_2 , h_1 and w_1 , for different initial amplifier angles of the primary mechanism. Six cases are shown.

Amplifier Angle ϕ_1 (degrees)	l_1 (mm)	l_2 (mm)	h_1 (mm)	w_1 (mm)
5	100.00	45.00	199.24	8.72
10	100.00	45.00	196.96	17.36
15	100.00	45.00	193.19	25.88
20	100.00	45.00	187.94	34.20
25	100.00	45.00	181.26	42.26
30	100.00	45.00	173.21	50.00

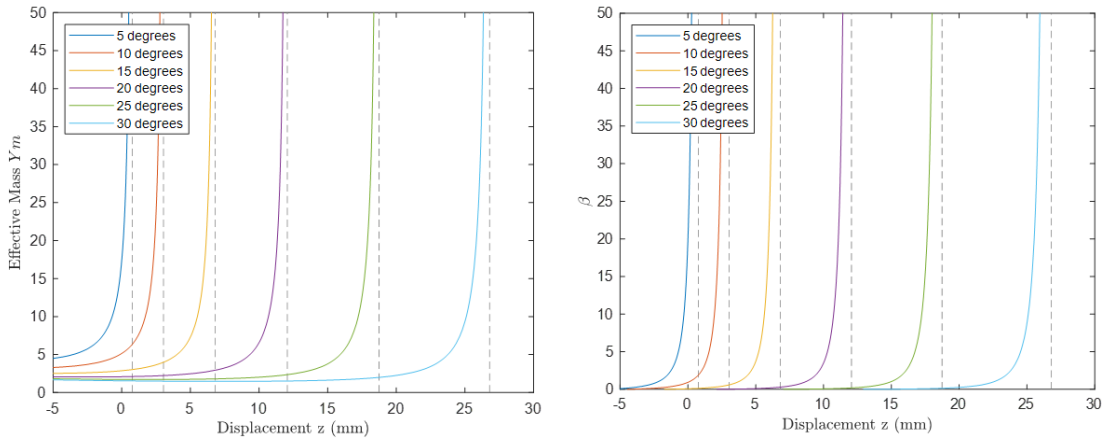


Figure 7: a) Effective mass as a function of the displacement z for the compound IA. b) non-linear velocity coefficient as a function of the displacement z for the compound IA. Six different values for the initial amplifier angle of the primary mechanism Φ_1 are shown in each plot.

The exponential curves depicted in Figure 7a) illustrate the relationship between the compound IAs effective mass and displacement for varying initial amplifier angles of the primary mechanism. When the arms of the compound IA meet the curves tend towards infinity, this is because the motion of the mechanism is at rest. As the compound IA displaces the effective mass rapidly decreases (negative displacement values). Note that the relationship closely resembles that of the single-stage IA, as demonstrated in Figure 5a) of Subsection 3.1.2. The primary contrast between the two mechanisms lies in the rate of change of effective mass with displacement, with the compound IA exhibiting a more rapid rate of change. Additionally, as the initial amplifier angle of the primary mechanism increases, the rate of change becomes more gradual.

The curves shown in Figure 7b) represent the exponential relationship between the compound IAs velocity squared coefficient and displacement for varying initial amplifier angles of the primary mechanism. The general trend shows that as the displacement of the mechanism increases the velocity squared coefficient rapidly decreases. When the arms of the mechanism meet, the displacement stops, and the curves tend towards infinity. It is worth noting that this relationship is similar to that of the single-stage IA, shown in Figure 5b) of Subsection 3.1.2. The main difference between the two mechanisms lies in the rate of change of velocity squared coefficient with displacement, with the compound IA experiencing a more rapid rate of change. Furthermore, as the initial amplifier angle increases, the rate of change of the velocity squared coefficient with displacement becomes slower. The non-linear trend may arise if the restoring force acting on the system is not directly proportional to the displacement of the

system. However, it is difficult to identify the exact cause of this relationship. If the performance of the compound IA is to be optimized, it is crucial to understand this relationship.

3.2.3 Linearised Equation of Motion for the Compound Inertial Amplifier

As stated in Section 3.1.3, the majority of non-linear dynamic systems display linear behaviours over a limited range of motion, rendering linear approximations possible. Linear equations are more straightforward to analyze and manipulate than non-linear equations. Therefore, this Subsection aims to convert the non-linear equation of motion for the compound IA (equation (59)) into a linear approximation. The linearization will be attained by setting the parameters z and \dot{z} , which respectively denote the vertical displacement and the velocity of the system, to approach zero.

As z and \dot{z} tend to 0, equation (59) becomes

$$\frac{d}{dt} \left(\frac{\partial L}{\partial \dot{z}} \right) = m \left(\left(-\frac{2\left(\frac{h_1}{2}\right)^2}{16\left(\left(\frac{h_1}{2}\right)^2 - l_1^2\right)} \right) + \left(\frac{\left(\sqrt{l_1^2 - \left(\frac{h_1}{2}\right)^2} - \frac{w_1}{2} \right) \left(\frac{h_1}{2}\right)}{2 \sqrt{l_2^2 - \left(\sqrt{l_1^2 - \left(\frac{h_1}{2}\right)^2} - \frac{w_1}{2} \right)^2} \sqrt{l_1^2 - \left(\frac{h_1}{2}\right)^2}} + \frac{1}{2} \right) \right)^2 + \left(\frac{\left(\frac{w_1}{2} - \sqrt{l_1^2 - \left(\frac{h_1}{2}\right)^2} \right) \left(\frac{h_1}{2}\right)}{2 \sqrt{l_2^2 - \left(\frac{w_1}{2} - \sqrt{l_1^2 - \left(\frac{h_1}{2}\right)^2} \right)^2} \sqrt{l_1^2 - \left(\frac{h_1}{2}\right)^2}} + \frac{1}{2} \right)^2 \right) \ddot{z}$$

62

Using trigonometry, with reference to Figure 6 the equation simplifies to

$$\frac{d}{dt} \left(\frac{\partial L}{\partial \dot{z}} \right) = m \left(\left(\frac{\cot^2 \phi_1}{8} \right) + \left(\frac{\cot^2 \phi_1 \tan^2 \phi_2}{2} + \frac{1}{2} \right) \right) \ddot{z} = 0$$

63

The linearized equation of motion for the compound IA, represented by equation (63), is an invaluable tool that provides a simplified and more manageable description of the system's behaviour, when compared to the nonlinear equation of motion. This equation highlights three crucial parameters, namely the discrete mass of the system, the initial amplifier angle of the primary mechanism, and the initial amplifier angle of the secondary mechanism. During experimental testing, these parameters will be carefully fine-tuned, as they play a vital role in determining the overall behaviour of the compound IA.

In Table 2 of Subsection 3.2.2, it is shown that the initial amplifier angle of the primary mechanism can be easily adjusted by modifying the height of the mechanism. It is worth noting that the initial amplifier angle of the secondary mechanism is also inherently adjustable, as it is linked to the primary mechanism. Therefore, the initial amplifier angle of the primary mechanism will be tuned through effective geometrical changes, which will inherently adjust the initial amplifier of the secondary mechanism. In contrast, the discrete mass will be adjusted by adding different quantities of proof mass to the system.

3.3 Nested Inertial Amplifier

3.3.1 System Considered and Kinematic Relations

The final mechanism to be considered in this Section is the nested IA, which is shown in Figure 8. The nested IA, like the compound IA, builds upon the structure of the single-stage IA, with the aim to further improve tuning performance. The system is composed of three IAs, which are implanted one inside another. In order to facilitate understanding, the outermost IA will be referred to as the primary mechanism, while the innermost IA will be referred to as the tertiary mechanism, represented by black and green lines in Figure 8, respectively. The IA connecting both the primary and tertiary mechanisms, represented by purple rigid arms in Figure 8, will be named the secondary mechanism.

The primary mechanism of the nested IA is identical to the primary mechanism of the compound IA, which is mentioned in Section 3.2. The secondary mechanism of the nested IA is also similar to the primary mechanism, with the only distinction being a change in the length of the rigid arms. The tertiary mechanism of the nested IA is similar to the single-stage IA, discussed in Section 3.1.1, with the length of the rigid arms again the only difference between the two systems. Together twelve rigid arms establish the shape of the nested IA. The arms all move freely around each joint, which are represented by black dots in Figure 8. At the furthest

left and furthest right joints of the tertiary mechanism, masses m are located. Note that for this analysis, all the component parts which make up the nested IA are considered to have negligible mass, such as the rigid arms, bearings, pins, and brackets. The top and the bottom joints of the nested IA have a free and a fixed connection, respectively, and the separation distance between these two joints defines the amplifier angle of each mechanism. The amplifier angle is denoted by ϕ_1 , ϕ_2 and ϕ_3 , for the primary, secondary and tertiary mechanisms, in the order given. When a force is applied to the vertical plane of the system, the amplifier will move, and a change in ϕ_1 , ϕ_2 and ϕ_3 will occur. The vertical displacement of the system is characterized by z and the horizontal displacement of the system is characterized by x . Since each mechanism resides in an offset plane, there will be no interference during motion.

Similarly, to the single-stage and compound IAs, the nested IA has a symmetric structure; such that the system can be vertically bisected from its free end to its fixed end, as illustrated in Figure 8. The reduced half system will be used to simplify the analysis, since the final dynamic expressions can be duplicated to fulfill the motion of the whole system. Note that the kinematic relations at joints a, b, and c are equivalent amongst the single-stage, compound, and nested IAs.

The geometry of the reduced model is characterized by the parameters height, h , width, w , and length, l , which can be seen in Figure 8. In the same manner, as the compound IA, these parameters are subscripted to indicate the mechanism to which they belong. Subscripts 1, 2, and 3 are used for the primary, secondary, and tertiary mechanisms, respectively. Note that some parameters correspond amongst different mechanisms i.e., the width of the primary and secondary mechanisms, and also the height of the secondary and tertiary mechanisms, therefore the notation, w_1 and h_2 is to be cross utilized. Furthermore, Figure 8 shows that mass m is positioned at joint i, so the notation $m = m_i$ is to be recognized.

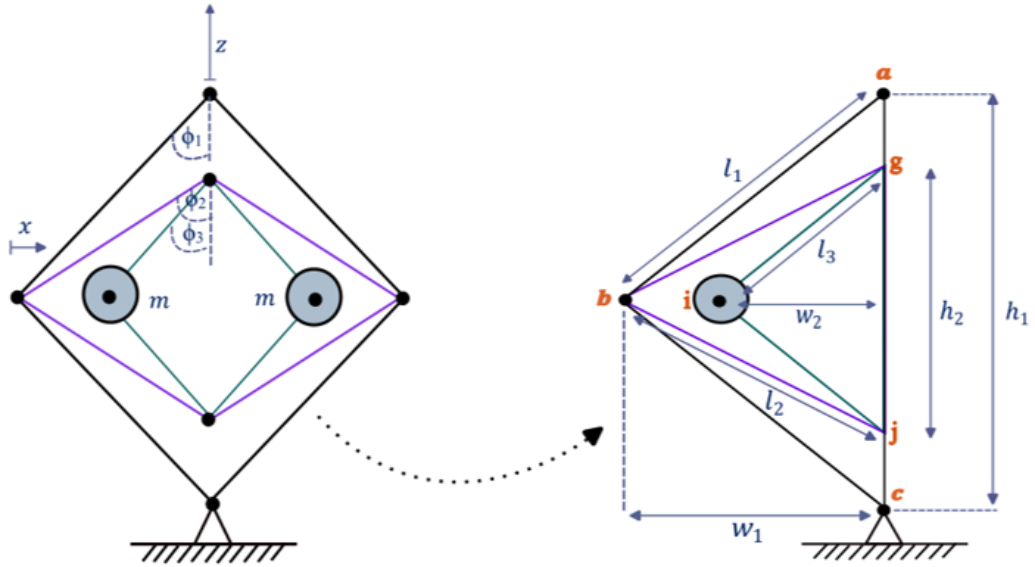


Figure 8: Conversion of the nested inertial amplifier to one-half system.

Much like the analysis for the single-stage IA and the compound IA in Sections 3.1 and 3.2, respectively, the nested IA follows the same analytical approach. The analysis aims to establish the equations of motion for the nested IA, and to do this the Lagrangian function is required to be used. For the Lagrangian function to be satisfied the kinematics at each joint need to be determined, in terms of the vertical displacement of the system, z . Therefore, in this Subsection, the kinematics at each joint will be found and a chain of functions will be written. By relating the geometry of the mechanism to the motion of the system, the kinematic relations at joints a, b, c, g, i, and j are as follows:

Joints a, b and c)

The kinematics at joints a), b) and c), are stated in Subsection 3.1.1; refer to equations (9-19).

Joint g)

The vertical displacement of joint g is given by

$$z_g = \sqrt{l_2^2 - (w_1 - x_b)^2} - \frac{h_2}{2} + z_b \tag{64}$$

The derivation to obtain the vertical displacement of joint e is shown by equations (139-141), which can be found in the appendix, section 8 sub-section 8.1.

For completeness, the horizontal displacement at joint g is given by

$$x_g = 0 \quad 65$$

Equation (64) written as a function of z is obtained as

$$z_g = z_g(x_b, z_b) = z_g(x_b(z_b(z)), z_b(z)) \quad 66$$

Joint j)

The vertical displacement at joint j) is given by

$$z_j = z_b + \frac{h_2}{2} - \sqrt{l_2^2 - (w_1 - x_b)^2} \quad 67$$

The derivation to obtain the vertical displacement of joint e is shown by equations (142-144), which can be found in the appendix, section 8 sub-section 8.1.

The horizontal movement at joint j) is given by

$$x_j = 0 \quad 68$$

Equation (67) written as a function of z is obtained as

$$z_j = z_j(x_b, z_b) = z_j(x_b(z_b(z)), z_b(z)) \quad 69$$

Joint i)

The vertical displacement of the mass at joint i) is given by

$$z_i = \frac{z_a}{2} = \frac{z}{2} \quad 70$$

To find the horizontal displacement x_i of the mass at joint i), Pythagorean theorem is applied to members g-i in Figure 8b).

$$l_3^2 = \left(\frac{h_2}{2} + z_g - z_i\right)^2 + (w_2 - x_i)^2 \quad 71$$

Equation (71) rearranges to give

$$x_i = w_2 - \sqrt{l_3^2 - \left(\frac{h_2}{2} + z_g - z_i\right)^2} \quad 72$$

Equations (70) and (72) written as a function of z become

$$z_i = z_i(z) \quad 73$$

$$x_i = x_i(z_g(x_b(z_b(z)), z_b(z)), z_i(z)) \quad 74$$

3.3.2 Lagrangian Analysis of the Nested Inertial Amplifier

In this Subsection the equations of motion for the nested IA will be derived using the Lagrangian function. The Lagrangian function requires the kinematic relationships at each joint to be established. Thus, the work conducted in Subsection 3.3.1, will be utilized and continued here. The Lagrangian function is defined by equation (20) in Subsection 3.1.2, and based on this equation the kinetic energy of the nested IA is stated below by equation (75), under the assumption that the mass of the system (constituent components) is negligible, except for the mass at joint i), denoted by m_i .

$$T = \frac{1}{2} (m_i (\dot{x}_i^2 + \dot{z}_i^2)) \quad 75$$

In Section 3.1.2, the Euler-Lagrange equation is defined by equation (22). The Euler-Lagrange equation will be used to calculate the equations of motion for the nested IA. The equation expresses the equivalence of the time derivative of the generalized momentum of the system and the derivative of the potential energy of the system. For the nested IA the potential energy of the system is considered zero because there are no elastic elements contained within the mechanism. In addition, the device is intended for use in the horizontal plane, rather than the vertical plane, thus making the gravitational potential energy of the proof mass negligible. Note that the mechanism is orientated in vertical plane in Figure 8, for illustrative purposes only, but it is experimentally analysed in the horizontal plane in Section 5.

$$\frac{\partial L}{\partial z} = \frac{\partial L}{\partial x_i} \frac{\partial x_i}{\partial z} + \frac{\partial L}{\partial z_i} \frac{\partial z_i}{\partial z} = 0 \quad 76$$

The generalized momentum of the system is expressed as

$$\frac{\partial L}{\partial \dot{z}} = \frac{\partial L}{\partial \dot{x}_i} \frac{\partial \dot{x}_i}{\partial \dot{z}} + \frac{\partial L}{\partial \dot{z}_i} \frac{\partial \dot{z}_i}{\partial \dot{z}} \quad 77$$

Which on substitution of terms $\frac{\partial \dot{x}_i}{\partial \dot{z}} = \frac{\partial x_i}{\partial z}$ and $\frac{\partial \dot{z}_i}{\partial \dot{z}} = \frac{\partial z_i}{\partial z}$ and equation (75), together with expansion through the use of the chain and product rule, the equation becomes

$$\frac{\partial L}{\partial \dot{z}} = m_i \left(\dot{x}_i \left(\frac{\partial x_i}{\partial z} \right) + \dot{z}_i \left(\frac{\partial z_i}{\partial z} \right) \right) \quad 78$$

By taking the time derivative of equation (78), the equation follows as

$$\frac{d}{dt} \left(\frac{\partial L}{\partial \dot{z}} \right) = m_i \left(\ddot{x}_i \left(\frac{\partial x_i}{\partial z} \right) + \dot{x}_i \left(\frac{\partial^2 x_i}{\partial z^2} \dot{z} \right) + \ddot{z}_i \left(\frac{\partial z_i}{\partial z} \right) + \dot{z}_i \left(\frac{\partial^2 z_i}{\partial z^2} \dot{z} \right) \right) \quad 79$$

Which on substitution of terms $\dot{x}_i = \frac{\partial x_i}{\partial z} \dot{z}$, $\ddot{x}_i = \frac{\partial x_i}{\partial z} \ddot{z} + \frac{\partial^2 x_i}{\partial z^2} \dot{z}^2$, $\dot{z}_i = \frac{\partial z_i}{\partial z} \dot{z}$, $\ddot{z}_i = \frac{\partial z_i}{\partial z} \ddot{z} + \frac{\partial^2 z_i}{\partial z^2} \dot{z}^2$ and through simplification, equation (79) becomes

$$\frac{d}{dt} \left(\frac{\partial L}{\partial \dot{z}} \right) = m_i \left(\left(\frac{\partial x_i}{\partial z} \cdot \frac{\partial x_i}{\partial z} + \frac{\partial z_i}{\partial z} \cdot \frac{\partial z_i}{\partial z} \right) \ddot{z} + 2 \left(\frac{\partial x_i}{\partial z} \cdot \frac{\partial^2 x_i}{\partial z^2} + \frac{\partial z_i}{\partial z} \cdot \frac{\partial^2 z_i}{\partial z^2} \right) \dot{z}^2 \right) \quad 80$$

The derivatives required to satisfy equation (80) are given by equations (145 -152), which can be found in the appendix, section 8 sub-section 8.1.

Through substitution of m , recall $m = m_i$, and equations (149-152) into equation (80), the equation of motion for the reduced system, shown in Figure 8, can be found. To find the equation of motion for the full nested IA, it is required that the equation of motion for the reduced system be multiplied by a factor of two, to account for the symmetry amongst systems. Through doing this, the equation of motion for the nested IA becomes

$$\frac{d}{dt} \left(\frac{\partial L}{\partial \dot{z}} \right) = m \left(\left(\left(- \frac{\left(\frac{h_1}{2} + \frac{z}{2} \right)^2}{2 \left(\left(\frac{h_1}{2} + \frac{z}{2} \right)^2 - l_1^2 + l_2^2 - l_3^2 \right)} + \frac{1}{2} \right) \ddot{z} + 4 \left(\frac{(l_3^2 - l_2^2 + l_1^2)(z + h_1)}{(4(l_3^2 - l_2^2 + l_1^2) - (z + h_1)^2)^2} \right) \dot{z}^2 \right) \right) \quad 81$$

The equation of motion presented in equation (81), represents the dynamic behaviour of the nested IA. The equation is inherently non-linear due to the fact it contains several complex

functions of z , and has two or more degrees. Note that the equation also includes one linear term, $\frac{m}{2}\ddot{z}$. As described in Sections 3.1.2 and 3.2.2, it is difficult to interpret the full behaviour of a system from an equation of motion that contains both linear and nonlinear terms. Nevertheless, some conclusions about the behaviour of the nested IA can still be drawn based on the parameters in the equation of motion. Notably, the discrete mass of the mechanism, m , the displacement of the system, z , the length of the arms of the primary mechanism, l_1 , the length of the arms of the secondary mechanism, l_2 , the length of the arms of the tertiary mechanism l_3 , and the height of the mechanism, h_1 . These parameters are key variables which will influence the natural frequencies and the amplitudes of motion of the system. In order to understand how these parameters affect the behaviour of the mechanism, the equation of motion can be broken down into two separate components, as shown by equation (37) in Section 3.1.2, which can be expressed graphically. These components are namely the effective mass term, \overline{Y}_m , and the velocity squared coefficient, β . By separately analyzing these components, a deeper understanding of the behaviour of the nested IA can be achieved.

The effective mass term of the nested IA is given by

$$\overline{Y}_m = m \left(-\frac{\left(\frac{h_1}{2} + \frac{z}{2}\right)^2}{2\left(\left(\frac{h_1}{2} + \frac{z}{2}\right)^2 - l_1^2 + l_2^2 - l_3^2\right)} + \frac{1}{2} \right) \quad 82$$

The velocity squared coefficient of the nested IA is given

$$\beta = 4m \left(\frac{(l_3^2 - l_2^2 + l_1^2)(z + h_1)}{(4(l_3^2 - l_2^2 + l_1^2) - (z + h_1)^2)^2} \right) \quad 83$$

In order to graphically illustrate the behaviour of each equation, \overline{Y}_m and β , the parameter values for l_1 , l_2 , l_3 , h_1 , m , and z need to be specified. The parameter l_1 for the nested IA corresponds to the parameter l_1 for the compound and single-stage IAs, and thus it is assigned a fixed value of 100mm. The parameters l_2 and l_3 are fixed physical dimensions which are assigned the values 80mm and 60mm, respectively. To determine the value of the parameter h_1 , trigonometric relationships are utilized with reference to Figure 8 b). The calculated value for h_1 corresponding to different initial amplifier angles of the primary mechanism ϕ_1 is tabulated in Table 3. To maintain consistency between the analysis of each IA, the value of m is fixed at 1g. The value of z on the other hand will range between -40 and 10mm, this is to

show the full range of motion for the nested IA. Figure 9 visually represents the behaviour of \bar{Y}_m and β for the specified values of l_1, l_2, l_3, h_1, m and z .

Table 3: A table to show the values for the parameters l_1, l_2, l_3 and h_1 , for different initial amplifier angles. Six cases are shown.

Amplifier Angle ϕ_1 (degrees)	l_1 (mm)	l_2 (mm)	l_3 (mm)	h_1 (mm)
5	100.00	80.00	60.00	199.24
10	100.00	80.00	60.00	196.96
15	100.00	80.00	60.00	193.19
20	100.00	80.00	60.00	187.94
25	100.00	80.00	60.00	181.26
30	100.00	80.00	60.00	173.21

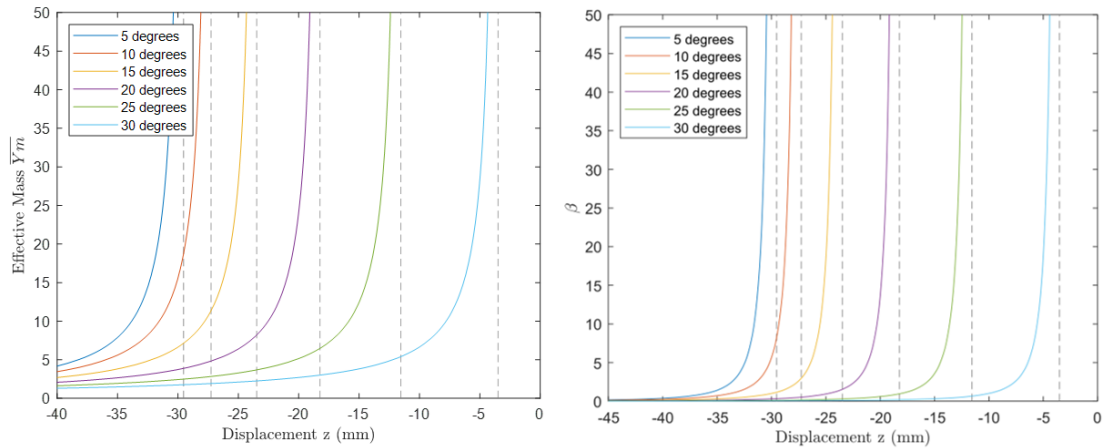


Figure 9 a) Effective mass as a function of the displacement z for the nested IA. b) Non-linear velocity coefficient as a function of the displacement z for the nested IA. Six different values for the initial amplifier angle ϕ are shown in each plot.

Figure 9a) illustrates the relationship between the displacement of the nested IA and its effective mass, for various initial amplifier angles of the primary mechanism. The graph indicates that as the displacement of the mechanism increases (shown by negative displacement values), the effective mass exponentially decreases. When the displacement of the mechanism stops the curves tend towards infinity. This trend is notably similar to that of the single-stage IA and compound IA, as depicted in Figure 5a) and Figure 7a) of Subsections 3.1.2 and 3.2.2, respectively. However, there is a distinct difference in the relationship between the effective mass and displacement for each type of IA, concerning the rate of

change. The nested IA exhibits a more gradual rate of change of effective mass with displacement than the compound IA, but a faster rate of change than the single-stage IA.

Figure 9b) illustrates an exponential relationship between the velocity squared coefficient and the displacement of the nested IA, for different initial amplifier angles of the primary mechanism. The curve shows that as the displacement of the mechanism increases (indicated by negative displacement values), the velocity squared coefficient rapidly decreases. When the displacement of the mechanism stops the curves tend towards infinity. It is worth noting that the relationship is similar to that of the single-stage IA and compound IA, as depicted in Figure 5b) and Figure 7b) of Subsections 3.1.2 and 3.2.2, respectively. The primary contrast between the three mechanisms lies in the rate of change of the velocity squared coefficient with displacement. The nested IA exhibits a slower rate of change than the compound IA but a faster rate of change than the single-stage IA. Note that the rate of change of velocity squared coefficient with displacement also changes, for different initial amplifier angles of the primary mechanism. The trend may be caused by a restoring force acting on the system that is not directly proportional to the displacement of the system. However, it is challenging to recognize the exact cause of this relationship.

3.3.3 Linearised Equation of Motion for the Nested Inertial Amplifier

As stated in Section 3.1.3 and 3.1.2, the majority of non-linear dynamic systems display linear behaviours over a limited range of motion, rendering linear approximations possible. Linear equations are more straightforward to analyse than non-linear equations. Therefore, this Subsection aims to convert the non-linear equation of motion for the nested IA (equation 81) into a linear approximation. Linearization will be attained by setting the parameters z and \dot{z} , which respectively denote the vertical displacement and the velocity of the system, to approach zero.

As z and \dot{z} tend to 0, equation (81) becomes

$$\frac{d}{dt} \left(\frac{\partial L}{\partial \dot{z}} \right) = m \left(- \frac{\left(\frac{h_1}{2} \right)^2}{2 \left(\left(\frac{h_1}{2} \right)^2 - l_1^2 + l_2^2 - l_3^2 \right)} + \frac{1}{2} \right) \ddot{z} = 0 \quad 84$$

In comparison with the non-linear equation of motion, equation (81), the linearized equation of motion for the nested IA, shown in equation (84), is a very useful tool as it provides a more

comprehensible explanation of the behaviour of the system. This equation draws attention to five crucial variables which are the length of the arms of the primary, secondary, and tertiary mechanisms, the height of the overall nested IA, and the system's discrete mass. As outlined in Section 3.3.2, the length of each arm of the nested IA is a fixed physical dimensions. Therefore, during experimental testing the height of the nested IA will be tuned, as well as the discrete mass of the system. According to Table 3, modifying the height of the mechanism will alter the initial amplifier angle of the primary mechanism. Therefore, the initial amplifier angle of the primary mechanism will be tuned through effective geometrical changes. Note that tuning this parameter will inherently adjust the initial amplifier of the secondary and tertiary mechanisms. In contrast, the discrete mass will be adjusted by changing the quantity of proof mass added to the system.

4. Design, Manufacturing and Assembly Process

In this Section, the physical realisation of all six IAs will be described. To physically realize each IA, the individual component parts of each mechanism must be sourced, or designed and manufactured, before being assembled. Such parts include the arms of the mechanism, bearings, pins, screws, bolts, brackets and proof mass. To ensure that this work is reproducible, readily available off-the-shelf component parts will be utilised wherever possible. These component parts will be used in their standard form, without any modifications, so that they can be easily obtained and used by other researchers. For any parts that are not commercially available, custom-designed parts will be created, which will be compatible with the off-the-shelf components. By employing this approach, the experimental setup will be as reproducible as possible, allowing other researchers to replicate the experiment and build upon the findings in this work.

To develop each IA, the component parts will be modelled using Solidworks, a 3D computer aided design (CAD) software. The use of Solidworks will allow for a thorough investigation of various design possibilities and iterations, prior to the commencement of the production process. Additionally, Solidworks is capable of creating assembly models of parts. This feature will be used to help visualise how each IA's component parts will fit together and interact. If any issues arise such as the interference of parts, the individual part models will be adjusted accordingly. The application of Solidworks will ultimately save significant time and resources in the physical production process. Figure 10 outlines the CAD process which will be followed for each IA.

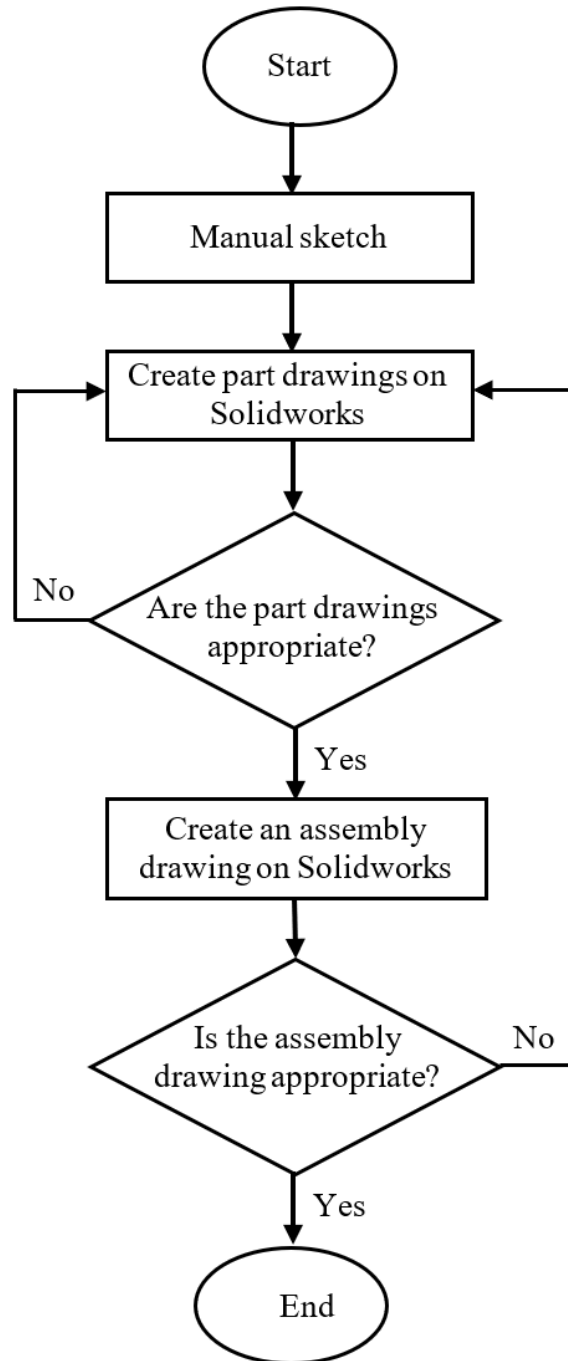


Figure 10: A flowchart outlining the design process followed to model each IA.

Upon completion of the design process and validation of the CAD models, the manufacturing stage will commence. Commercial components will be procured, while custom-made parts will be additively manufactured, more specifically 3D printed. Note that all custom-made parts will be 3D printed from the material acrylonitrile butadiene styrene (ABS), which is a type of plastic known for its strength and durability. Once the parts are manufactured, they will then be assembled. One potential issue with 3D printing is that the layer-by-layer printing process

can produce dimensional inaccuracies. Therefore, if the parts do not fit together postprocessing steps like sanding may be necessary, to refine the final dimensions. It is important for the component parts to fit flush together, eliminating any potential source of vibration that may arise from the assembly. Even slight misalignments can result in unwanted motion when the system is displaced.

4.1 Component Parts of Each Inertial Amplifier

This Subsection provides a description of the constituent parts which form each IA. While each IA consists of the same fundamental components, variations in the quantities, dimensions, and design features of these parts occur amongst mechanisms. To see the full assembly of each IA, proceed to Subsection 4.2, Figure 21, Figure 22 and Figure 23.

4.1.1 Arms

The structural configuration of the single-stage, single-stage truss, compound, compound truss, nested and nested truss IAs is defined by the arms. The arms are designed based on the dimensions of the bearings, specifically the 694ZZ deep groove ball bearings mentioned in Subsection 4.1.2. These bearings have an outer diameter of 11mm and a width of 4mm. To connect the arms together, to form the structures of each mechanism, two 11mm diameter holes must be housed at each end of each arm. Additionally, the thickness of each arm must be 4mm to align with the bearing width of 4mm.

The single-stage and single-stage truss IAs have an identical structural configuration, as do the compound and compound truss IAs, and the nested and nested truss IAs. To differentiate between corresponding mechanisms, the arms incorporate a distinct design feature. The arm design of the single-stage, compound and nested IAs features a standard, solid structure, while the arms of the corresponding mechanisms share the same design but incorporate truss shaped cut-outs. The rationale behind employing two different arm designs in this work, is to evaluate how a slight design modification of the mechanisms will impact the response of a dynamic system, specifically a cantilever beam.

The IAs featuring arms with truss shaped cut-outs will exhibit a reduction in their overall mass, compared to the IAs with solid arms. This decrease in mass has the potential to increase the natural frequency of the system since there is less mass to move or accelerate. On the other hand, a reduction in mass could decrease the stiffness of the system since there is less material to resist deformation, causing a decrease in the natural frequency of the system. Moreover, the

reduction in mass could also lead to a decrease or an increase in damping, depending on the amount of resistance to motion due to air resistance. The impact of the truss-shaped cut-outs on the system is not easily predictable, and by conducting experiments on the mechanisms, it will be possible to draw conclusions about the effects of the design variant on the dynamic response.

The single-stage and single-stage truss IAs are characterized by a rhombus shaped structure, consisting of four arms each. The length of each arm is 117mm, with a distance of 100mm from the centre of one bearing to the centre of the opposite bearing, as depicted in Figure 11. The compound and compound truss IAs contain ten arms each. Among the ten arms, four arms are identical to the arms of the single-stage and single-stage truss IAs. These four arms connect together to form an external rhombus structure. The remaining six arms form a pantograph mechanism, which connect within the external rhombus structure. There are four short arms with a length of 62mm, and a distance of 45mm from the centre of one bearing to the centre of the opposite bearing, as shown in Figure 12. The remaining two arms are classified as long arms, which have a length of 107mm and a distance of 45mm from the centre of one bearing to the centre of the adjacent bearing, as illustrated in Figure 13. It should be noted that the two long arms house three bearings, two at each end of the arm and one at the centre of the arm. The central hole serves as the connection point for each of the long arms, which combine to form the pantograph structure.

The nested and nested truss IAs comprise twelve arms, four of which are identical to the compound and compound truss IAs, and the single-stage and single-stage truss IAs, which can be seen in Figure 11. These four arms construct to form an outer rhombus structure. An additional four arms have a length of 97mm, and a distance of 80mm from the centre of one bearing to the centre of the opposite bearing, as shown in Figure 14. These four arms connect to form a secondary rhombus mechanism within the outer rhombus structure. The remaining four arms have a length of 77mm, and a distance of 60mm from the centre of one bearing to the centre of the adjacent bearing, as depicted in Figure 15. These arms join together to configure a tertiary rhombus structure, within the secondary rhombus mechanism.

Once the design of each arm is validated, the arms are fabricated using a 3D printer. In case of any manufacturing error, the affected arms are to be remanufactured. Additionally, any undersized bearing holes that may be present among the arms, are to be sanded to guarantee a flush fit for the respective 694ZZ deep groove ball bearings. To assemble the bearings into the arms a push fit technique is used.

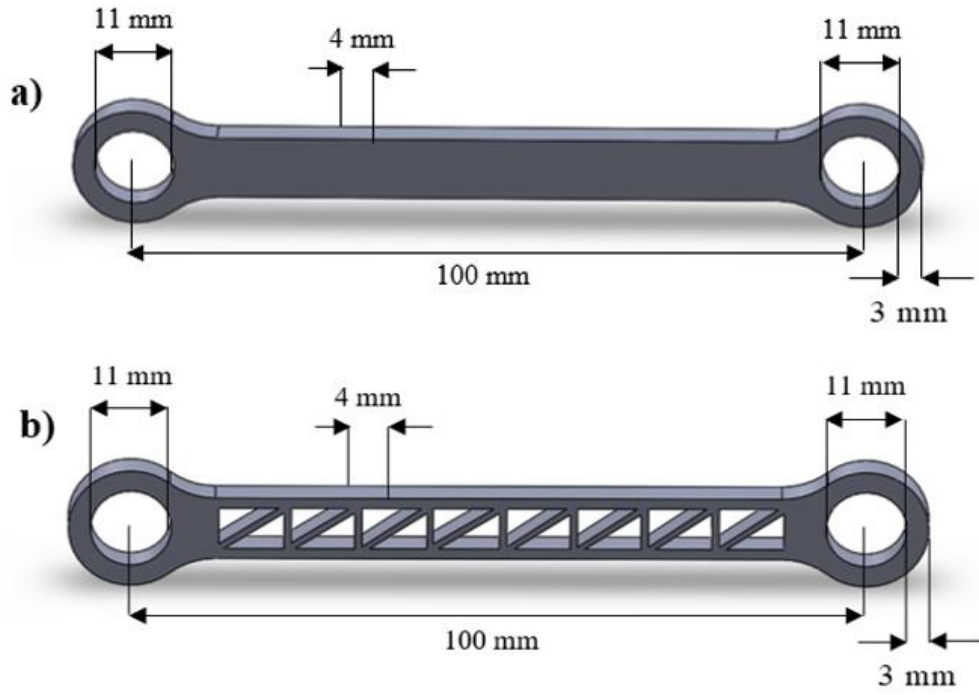


Figure 11: a) One outer arm of the single-stage, compound and nested IAs. b) One outer arm of the single-stage truss, compound truss and nested truss IAs.

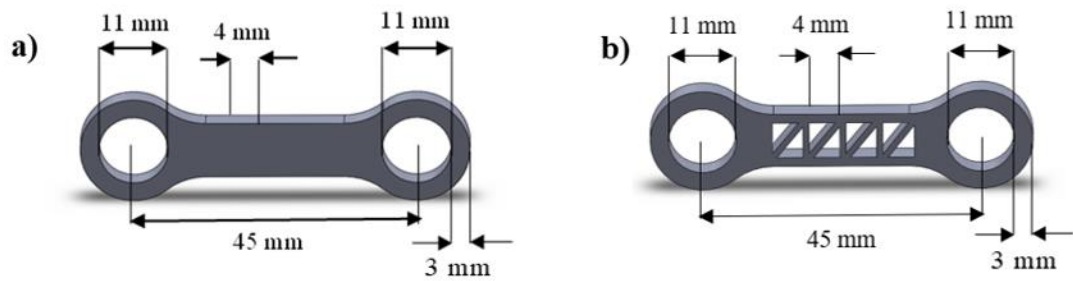


Figure 12: a) One short arm of the compound IA. b) One short arm of the compound truss IA.

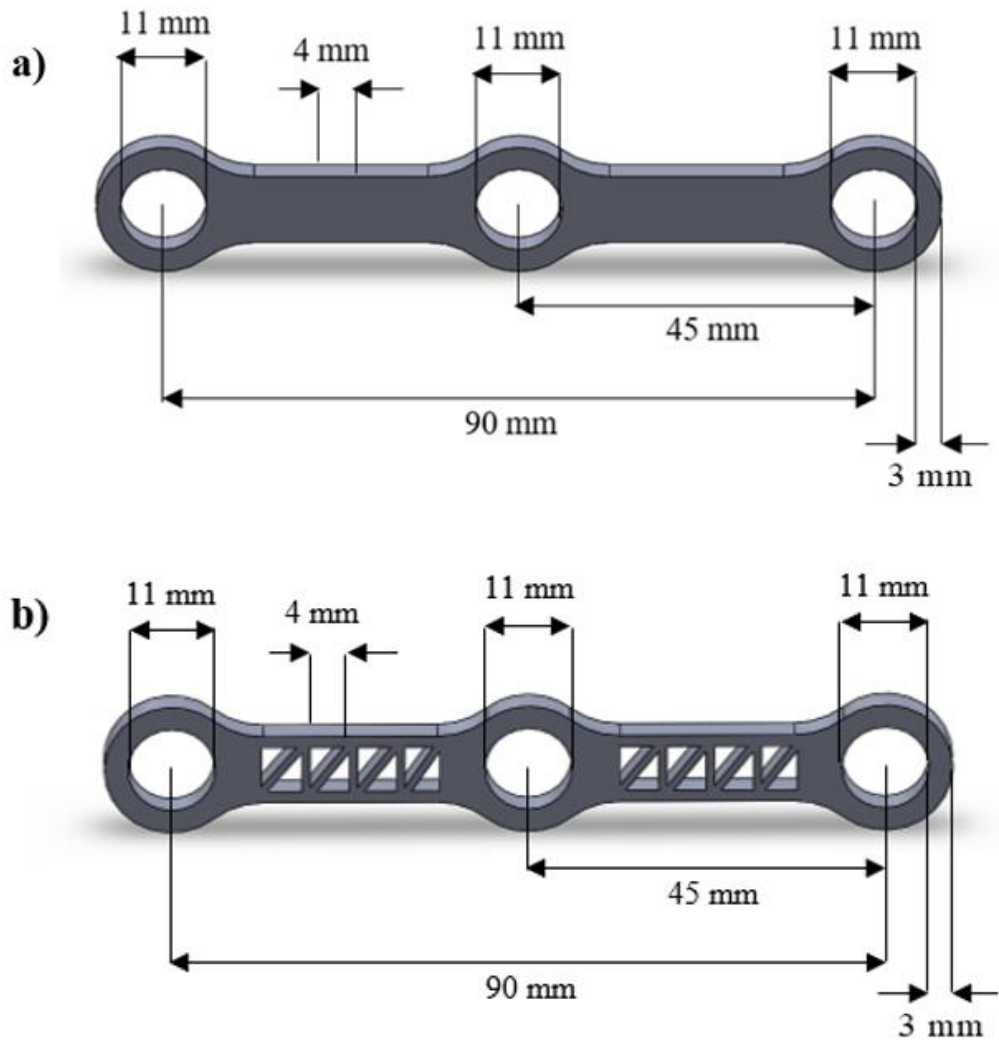


Figure 13: a) One long arm of the compound IA. b) One long arm of the compound truss IA.

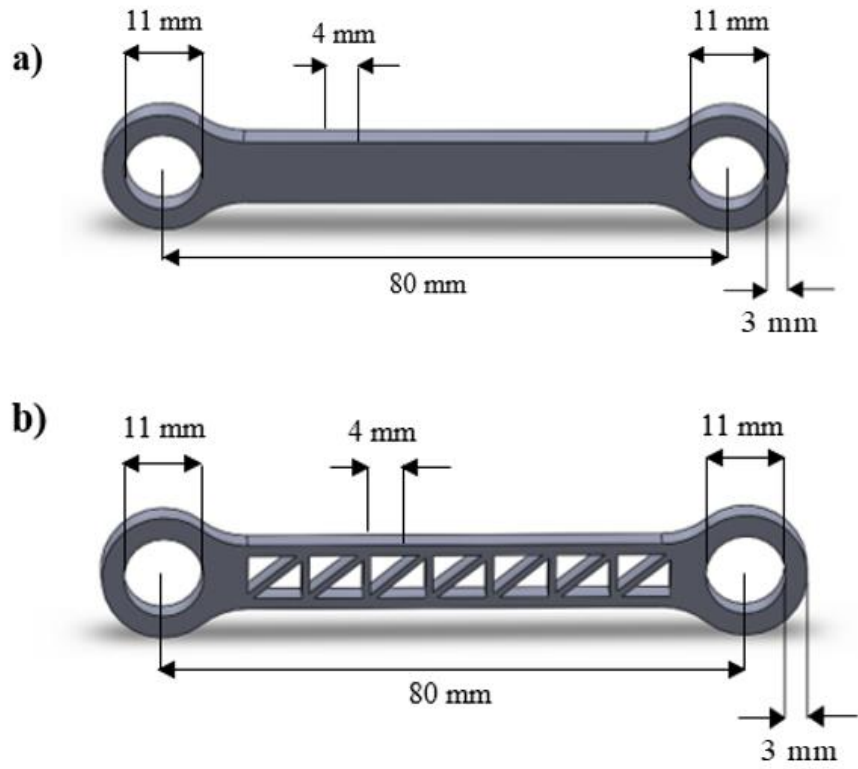


Figure 14: a) One secondary arm of the nested IA. b) One secondary arm of the nested truss IA

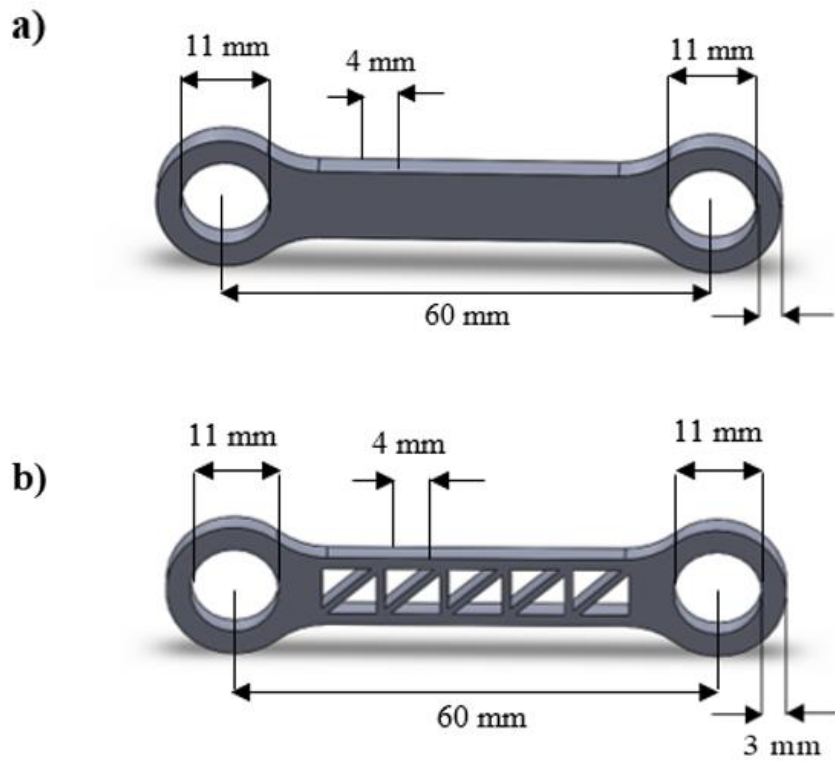


Figure 15: a) One tertiary arm of the nested IA. b) One tertiary arm of the nested truss IA.

4.1.2 Deep Groove Ball Bearings

Deep groove ball bearings are utilized in each IA to reduce friction at the joints. The bearings are fitted into both ends of each arm using a push-fit method. Note that the two long arms of the compound IA house three bearings, as mentioned in Subsection 4.1.1. Through the use of bearings, the arms are able to move with minimal resistance around the pins, which are described in Subsection 4.1.3. The bearings contain a series of steel balls which are placed between two rings, an inner ring and an outer ring. As the arms rotate around the pins, the balls roll along the raceway of the inner and outer rings. The rolling motion of the balls distributes radial and axial loads evenly, which helps to reduce the amount of contact between the inner ring of the bearing and the pin, and minimises friction which would otherwise be prominent. The implementation of bearings to minimize friction can reduce the deterioration of the arms and pins, by impeding direct contact between them. Furthermore, the amount of force needed to facilitate the rotation of the arms around the pins can be reduced, which enhances the free and unhindered motion of each IA.

A wide range of industrial supply stores offer deep groove ball bearings in numerous sizes, suitable for a diverse array of applications. The size of such bearings is generally determined by the inner diameter, outer diameter, and width. Specifically, this study employs 694ZZ deep groove ball bearings, which measure 4mm x 11mm x 4mm, as shown in Figure 16. The single-stage and single-stage truss IAs use eight deep groove ball bearings, while the compound IA, compound truss IA, nested IA, and nested truss IA use twenty-two.

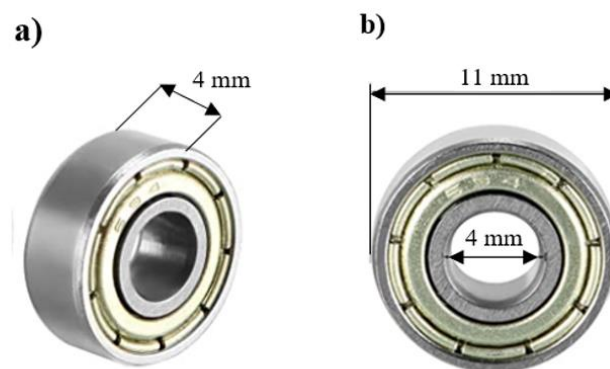


Figure 16: a) An image which indicates the width of a 694ZZ deep groove ball bearing. b) An image which shows the inner and outer diameters of a 694ZZ deep groove ball bearing.

4.1.3 Pins

To facilitate the rotational movement of each arm around a shared axis, pins are installed within each IA. These pins serve as joints that preclude any translation or sliding linear motion. The pins are specifically designed to fit through the 4mm inner diameter hole of each bearing, with assembly being executed through a push-fit method. The lengths of the pins vary amongst joints, contingent on the number of components that must be connected. Figure 17 illustrates a 4mm diameter pin with a given length, L . It should be noted that the components to be joined are invariably the arms, while at the upper and lower joints of each IA, the brackets must also be housed by the pins. The brackets are detailed in Subsection 4.1.4. The utilization of pins to form joints confers a number of benefits compared to alternative types of joints, including a straightforward assembly, a lightweight structure, and improved flexibility and range of motion.

ABS round rods, measuring 4mm x 500mm, are commercially procured to serve as pins in this work. The round rods are industrially produced by extruding melted ABS plastic pellets through a round die. This extrusion process may cause minor inaccuracies in the diameters of the rods. Given that it is essential to obtain a precise 4mm fit between the pins and the bearings, and the pins and the brackets, sanding the rods may be necessary. To determine the lengths of the pins for each IA, a CAD assembly of each IA is created, including all components except for the pins. The components are arranged symmetrically, and as closely together as possible without causing any interference. This allows the distance between each component to be measured. The required lengths for the pins are then based on these measured distances. To manufacture the necessary pin lengths, the ABS rods are measured, marked, and cut using a ruler, scribe, and tenon saw, respectively. Crucial information regarding the requisite pin lengths, corresponding pin types, and pin quantities for the various joints of the single-stage and single-stage truss IAs, the compound and compound truss IAs, as well as the nested and nested truss IAs, is presented in Table 4, Table 5 and Table 6, respectively. It should be noted that the pin type pertains to the number of pins with different lengths. The pin type can provide valuable assistance during the assembly of each IA, indicating the location of specific pins on the mechanism. This information is illustrated in Figure 21a), Figure 22a), and Figure 23a), which can be found in Subsection 4.2.

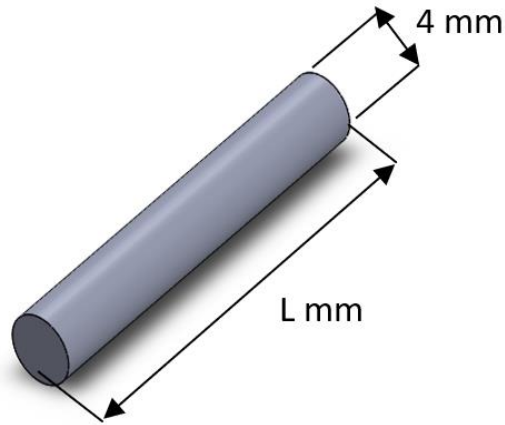


Figure 17: A 4mm diameter ABS pin, which is used to form each joint in each IA.

Table 4: Pin specifications for the single-stage and single-stage truss IAs

Pin Type	Length (L) mm	Quantity
1	25.00	2
2	14.00	2

Table 5: Pin specifications for the compound and compound truss IAs

Pin Type	Length (L) mm	Quantity
1	25.00	1
2	21.00	2
3	11.40	2
4	31.80	1
5	17.40	2
6	37.00	1

Table 6: Pin specifications for the nested and nested truss IAs

Pin Type	Length (L) mm	Quantity
1	25.00	2
2	46.60	2
3	58.00	1
4	31.50	2
5	78.20	1

4.1.4 Brackets

To form each IA, arms, bearings, and pins are required, which are outlined in Subsections 4.1.1, 4.1.2, and 4.1.3, respectively. However, to use each IA in an application one end of each mechanism must be fixed to the ground and the other end must be attached to a dynamic system. In this work, a bracket has been designed as an intermediary component to connect each IA to either the ground or a system. Note that the dynamic system used in this study is a cantilever beam, which is outlined in Subsection 4.1.5

To ensure seamless integration of the bracket with the other constituent components in the system, careful consideration must be given to its design and dimensions. Figure 18 shows a CAD model of the designed bracket, with the part dimensions specified. The design process requires taking into account the dimensions of the other components and their spatial relationships within the system. For instance, a 2.5mm diameter stainless steel TX pan machine screw is used to attach the base of the bracket to the beam or the ground. Consequently, the holes in the base of the bracket must have a diameter of 2.5mm. Additionally, each bearing has an inner diameter of 4mm, therefore the pins must have a diameter of 4mm. As a result, the bracket requires a 4mm diameter hole to accommodate the pins.

Furthermore, each bearing has an outer radius of 5.5mm, while the casing of each arm, which holds the bearing in place, has a diameter of 3mm. As a result, the distance from the centre of the 4mm pin hole to the top of the base of the bracket must measure greater than 8.5mm. Note that this distance is given by 15mm to allot extra room, to facilitate an easier assembly. Moreover, the width of the cantilever beam is 30mm, as stated in Subsection 4.1.5, therefore the width of two brackets must be less than 30mm. Finally, the column of the bracket is aligned in a central position with the length of the base plate, which measures 35mm, but not with its width of 11.5mm. This particular arrangement has been adopted to provide additional space for the arms to fit seamlessly along the pins without the risk of interference.

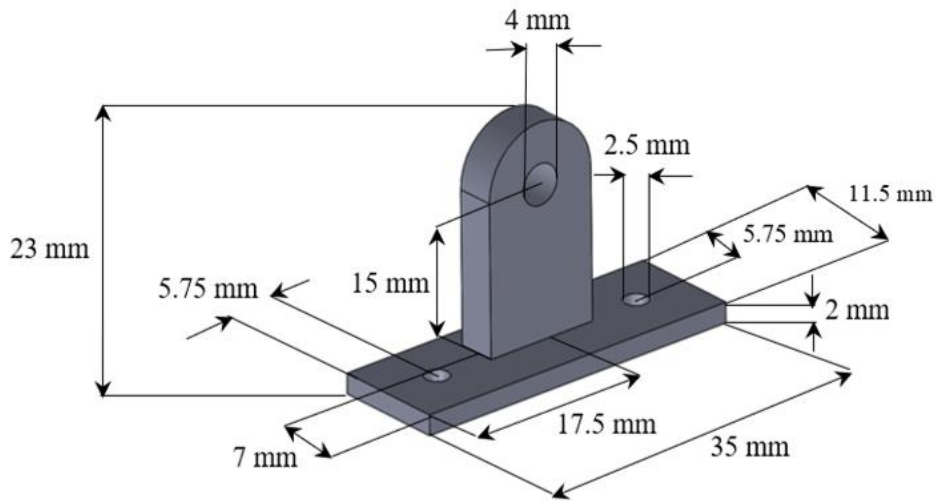


Figure 18: CAD model of the designed bracket, with the part dimensions specified.

Each IA requires a total of four brackets, two to attach each IA to ground and two to attach each IA to the cantilever. Given that the brackets are secured using M2.5 (2.5mm x 20mm) stainless steel TX pan machine screws and M2.5 hexagonal nuts, and not adhesive glue, only four brackets need to be 3D printed as they can be easily removed and reutilized amongst mechanisms. This approach reduces material costs. Once the brackets have been 3D printed, any undersized screw and pin holes are sanded to facilitate a proper fit for the respective screws and pins.

4.1.5 Cantilever Beam

A cantilever beam is a structural member that is rigidly supported at one end while its other end remains free. Such a beam can be analysed as a single-degree-of-freedom dynamic system. Figure 19 shows a CAD model of the cantilever beam used in this work, with the dimensions explicitly defined. By first determining the natural frequency of the cantilever beam and then attaching each IA to it, the influence of the latter on the cantilevers dynamic response can be evaluated. This will offer valuable insight into the expected performance of each IA in a real-world application.

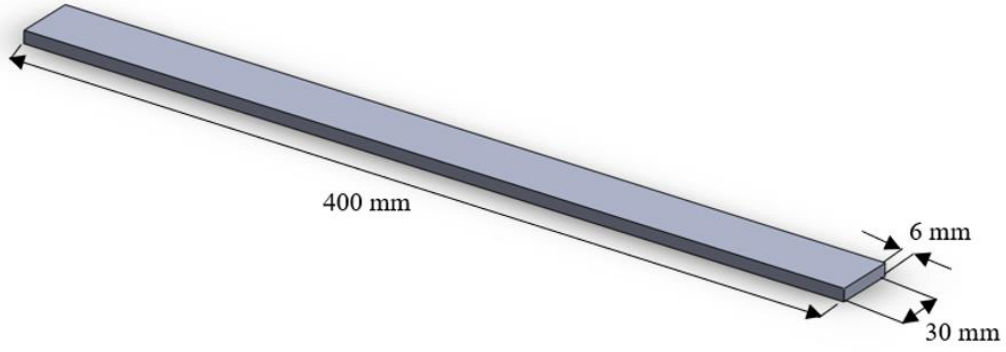


Figure 19: A CAD model of the cantilever beam used in this work, with the dimensions explicitly defined.

The selection of the cantilever's dimensions is predicated on the size of the available 3D printer, which restricts the cantilever's length to 400mm. Moreover, the cantilever's thickness must be relatively small to facilitate the deflection of the beam. Therefore, the thickness of the beam is chosen to measure 6mm. Furthermore, the cantilever's width is selected based on the length and thickness values, this dimension is given as 30mm. It is worth noting that despite the cantilever's actual length of 400mm, a margin of 100mm is set aside for clamping the beam, during experimental testing. Thus, the effective length of the cantilever is 300mm. It is sufficient to additively manufacture only one cantilever, as the same cantilever can be employed across all experiments.

It is possible to calculate the first natural frequency of the cantilever beam, through utilising the dimensions and the material properties of the cantilever. The undamped first natural frequency (Hz) for a cantilever beam is given by

$$w_1 = \frac{k_1^2}{2\pi} \sqrt{\frac{EI}{\rho AL^4}} \quad 85$$

Where w_1 is the first natural frequency, k_1 is the first fundamental mode of vibration which is equivalent to 1.875 [124], E is the Young's modulus, I is the second moment of area, ρ is the material density, A is the cross-sectional area and L is the length of the cantilever.

The second moment of area for a cantilever beam can be calculated using the following equation

$$I = \frac{bh^3}{12} \quad 86$$

By entering the dimensions of the cantilever beam employed in this study into equation (86), the second moment of area can be obtained.

$$I = \frac{0.03 * 0.006^3}{12} = 5.4 * 10^{-10} m^4 \quad 87$$

The Young's modulus and density are inherent material properties. In this work, the cantilever is manufactured from ABS, the Young's modulus of ABS is $2 * 10^9$ Pa and the density of ABS is 1020 Kg/m^3 . Using equation (85) and the parameter values for k_1 , E , I , ρ , A and L , the first natural frequency of the cantilever beam is calculated.

$$w_1 = \frac{1.875^2}{2\pi} \sqrt{\frac{(2 * 10^9) * (5.4 * 10^{-10})}{1020 * 0.006 * 0.03 * 0.3^4}} = 15.08 \text{ Hz} \quad 88$$

It should be noted that the calculated natural frequency of the cantilever beam may deviate from the natural frequency value determined during experimental testing. This discrepancy may be attributed to the inherent nature of the 3D printing technique used to manufacture the cantilever, which typically does not produce entirely solid structures. Additionally, to experimentally test each IA modifications need to be made to the structure of the cantilever, which may also contribute to any observed discrepancy in the natural frequency. Such modifications include drilling four 2.5mm diameter holes into the free end of cantilever. These holes will facilitate the attachment of each IA to the cantilever through the use of M2.5 stainless steel TX pan machine screws. To perform the drilling process, two brackets are placed at the tip of the cantilever. One bracket is aligned to one side, and end edge, of the cantilever, and the other bracket is aligned to the opposite side, and end edge, of the cantilever. Once aligned the position of the screw holes in the bracket are scribed onto the cantilever. After they have been marked, the holes are made using a hand drill with a 2.5mm drill bit.

4.1.6 Proof Mass

A proof mass is a predetermined quantity of mass that can be added to, or incorporated into, a system. During experimental testing, each IA will be coupled to a cantilever beam and a proof mass will be added to the system. A proof mass will be placed at either the tip of the

cantilever, or at specific joints of each IA, which are specified in Sections 3.1.1, 3.2.1, and 3.3.1. It is important to note that the quantity of proof mass added to either the tip of the cantilever or to the specific joints of each IA will be subject to variation.

In this work, circular lead disks with a diameter of 25mm and a mass of 12g are employed as proof mass. Figure 20 shows an image of one circular lead disk. The disks can be obtained from Amazon, a multinational e-commerce corporation, in a pack of 20, with a total mass of 240g. To vary the amount of proof mass, which is added to the system, the disks can be cut to decrease mass or combined together to increase mass. It should be noted that the disks will be weighed prior to their addition to the system, since manipulation can result in changes to their mass. The lead disks will be added to the system using super glue, a high strength adhesive.

The experiment employs proof mass to investigate the impact it will have on the dynamic characteristics of the cantilever beam. The proof mass is anticipated to enhance the effective inertia and effective mass of the system, thereby lowering the natural frequency of the cantilever. This is due to its capability to produce force or motion in response to an input. Additionally, the presence of the proof mass is expected to dampen any vibration, to reduce the amplitude of resonances.



Figure 20: An image of one 12g circular lead disk, with a diameter of 25mm [125]

4.2 Assembly

Upon completion of the design and manufacturing process, all parts of each IA, must be assembled. The parts must be joined together in a particular sequence which is provided below:

1. Place two 694ZZ bearings into the end of each arm, and one additional bearing into the centre of each long arm of the compound and compound truss IAs, using a push-fit technique.
2. Next, implement a push-fit methodology to insert the pins through the bearings in the arms, taking care to match the correct pins with the corresponding arms. This selection is based on the lengths of the pins, as well as the designs and lengths of the arms. To determine the specific pairing of the pins and the arms, consult the explanations provided in Subsections 4.1.1 and 4.1.3, along with the Figures labelled Figure 21a), Figure 22a), and Figure 23a) below. Also note that every pin will house at least two arms.
3. Position the arms along each pin such that there is no contact between them, while also guaranteeing that the structure of each mechanism is vertically symmetric when viewed from the side. This is exemplified in Figure 21b), Figure 22b), and Figure 23b).

Once the above steps are complete, each IA will be assembled. To attach an individual IA to a cantilever beam, proceed to use the method provided below:

4. Push-fit two brackets onto the top and the bottom pins of an IA, with one bracket located at each end of each pin. Ensure that each bracket is correctly orientated, with the 4.5mm distance between the side of the bracket and the centre of the column of the bracket facing away from, and not into, the mechanism.
5. Thread two M2.5 TX Pan Machine Screws into each bracket.
6. Next, thread all four screws located at one end of the IA into the corresponding holes of the cantilever beam.
7. Secure each screw of the system, eight in total, with an M2.5 Hexagonal nut. Tighten each nut using small pliers.

To ensure that an IA is adequately prepared for experimental testing, it is necessary to follow steps four through seven. It is important to note that only one IA can be tested at a time owing to the limited availability of equipment. To test a different IA, the IA that has been tested must first be removed from the cantilever. This can be done by employing pliers to loosen all four hexagonal nuts that secure the IA to the cantilever, followed by unthreading the IA from the system. The next IA can then be affixed to the cantilever beam by repeating steps four through seven. CAD models of the assembled IAs can be seen in Figure 21, Figure 22, and Figure 23.

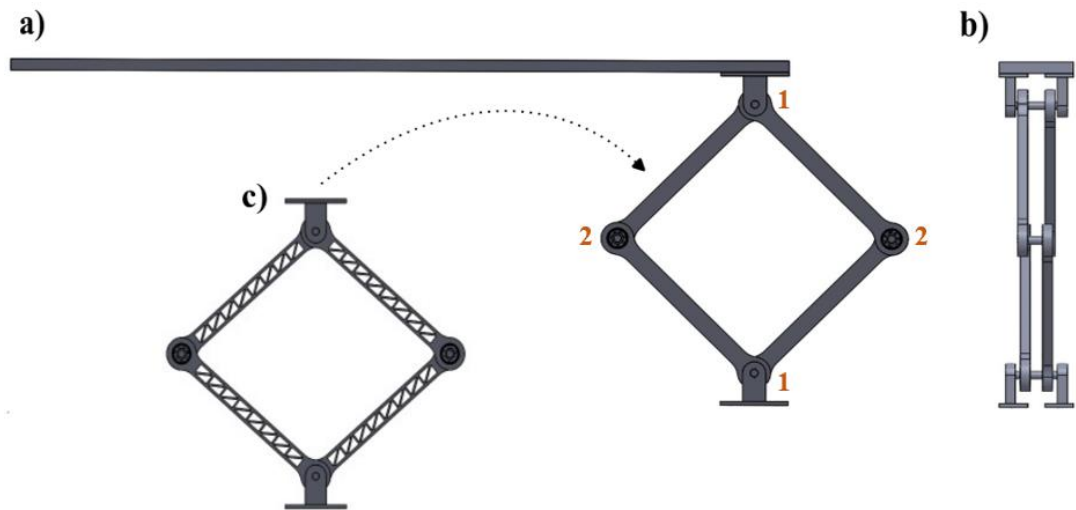


Figure 21: a) A front view CAD assembly model of the single-stage IA attached to a cantilever beam. b) A side view CAD assembly model of the single-stage IA. c) A front view CAD assembly model of the single-stage truss IA.

The numbers in Figure 21a) correspond to the different pin types used at each joint of the single-stage IA. The pin types can be cross-referenced with Table 4 in Subsection 4.1.3. to determine the pin lengths at each joint. Note that the pin types are equivalent among corresponding mechanisms, as mentioned in Subsection 4.1.3.

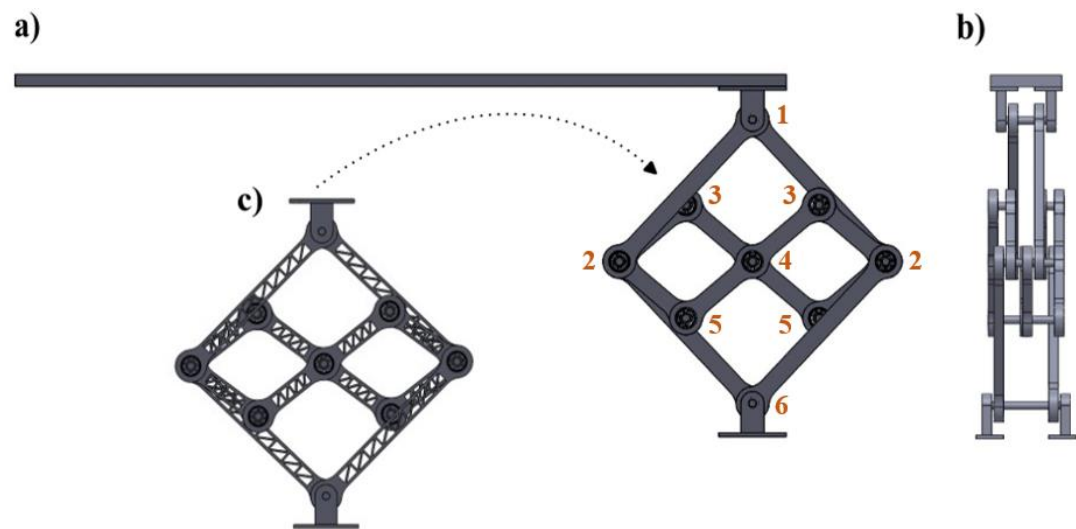


Figure 22: a) A front view CAD assembly model of the compound IA affixed to a cantilever beam. b) A side view CAD assembly model of the compound IA. c) A front view CAD assembly model of the compound truss IA.

The numbers in Figure 22a) correspond to the different pin types used at each joint of the compound IA. The pin types can be cross-referenced with Table 5 in Subsection 4.1.3. to determine the pin lengths at each joint. Note that the pin types and their positions are equivalent for the compound truss IA.

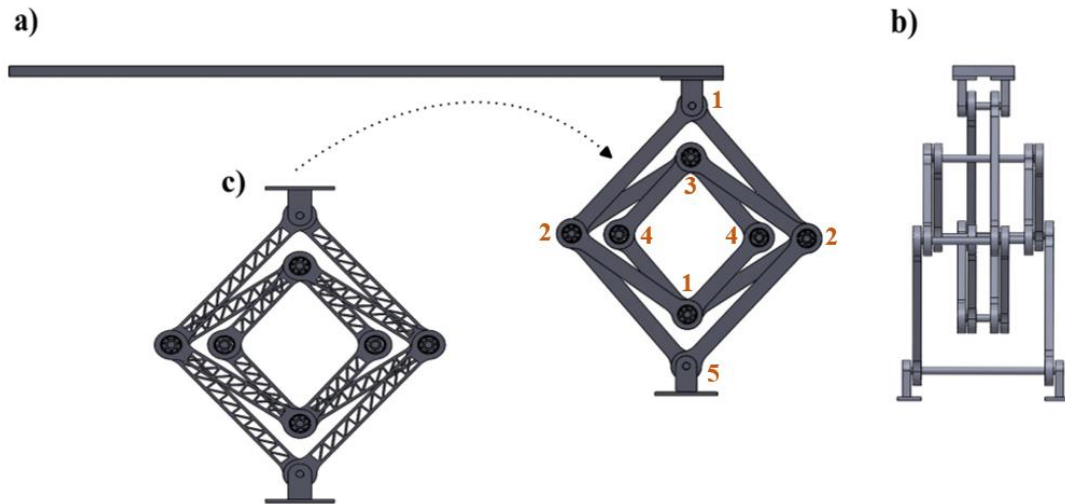


Figure 23: a) A front view CAD assembly model of the nested IA affixed to a cantilever beam. b) A side view CAD assembly model of the nested IA. c) A front view CAD assembly model of the nested truss IA.

The numbers in Figure 23a) correspond to the different pin types used at each joint of the nested IA. The pin types can be cross-referenced with Table 6 in Subsection 4.1.3. to determine the pin lengths at each joint. Note that the pin types and their positions are equivalent amongst corresponding mechanisms.

5. Experimental Analysis of the Inertial Amplifiers

In this Section, an experimental analysis will be conducted on each IA, to assess the dynamic behaviour and the performance of each mechanism, to validate the accuracy of the theoretical models utilised in Section 3, and to identify any possible design flaws and optimization opportunities.

Two sets of experiments will be carried out. The first set of experiments will involve directly mounting each individual IA to an electrodynamic shaker. This will allow the pure mass effects of each IA to be identified. The second set of experiments will assess the impact of the single-stage and single-stage truss IAs, as well as the compound and compound truss IAs, on the dominant single-degree-of-freedom mode of a cantilever beam. In order to evaluate how each IA will influence the dynamic behaviour of a cantilever beam, a clear understanding of

the cantilevers underlying dynamic behaviour is required. To achieve this, a cantilever will be affixed to an electrodynamic shaker, in a manner comparable to that of each distinct IA.

After establishing the baseline dynamic performance of the cantilever beam, each IA will be coupled to it and subject to various experimental tests. These tests will involve altering the initial amplifier angle and the proof mass of each mechanism. As mentioned in Section 3, the initial amplifier angle will be controlled by changing the height of the mechanism, and the proof mass will be controlled by adding different quantities of mass to the system. The proof mass will be added at either the tip of cantilever, or at specific joints of each IA.

This methodology will not only allow the behaviour and the performance of each IA to be determined, but it will also facilitate the identification of any potential issues that may arise during the integration of each IA into a real-life application, like atomic force microscopy or vibration-based energy harvesting.

The Section commences by discussing the experimental configuration of each test, and then continues with an account of the outcomes derived from the experiments.

5.1 Experimental Set-up

In this Subsection, the experimental set-up for each test is described. To achieve a comprehensive understanding of the behaviour and performance of each IA, it is necessary to employ three different experimental set-ups.

The experimental setup used to evaluate the dynamic behaviour of each IA is illustrated in Figure 24a). It is important to note that due to the nature of the testing procedure, only one mechanism can be tested at a time. Therefore, after testing one IA, the testing process will need to be repeated for the remaining five IAs. In this experimental set-up, one end of the test IA is fixed to wooden block 1, which integrates a PCB 352 C03 piezoelectric accelerometer and a PCB 208 C03 force transducer. The total weight of wooden block 1, the accelerometer, and the transducer is 47g. The other end of the IA is attached to wooden block 2, which comprises a PCB 352 C03 piezoelectric accelerometer. The combined mass of wooden block 2 and the accelerometer is 36g. It should be noted that the accelerometer attached to wooden block 2 serves the purpose of monitoring the stationary position of the attached end of the IA. Both ends of the IA are secured to their respective wooden blocks using four M2.5 TX pan machine screws and four M2.5 hexagonal nuts. To affix the IA to the testing apparatus, the

transducer attached to wooden block 1 is screwed into a Data Physics GW-V4 electrodynamic shaker, while wooden block 2 is firmly clamped to a metal ramp to establish a grounded fixture. A photograph of the tested compound IA is shown in Figure 24b).

In Figure 25a) the experimental set-up used to assess the dynamic behaviour of the cantilever beam is illustrated. In this configuration, a PCB 208 C03 force transducer is adhered 17.5 mm from one end of the cantilever. A 2mm diameter ABS plastic stinger connects to the force transducer. On the face of the cantilever opposite to the transducer, a PCB 352 C03 piezoelectric accelerometer is secured. It should be noted that the accelerometer is positioned so that it is at a slight misalignment with the force transducer. To secure the cantilever to the test rig, the free end of the stinger is threaded into a Data Physics GW-V4 electrodynamic shaker, and the opposite end of the cantilever is clamped to form a fixed connection. As mentioned in Section 4, Subsection 4.1.5, 100mm of the cantilevers length is clamped, allowing the effect length of the cantilever to measure 300mm. Figure 25b) depicts a photograph of the cantilever beam under test.

In order to determine the individual impact of each IA on the dynamic behaviour of the cantilever beam, it is necessary to couple each IA separately to the beam. The test arrangement used in these experiments is illustrated in Figure 26a). The experimental set-up is identical to that used for the experiment of the cantilever beam, except an IA is now coupled to the free end of the system. One end of the IA is attached to the face of the cantilever with the accelerometer and is aligned centrally with the transducer located on the opposite face of the beam. The other end of the IA is attached to a wooden block that integrates a PCB 352 C03 piezoelectric accelerometer, with a combined mass of 36g. Each end of the IA is secured using four M2.5 TX pan machine screws and four M2.5 hexagonal nuts. Note that the end of the IA that is not attached to the cantilever must be grounded, and therefore clamps are used to secure the wooden block in place.

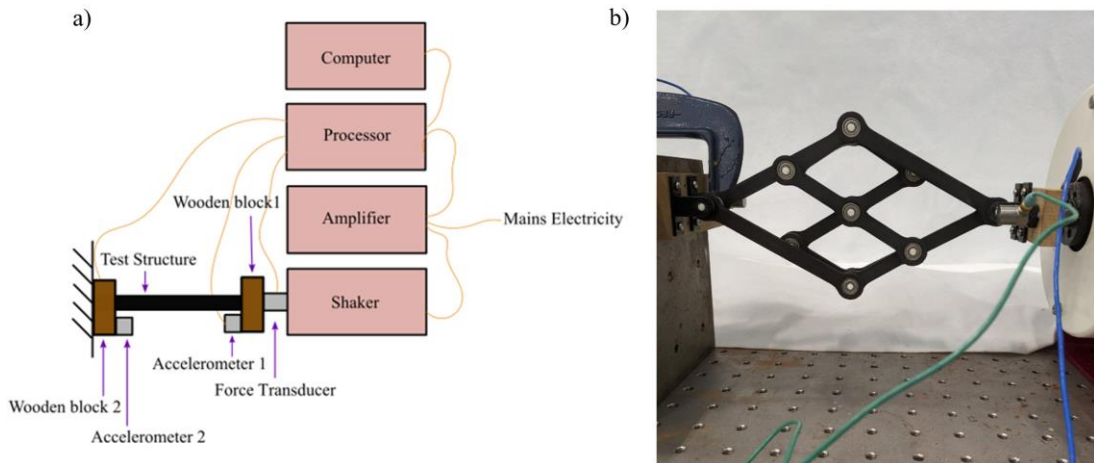


Figure 24: a) Schematic diagram of the experimental set-up to test each distinct IA. b) Photograph of the experiment for the compound IA.

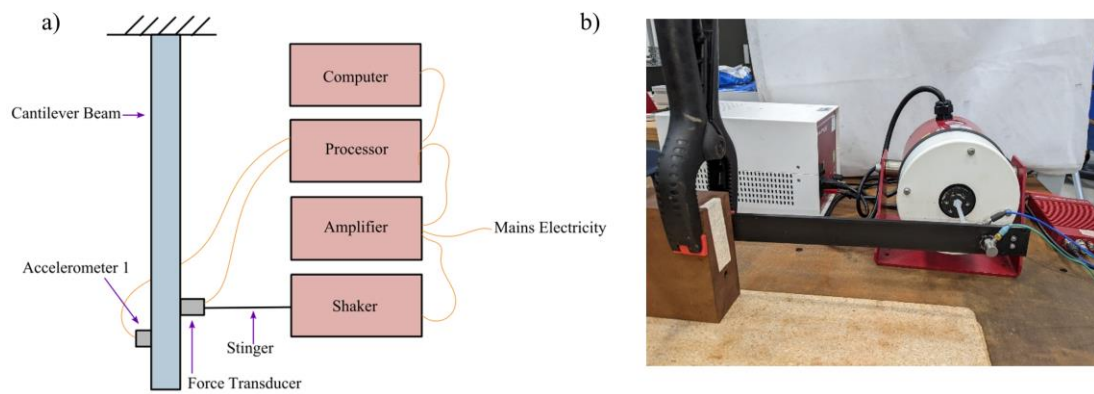


Figure 25: a) Schematic diagram of the experimental set-up for the cantilever beam. b) Photograph of the experimental set-up for the cantilever beam.

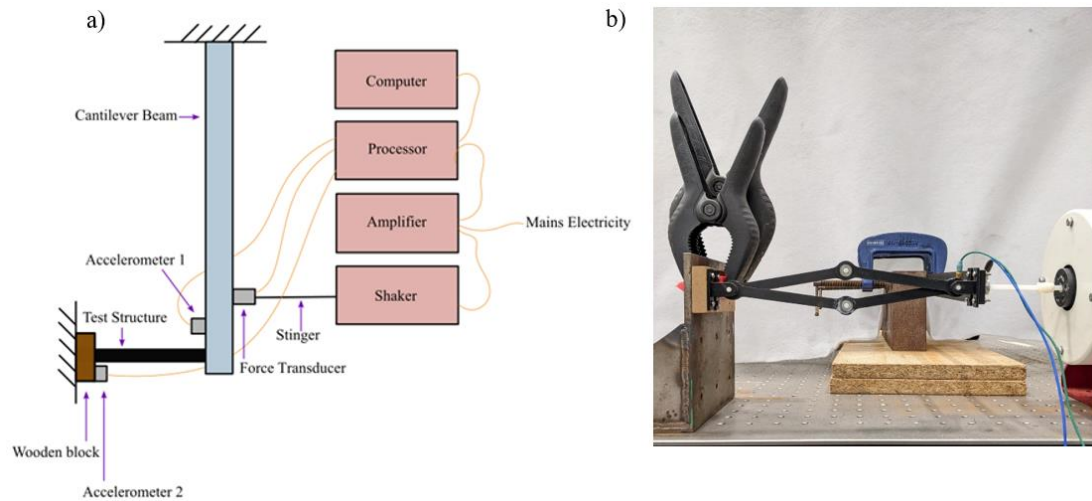


Figure 26: a) Schematic diagram of the experimental setup for each IA coupled to a cantilever beam. b) Photograph of the single-stage IA coupled to a cantilever beam.

To excite and analyse the performance of each test system, a computer with the Data Physics software installed, a Data Physics ABACUS 901 signal analyser, a Data Physics SignalForce 100W amplifier, a Data Physics GW-V4 electrodynamic shaker, a PCB 208 C03 force transducer, and a PCB 352 C03 piezoelectric accelerometer is utilised. The following list, states the use of each apparatus in this work:

- An amplifier is a necessary component of the experiment as it drives the electrodynamic shaker, by providing it with the necessary power to operate. Additionally, the amplifier boosts the level of the input signal to a suitable range for the ABACUS 901 signal analyser to detect and interpret.
- The shaker generates vibrations. In each experiment, the shaker is controlled to generate random wavelength vibrations with a bandwidth of 100Hz. This input is chosen to simulate real-world ubiquitous vibrations.
- A force transducer is used among all experiments to record the force input into each test system.
- For all experiments which involve a cantilever beam, the shaker connects to a lightweight stinger. The stinger allows a more efficient transfer of vibrational energy to the cantilever, and it also helps to eliminate any losses or attenuation of the vibration signal.
- The motion of each test structure is recorded by a PCB 352 C03 piezoelectric accelerometer. Note that for all experiments which involve an IA, two accelerometers are utilised. One accelerometer is employed to measure the response of the mechanism, and

the other accelerometer is used to ensure that there is no movement at the fixed connection of the system.

- A Data Physics ABACUS 901 signal analyser, which is namely ‘processor’ in Figure 24, Figure 25, and Figure 26, is used to measure and analyse the signals from the force transducer and accelerometer(s).
- It is imperative to have a computer equipped with the Data Physics software in order to operate the Data Physics ABACUS 901 signal analyser, capture data, and perform an analysis of the results.

5.2 Experimental Results

In this Subsection the experimental results will be presented. Subsection 5.2.1 presents the dynamic response of each individual IA, Subsection 5.2.2 shows the dynamic behaviour of the cantilever beam, and Subsection 5.2.3. demonstrates the impact of each IA on the cantilever beam.

5.2.1 Pure Mass Inertial Amplifier Tests

In this subsection, the pure mass effects of each IA are presented. It is imperative to comprehend the pure mass effects of each IA, as they can offer crucial insights into the dynamic behaviour of each system. Moreover, understanding these effects can facilitate the optimization of each IA, and foster the development of more accurate theoretical models.

5.2.1.1 Single-Stage Inertial Amplifier

The single-stage IA, depicted in Figure 27, has a mass of 39g. In order to evaluate the dynamic behaviour of the single-stage IA, an electrodynamic shaker test is performed, utilizing the experimental set-up illustrated in Figure 24a), Subsection 5.1. A series of tests are conducted on the single-stage IA, entailing the adjustment of the initial amplifier angle of the mechanism. The selection of the initial amplifier angle as a variable parameter is rooted in the analytical analysis presented in Section 3.1, which suggests that this particular parameter significantly influences the overall behaviour of the mechanism. The initial amplifier angle is varied from 5 to 30 degrees, in increments of five degrees. The response of the mechanism can be seen in Figure 28a) and the corresponding coherence plot can be seen in Figure 28b).

In order to modify the initial amplifier angle of the mechanism, adjustments must be made to the distance between each fixture of the system, including the ground and the shaker. To achieve this, six different pipe lengths are cut, whereby the lengths correspond to the values

of h_1 specified in Table 1, Section 3.1, with an additional 34mm added to each value. The extra 34mm length is to account for the distance between the bottom of each bracket and the centre of the corresponding pin. The pipe is then placed between each fixture to facilitate the correct initial amplifier angle, as depicted by Figure 27.

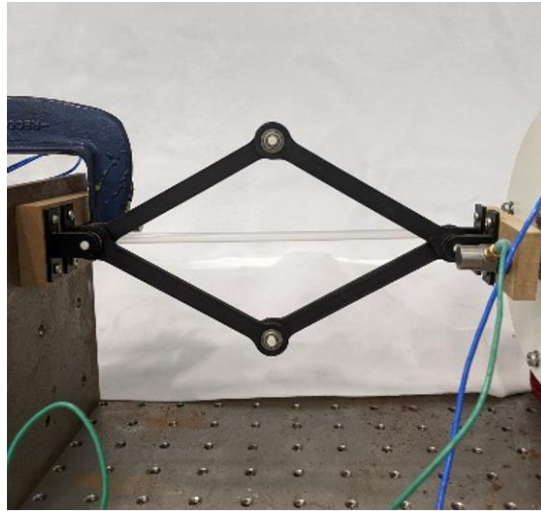


Figure 27: A photograph of the single-stage IA with an initial amplifier angle of 20 degrees.

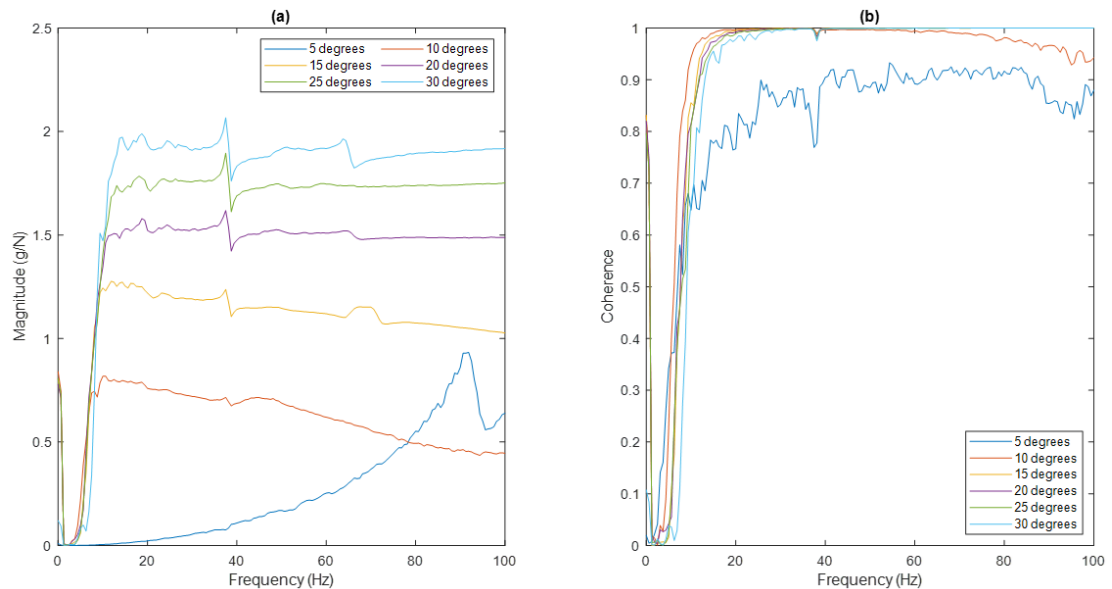


Figure 28a) A frequency response plot of the single-stage IA. b) A coherence plot of the single-stage IA.

Figure 28a) displays the frequency response plot for the single-stage IA at various initial amplifier angles, including 5, 10, 15, 20, 25, and 30 degrees. Notably, when the initial amplifier angle is set to 20, 25, or 30 degrees, the frequency response exhibits a relatively flat line. This suggests that the mechanism can generate a consistent response over a wide range of frequencies, irrespective of any alterations in mass that may occur, as well as any resonance

or damping effects that might cause deviations. When the initial amplifier angle of the mechanism is set to 10 or 15 degrees, the response is also relatively good, although the magnitude of the response begins to decrease for higher frequency values. On the other hand, when the initial amplifier angle is set to 5 degrees, the frequency response is not flat, and there is a resonance peak around 90Hz. This suggests that the structure may exhibit resonance or damping effects for this initial amplifier angle. Furthermore, for the initial amplifier angle cases 10, 15, 20, 25 and 30 degrees, there is a dip at around 40Hz, this is due to the presence of harmonics in the power supply.

Using the linearised equation of motion for the single-stage IA, equation (41) in Section 3.1.3, the magnitude of the response for the single-stage IA with different initial amplifier angles can be calculated. The analytical values are shown in Table 7.

Table 7: A Table to show the analytical magnitude of response values, for the single stage IA with different initial amplifier angles.

Initial amplifier angle \emptyset (degrees)	Magnitude of response (g/N)
5	0.0397
10	0.1576
15	0.3501
20	0.6115
25	0.9336
30	1.3068

The analytical magnitude of response values presented in Table 7, exhibit lower readings compared to the experimental magnitude of response values in Figure 28a). This disparity could suggest two possible scenarios: the mechanism could possess nonlinear characteristics, and or there might be experimental and human error involved in determining the initial amplifier angles, in which the system could be quite sensitive to.

Figure 28b) presents the coherence plot corresponding to Figure 28a). Notably, the coherence is excellent for the single-stage IA with an initial amplifier angle of 10, 15, 20, 25, and 30 degrees, indicating a strong correlation between the input and output signals. However, the coherence is not as high for an initial amplifier angle of 5 degrees.

5.2.1.2 Single-stage Truss Amplifier

Figure 29 displays the single-stage truss IA, which has a mass of 37g. This mechanism shares similarities with the single-stage IA illustrated in Figure 27, but features a design variant which is elaborated upon in Subsection 4.1.1 of this paper. To experimentally evaluate the dynamic behaviour of the single-stage truss IA, the same experimental set-up and procedure is used as for that of the single-stage IA mentioned in Subsection 5.2.1.1. This involves conducting six electrodynamic shaker tests on the IA, for different initial amplifier angles, 5, 10, 15, 20, 25, and 30 degrees. It is worth noting that adjustments to the initial amplifier angle are made based on the mechanism's height, utilizing the lengths and methodology discussed in Subsection 5.2.1.1. The dynamic response of the single-stage truss IA can be seen in Figure 30a) and the corresponding coherence plot can be seen in Figure 30b).

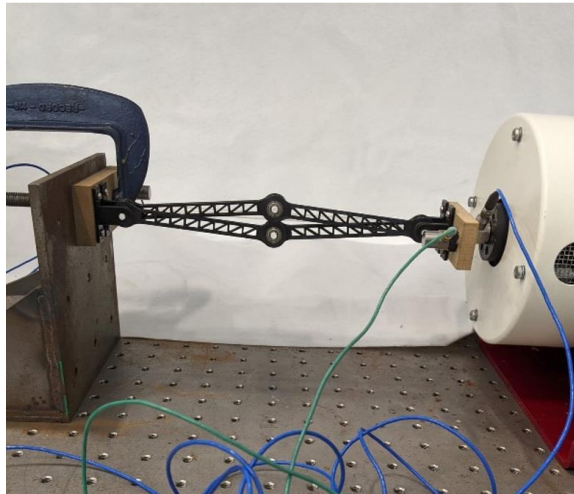


Figure 29: A photograph of the single-stage truss IA with an initial amplifier angle of 5 degrees.

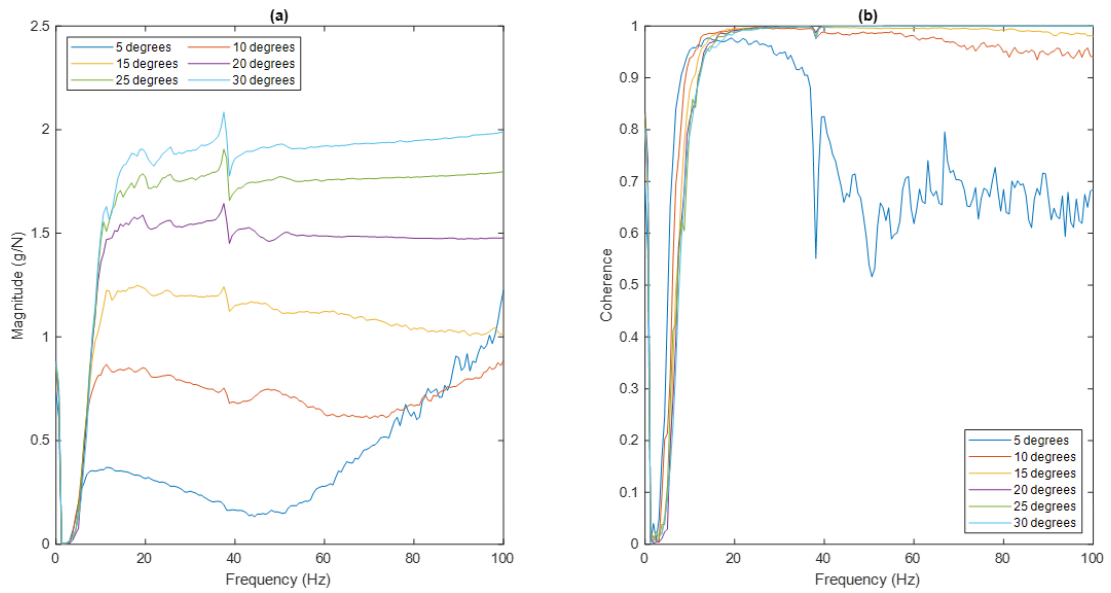


Figure 30: a) A frequency response plot of the single-stage truss IA. b) A coherence plot of the single-stage truss IA.

Figure 30a) depicts the frequency response plot for the single-stage truss IA with different initial amplifier angles, ranging from 5 to 30 degrees. The trend in the response for initial amplifier angles 10, 15, 20, 25 and 30 degrees, is consistent with the response of the single-stage IA, described in Subsection 5.2.1.1., for initial amplifier angles 10, 15, 20, 25 and 30 degrees. This not only suggests that the mechanism can generate a consistent response over a wide range of frequencies, irrespective of any alterations in mass that may occur, or any resonance or damping effects that might cause deviations, but also that both mechanisms have a similar behaviour. However, when the initial amplifier angle of the single-stage truss IA is 5 degrees, the frequency response is not flat, and there is a dip in the response around 50Hz, followed by a gradual rise. This suggests that the structure may exhibit resonance or damping effects at an initial amplifier angle of 5 degrees.

The frequency response for the single-stage truss IA differs at 5 degrees from the single-stage IA, shown in Figure 28a). This could be due to noise, interference, and or structural nonlinearities that may exist between the different mechanisms. Notably, the coherence plot for the single-stage truss IA with an initial amplifier angle of 5 degrees, shown in Figure 30b), indicates a good coherence up to 30 Hz, beyond which it deteriorates. In contrast, the coherence plot for the single-stage IA, displayed in Figure 28b), initially demonstrates poor coherence and gradually improves over time. The aforementioned factors could be the reason for this trend in coherence, and thus frequency response pattern.

Using the linearised equation of motion for the single-stage truss IA, equation (41) in Section 3.1.3, the magnitude of the response for the single-stage truss IA with different initial amplifier angles can be calculated. Note that the linearised equation of motion for the single-stage IA and single-stage truss IA is equivalent. The analytical values are shown in Table 8.

Table 8: A Table to show the analytical magnitude of response values, for the single stage truss IA with different initial amplifier angles.

Initial amplifier angle \emptyset (degrees)	Magnitude of response (g/N)
5	0.0418
10	0.1661
15	0.3691
20	0.6445
25	0.9841
30	1.3775

In a manner akin to the single-stage IA, the analytical response values depicted in Table 8 for the single-stage truss IA also demonstrate reduced readings when compared to the experimental response values illustrated in Figure 30a). Again, this discrepancy could suggest two possible scenarios: first, the mechanism could possess nonlinear characteristics, and second, there could be a presence of experimental and human error in the determination of the initial amplifier angles, a factor that the system might be highly sensitive to.

5.2.1.3 Compound Inertial Amplifier

The compound IA, shown in Figure 24b) of Subsection 5.1, has a mass of 77g. In order to evaluate the dynamic behaviour of the compound IA, a series of electrodynamic shaker tests are performed on the mechanism. These tests involve altering the initial amplifier angle of the primary mechanism of the system. Note that a change in the initial amplifier angle of the primary mechanism will result in a change in the initial amplifier of the secondary mechanism. The selection of the initial amplifier angle as a variable parameter is rooted in the analytical analysis presented in Section 3.2, which suggests that this particular parameter significantly influences the overall behaviour of the mechanism. The initial amplifier angle of the primary mechanism is varied from 10 to 30 degrees, in increments of five degrees. The response of the

compound IA can be seen in Figure 31a) and the corresponding coherence plot can be seen in Figure 31b).

To allow the initial amplifier angle of the primary mechanism to be accurately altered, the same procedure is followed as for that of the single-stage and single-stage truss IAs, mentioned in Subsection 5.2.1.1 and 5.2.1.2, respectively. It is important to highlight that the different pipe lengths used to achieve the desired initial amplifier angles remain consistent across all IA mechanisms. This consistency is ensured due to the identical outer dimensions of each mechanism.

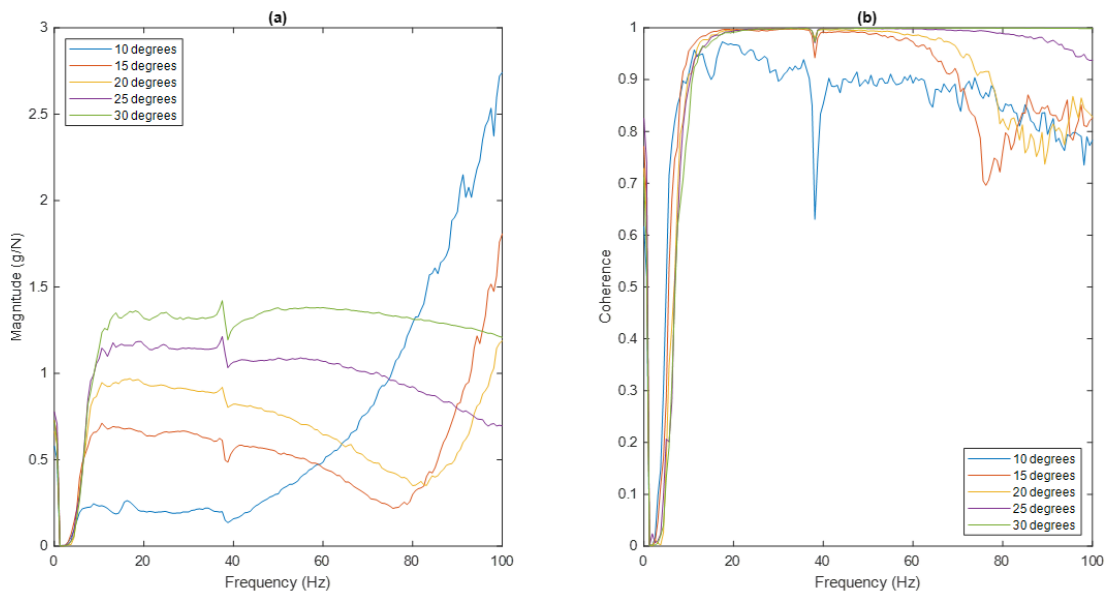


Figure 31: a) A frequency response plot of the compound IA. b) A coherence plot of the compound IA.

Figure 31a) displays the frequency response plot for the compound IA, showcasing different initial amplifier angles for the primary mechanism. The range of initial amplifier angles spans from 10 to 30 degrees. When the initial amplifier angle of the primary mechanism is set to 15, 20, 25, and 30 degrees, the frequency response exhibits a fairly constant magnitude. However, it is important to note that beyond approximately 50Hz, the magnitude of each response begins to gradually decrease, indicating that the compound IA may exhibit an unstable response that is sensitive to changes in mass, as well as any resonance and damping effects within the structure. When the initial amplifier angle of the primary mechanism is set to 10 degrees, the frequency response of the compound IA maintains a relatively stable magnitude up to 40Hz. Beyond this point, there is a steep increase in magnitude with increasing frequency, suggesting that the structure may be approaching its resonance frequency.

It is worth noting that the relationships depicted in Figure 31a) bear resemblance to those shown for that of the single-stage and single-stage truss IAs, presented in Figure 28a) Subsection 5.2.1.1 and Figure 30a) Subsection 5.2.1.2, respectively. However, the magnitude of the response for each initial amplifier angle of the compound IA, is lower by approximately 0.5g/N. Additionally, the frequency range with a flat response is smaller for the compound IA compared to the aforementioned single-stage and single-stage truss IAs.

By utilizing the linearized equation of motion for the compound IA, specifically equation (63) in Section 3.2.3, it becomes possible to calculate the magnitude of the response for the system under various initial amplifier angles. The corresponding analytical values are presented in Table 9.

Table 9: A Table to show the analytical magnitude of response values, for the compound IA with different initial amplifier angles.

Primary initial amplifier angle ϕ_1 (degrees)	Secondary initial amplifier angle ϕ_2 (degrees)	Magnitude of response (g/N)
5	5.56	0.1517
10	11.12	0.5149
15	16.71	0.9229
20	22.33	1.2725
25	28.01	1.5347
30	33.75	1.7141

In accordance with the previously discussed IAs in Section 5.2.1.1 and 5.2.1.2, the analytical calculations in Table 9 demonstrate lower readings in contrast with the experimental values presented in Figure 31a). The presence of the observed discrepancy, as indicated in Section 5.2.1.1, remains a viable explanation. It is also important to note that the primary mechanism of the compound IA cannot physically attain an initial amplifier angle of 5 degrees. Consequently, the experimental results for such an angle are absent. Nonetheless, the analytical results are included for completeness.

The coherence plot, depicted in Figure 31b), demonstrates that the compound IA maintains a strong coherence for initial amplifier angles of 15, 20, 25, or 30 degrees, up to a frequency of 60Hz. Beyond this frequency, the correlation between the input and output signals of the

system tends to decrease. While the coherence is not as high when the initial amplifier angle of the mechanism is 10 degrees, it is still considered acceptable. Note that a dip in coherence is observed across all test conditions at 40Hz, which can be attributed to the presence of harmonics in the power supply.

5.2.1.4 Compound Truss Inertial Amplifier

The compound truss IA, which has a mass of 74g, is identical to the compound IA illustrated in Figure 24b) Subsection 5.1, with the exception of a design variant expounded upon in Subsection 4.1.1. This design variant can also be observed in Figure 29 Subsection 5.2.1.2. for the single-stage truss IA. To evaluate the dynamic behaviour of the compound truss IA, five electrodynamic shaker tests are performed on the system. These tests involve altering the initial amplifier angle of the primary mechanism. The experimental set-up utilised can be seen in Figure 24a) Subsection 5.1, and the outcomes from these experiments can be seen in Figure 32.

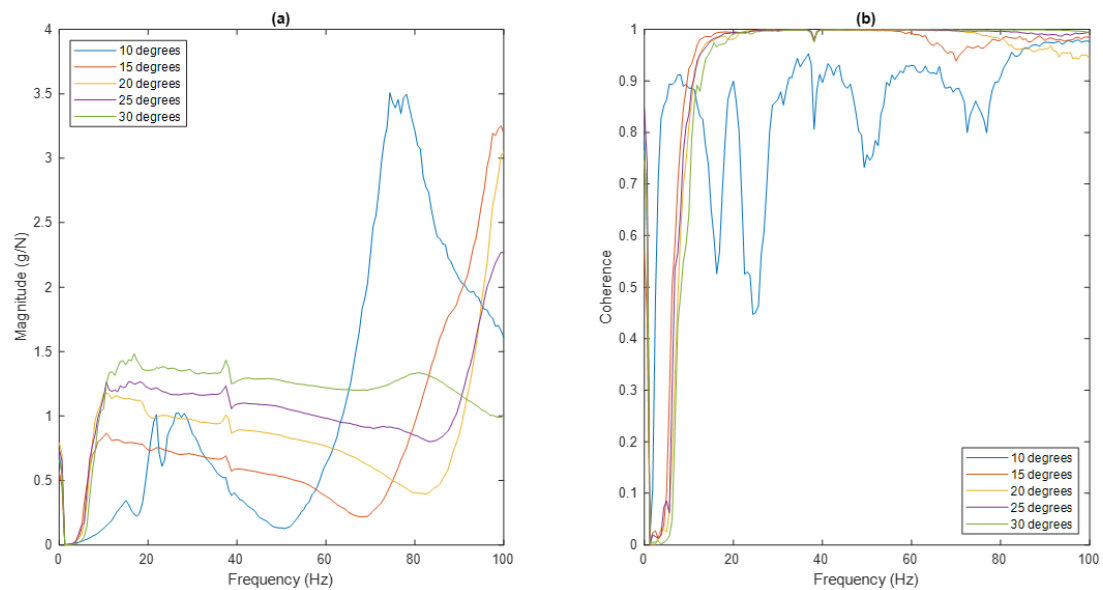


Figure 32: a) A frequency response plot of the compound truss IA. b) A coherence plot of the compound truss IA.

Figure 32a) presents the frequency response plot for the compound truss IA, illustrating the response for different initial amplifier angles of the primary mechanism, ranging from 10 to 30 degrees. When considering an initial amplifier angle of 15, 20, 25, and 30 degrees, the frequency response of the compound truss IA initially demonstrates a relatively constant magnitude. However, as the frequency increases, the magnitude of each response gradually decreases. Notably, for the initial amplifier angle cases 15, 20, and 25 degrees, a significant

upsurge in magnitude then takes place, as the frequency approaches approximately 68Hz, 81Hz, and 84Hz, respectively. This observation implies that the structure may be approaching resonance. In contrast, for an initial amplifier angle of 10 degrees, the frequency response of the compound truss IA is not flat, and instead exhibits a messy response pattern. This suggests that the compound truss IA may demonstrate resonance or damping effects with an initial amplifier angle of 10 degrees. Note that a clear resonance peak is observed at around 78Hz for this case.

Using the linearised equation of motion for the compound truss IA, equation (63) in Section 3.2.3, the magnitude of the response for the system with different initial amplifier angles can be calculated. The analytical values are shown in Table 10. Note that the linearised equation of motions for the compound and compound truss IAs are equivalent.

Table 10: A Table to show the analytical magnitude of response values, for the compound truss IA with different initial amplifier angles.

Primary initial amplifier angle ϕ_1 (degrees)	Secondary initial amplifier angle ϕ_2 (degrees)	Magnitude of response (g/N)
5	5.56	0.1578
10	11.12	0.5358
15	16.71	0.9603
20	22.33	1.3241
25	28.01	1.5969
30	33.75	1.7836

Upon analysing the experimental magnitude of response values depicted in Figure 32a), and comparing them to the calculated magnitude of response values presented in Table 10, a noticeable discrepancy emerges. The potential factors contributing to this discrepancy are elucidated in Sections 5.2.1.1, 5.2.1.2, and 5.2.1.3. It is important to acknowledge that, similar to the compound IA, the analytical results for the compound truss IA with an initial amplifier angle of 5 degrees have been included for the purpose of completeness, despite the absence of experimental data for comparison.

Figure 32b) presents the coherence plot corresponding to Figure 32a). The coherence is excellent when the primary mechanism of the compound truss IA has an initial amplifier angle

of 15, 20, 25, and 30 degrees, indicating a strong correlation between the input and output signals. However, for an initial amplifier angle of 10 degrees the coherence is not ideal, since the value drops below 0.5. As the analytical graphs in Figure 7a) and Figure 7b) of Subsection 3.2.2. show that nonlinearities are highly significant at low angles, poor coherence is to be expected due to the fact that FRFs become quite unreliable with nonlinearities.

5.2.1.5 Nested Inertial Amplifier

The nested IA, depicted in Figure 33, has a mass of 89g. In order to evaluate the dynamic behaviour of the nested IA, several electrodynamic shaker tests are conducted on the mechanism, utilizing the experimental set-up illustrated in Figure 24a), Subsection 5.1. Each test involves adjusting the initial amplifier angle of the primary mechanism, as the analytical analysis in Subsection 3.3 suggests that this parameter significantly impacts the overall behaviour of the nested IA. The initial amplifier angle is controlled between 25 to 30 degrees, in increments of five degrees. To obtain the appropriate initial amplifier angle, the method outlined in Subsection 5.2.1.1 is employed. Figure 34 shows the results of the experiments.

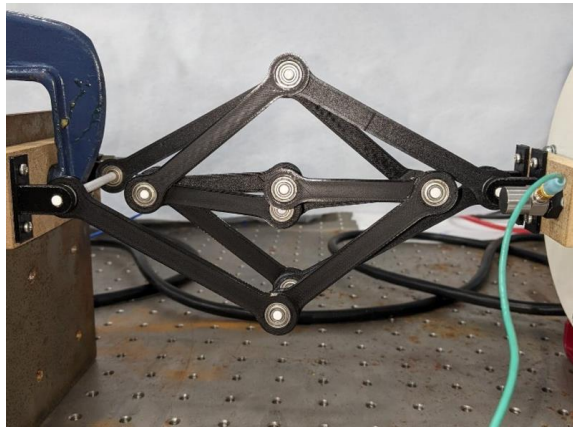


Figure 33: A photograph of the nested IA with an initial amplifier angle of 25 degrees.

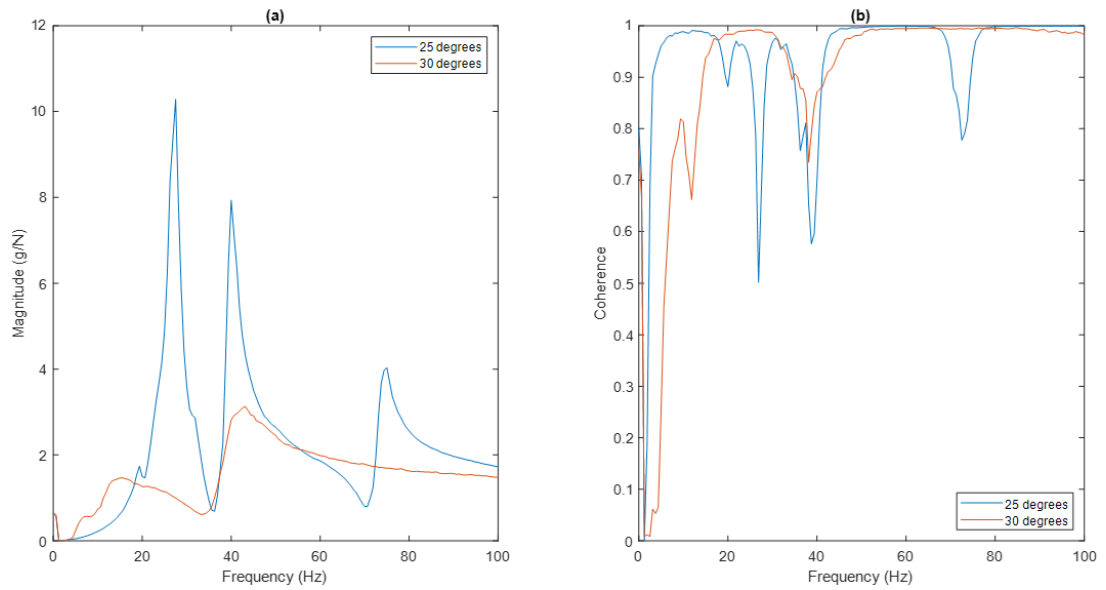


Figure 34: a) A frequency response plot of the nested IA. b) A coherence plot of the nested IA.

The frequency response plot for the nested IA is presented in Figure 34a) which depicts the response of the mechanism for a primary initial amplifier angle of 25 and 30 degrees. For both test cases, an irregular response pattern is observed, which indicates a potential instability of the system. Notably, resonance peaks are detected at frequencies of approximately 27Hz, 41Hz, and 76Hz when the initial amplifier angle is 25 degrees, and at approximately 14Hz and 42Hz when the initial amplifier angle is 30 degrees. These peaks are likely to be caused by resonance or damping effects within the structure of the mechanism, and they indicate that the nested IA is sensitive to changes in mass. The nested IA contains 24 joints, which could lead to significant damping effects, primarily through friction. Such effects may impact the resonance within the structure. To comprehend the resonance and damping effects, further investigations could be conducted, including experiments varying the driving frequency of the input signal, and employing finite element analysis (FEA) to explore the IAs mode shapes. Comparative analysis of the data in Figure 34a) and the results from the proposed additional tests could help to confirm any resonance and damping within the IA.

Using the linearised equation of motion for the nested IA, equation (84) in Section 3.3.3, the magnitude of the response for the nested IA with different initial amplifier angles can be calculated. The analytical values are shown in Table 11.

Table 11: A Table to show the analytical magnitude of response values, for the nested IA with different initial amplifier angles.

Primary initial amplifier angle ϕ_1 (degrees)	Magnitude of response (g/N)
5	1.7333
10	1.5896
15	1.3557
20	1.0374
25	0.6450
30	0.1911

Upon analysing the experimental magnitude of response values depicted in Figure 34a), and comparing them to the calculated magnitude of response values presented in Table 11, no noticeable trend can be seen. The disparity between the experimental and analytical results may be attributed to the use of a linear equation for calculating the response magnitude, as the experimental system is non-linear. Note that despite the absence of experimental data for initial amplifier angles 5, 10, 15 and 20 degrees, the analytical results have been included for completeness.

Figure 34b) shows the coherence plot which corresponds to the frequency response plot in Figure 34a). It is evident that the coherence is poor for both the tested initial amplifier angles. This could be due to non-linearities present within the mechanism. Since the mechanism exhibits an unsatisfactory response, no further findings pertaining to this IA will be presented.

5.2.1.6 Nested Truss Inertial Amplifier

The nested truss IA, which has a mass of 84g, is identical to the nested IA illustrated in Figure 33 Subsection 5.2.1.5, with the exception of a design variant expounded upon in subsection 4.1.1. This design variant can also be observed in Figure 29 Subsection 5.2.1.2. for the single-stage truss IA. To evaluate the dynamic behaviour of the nested truss IA, two tests are conducted, each varying the initial amplifier angle of the primary mechanism. The experimental set-up utilised for these tests can be seen in Figure 24a) Subsection 5.1, and the outcomes from these experiments can be seen in Figure 35.

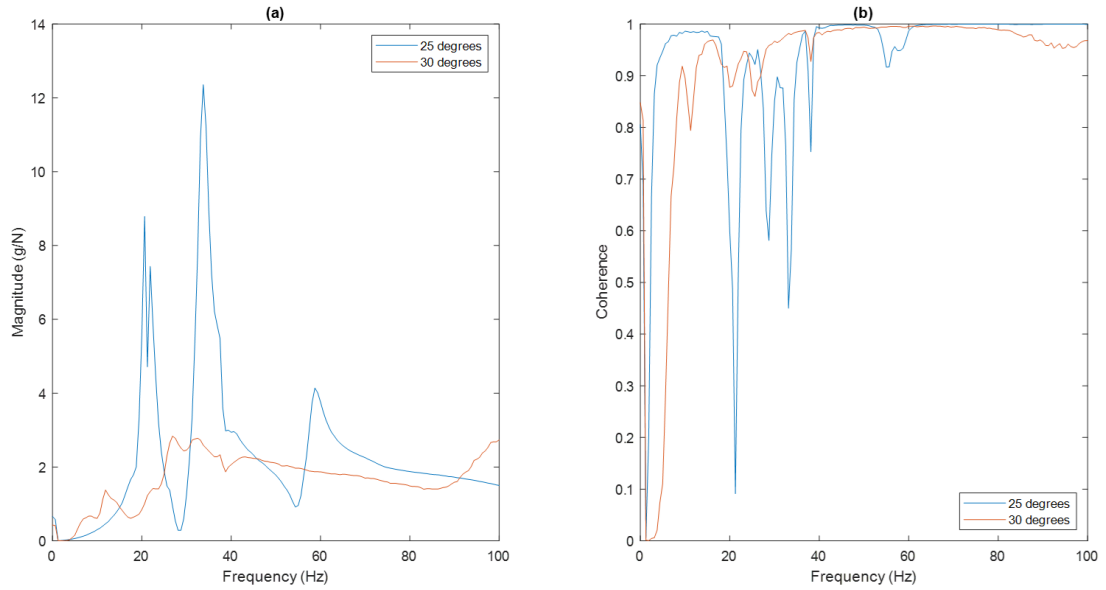


Figure 35: a) A frequency response plot of the nested truss IA. b) A coherence plot of the nested truss IA

Figure 35a) depicts the frequency response plot for the nested truss IA, illustrating the response for the mechanism at two different primary initial amplifier angles, 25 and 30 degrees. Similar to the nested IA, the response exhibits a non-uniform pattern for both test conditions, possibly due to non-linearities within the structure of the mechanism. When the initial amplifier angle of the primary mechanism for the nested truss IA is 25 degrees, two resonance peaks emerge at approximately 20Hz, 33Hz, and 60Hz. In contrast, no distinct resonance peaks are observable when the initial amplifier angle of the primary mechanism is 30 degrees.

Using the linearised equation of motion for the nested truss IA, equation (84) in Section 3.3.3, the magnitude of the response for the system with different initial amplifier angles can be calculated. The analytical values are shown in Table 12. Note that the linearised equation of motions for the nested and nested truss IAs are equivalent.

Table 12: A Table to show the analytical magnitude of response values, for the nested truss IA with different initial amplifier angles.

Primary initial amplifier angle \emptyset_1 (degrees)	Magnitude of response (g/N)
5	1.8365
10	1.6843
15	1.4364
20	1.0991
25	0.6834
30	0.2025

In a manner akin to the nested IA discussed in Section 5.2.1.5, no discernible trend can be observed between the experimental magnitude of response values depicted in Figure 35a) and the analytical magnitude of response values presented in Table 12. This lack of correlation may be attributed to nonlinearities within the system or potential errors in measuring the initial amplifier angle. Additionally, the poor coherence response in Figure 35b), which corresponds to the frequency response plot in Figure 35a) indicates a weak linear relationship between the input and output signals, which could contribute to disparities between the analytical and experimental data.

It is evident that the coherence is poor when the initial amplifier angle is 25 degrees. Conversely, the coherence is acceptable when the initial amplifier angle is 30 degrees. However, since there is no apparent mass effect for this configuration, no additional outcomes will be presented for the nested truss IA.

5.2.2 Cantilever Beam

To establish the performance of each IA, it is essential to examine the dynamic behaviour of the cantilever beam. This will allow the impact of each IA on the behaviour of the cantilever beam to be assessed. To evaluate the behaviour of the cantilever beam several electrodynamic shaker tests are conducted. These tests aim to not only determine the baseline performance of the cantilever, but also the performance of the cantilever under varying quantities of tip mass, specifically 12g, 24g, 36g, and 48g. The results of these experiments are illustrated in Figure 37 and Figure 38.

The introduction of proof mass to the tip of the cantilever is expected to modify the dynamic characteristics of the system. Monitoring and analysing these alterations will facilitate a comprehensive evaluation of the cantilever's behaviour. Furthermore, adding proof mass to the tip of the cantilever should stimulate the effects of each IA when coupled to the system. Therefore, it is necessary to add proof mass to the cantilever for comparative purposes. Figure 36 shows the experiment of the cantilever beam with 48g of proof mass.

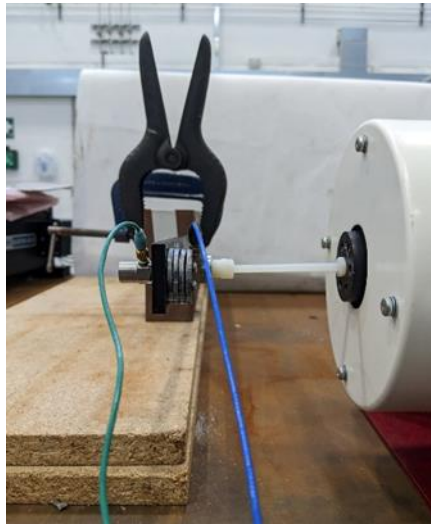


Figure 36: A photograph of the cantilever beam with 48g of tip mass attached.

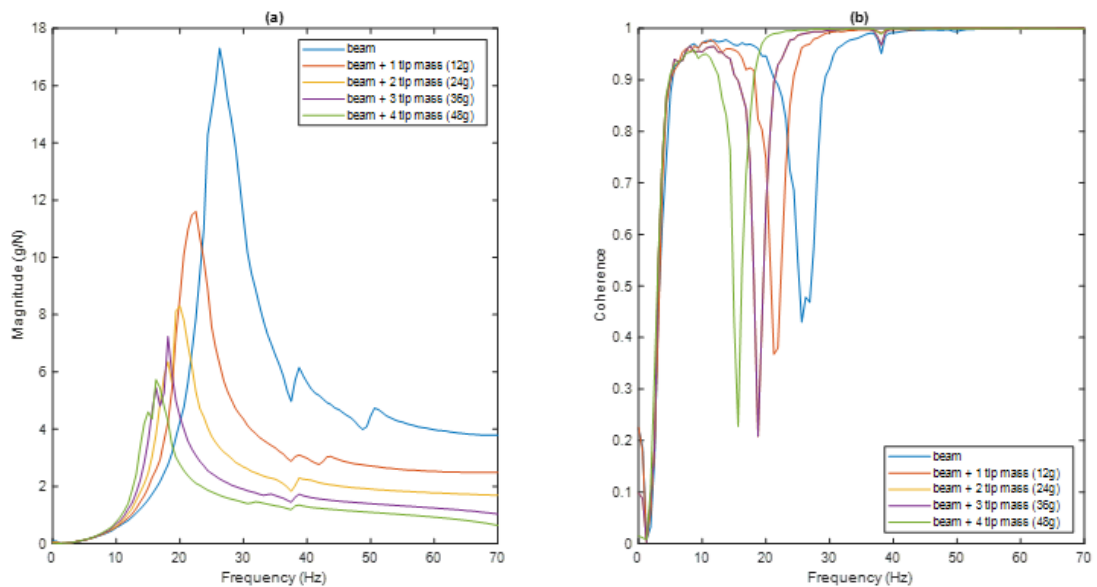


Figure 37: a) A frequency response plot of the cantilever beam. b) A coherence plot of the cantilever beam.

Each plot depicts five conditions, the baseline dynamic behaviour of the cantilever beam and the when 12g, 24g, 36g, and 48g of proof mass have been added to the tip of the free end of the cantilever. Figure 37 a) shows that the natural frequency of the cantilever beam is 26.25

Hz. When 12g, 24g, 36g, and 48g of proof mass is added to the tip of the cantilever, the natural frequency of the cantilever decreases correspondingly to 22.50 Hz, 20.00 Hz, 18.13 Hz, and 16.25 Hz, respectively. The observed inversely proportional relationship between the proof mass and the natural frequency of the cantilever is expected, since the addition of the proof mass results in an increased effective mass of the system. As natural frequency is inversely proportional to the square root of effective mass, the observed trend is explained. Figure 37a) also presents the magnitude of the cantilever's response, which decreases as the proof mass of the system increases.

The coherence for each test can be seen in Figure 37b). In each test, the coherence drops at the natural frequency of the cantilever. This suggests that the linear correlation between the input and output signals diminishes at the natural frequency of the cantilever.

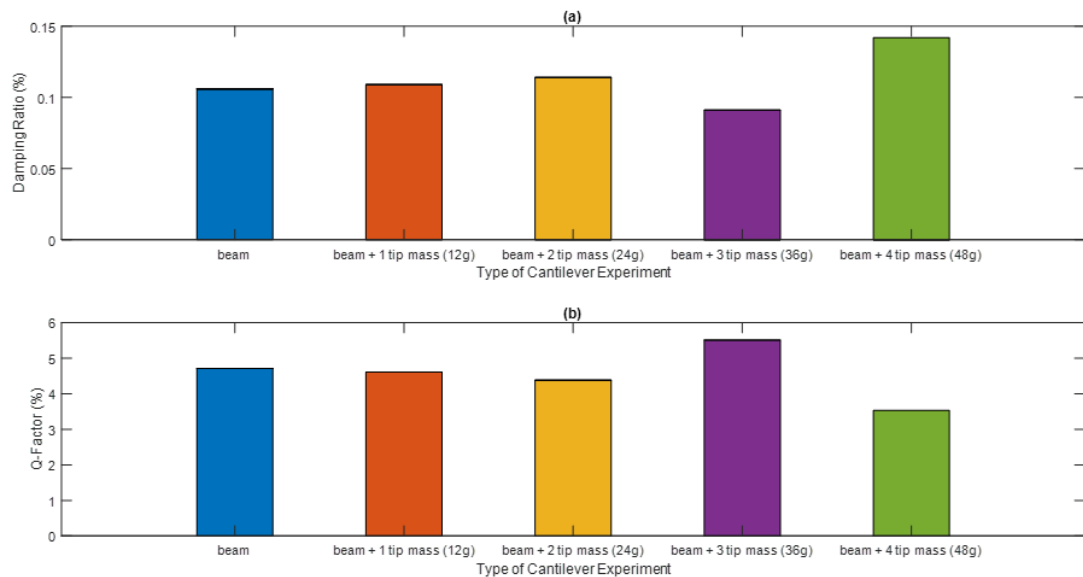


Figure 38: a) A bar chart to show the damping ratio of the cantilever beam for different test conditions. b) A bar chart to show the Q -factor of the cantilever beam for different test conditions.

Each plot depicts five test conditions, which include the standard beam, and the beam with a proof mass of 12g, 24g, 36g, and 48g placed at the tip of the free end of the cantilever. Figure 38a) shows that the damping ratio of the cantilever beam is 0.106%. When 12g, 24g, 36g, and 48g of proof mass is added to the tip of the cantilever, the damping ratio changes correspondingly to 0.109%, 0.114%, 0.091% and 0.142%, respectively. The general trend shows that as the proof mass of the cantilever increases, the damping ratio of the cantilever also increases, except for the case of 36g of proof mass. This is the only case which shows the damping ratio of the cantilever to decrease below its natural value.

Figure 38b) that the Q-factor of the cantilever beam is 4.71%. When 12g, 24g, 36g, and 48g of proof mass is added to the tip of the cantilever, the Q-factor changes correspondingly to 4.61%, 4.38%, 5.51%, and 3.53%, respectively. The general trend shows that as the proof mass of the cantilever increases, the Q-factor of the cantilever decreases, except for the case of 36g of proof mass. For this case, the Q-factor of the cantilever increases, and exceeds the value of the Q-factor for the natural beam.

There is a clear relationship between the Q-factor and the damping ratio of the cantilever beam. As the Q-factor of the cantilever increases the damping ratio of the cantilever decreases. This phenomenon is accounted for by the relationship expounded in equation (3), in Subsection 2.1.3.

5.2.3 Inertial Amplifier Coupled to a Cantilever Beam

In order to assess the performance of each IA, the IAs are individually coupled to a cantilever beam. As the behaviour of the cantilever beam is stated in Subsection 5.2.2, the results outlined in this Section can be compared with those of the cantilever to demonstrate the impact each IA has on its behaviour. Following this process yields valuable insight into how the IAs would perform in a real-life application.

5.2.3.1 Single-Stage Inertial Amplifier Coupled to a Cantilever Beam

Figure 26b) in Subsection 5.1 shows a photograph of the single-stage IA coupled to a cantilever beam. In order to evaluate the dynamic behaviour of the single-stage IA when coupled to a cantilever beam, a series of electrodynamic shaker tests are performed on the system, utilizing the experimental set-up illustrated in Figure 26a), Subsection 5.1. Each test involves altering the initial amplifier angle of the mechanism from 5 to 30 degrees, in increments of five degrees. Note that in order to achieve precise adjustments of the initial amplifier angle of the mechanism, the identical process is implemented as for that of each individual IA, explicitly outlined in Subsection 5.2.1.1 for the single-stage IA. The results of the experiments for the single-stage IA coupled to a cantilever beam are illustrated in Figure 39 and Figure 40.

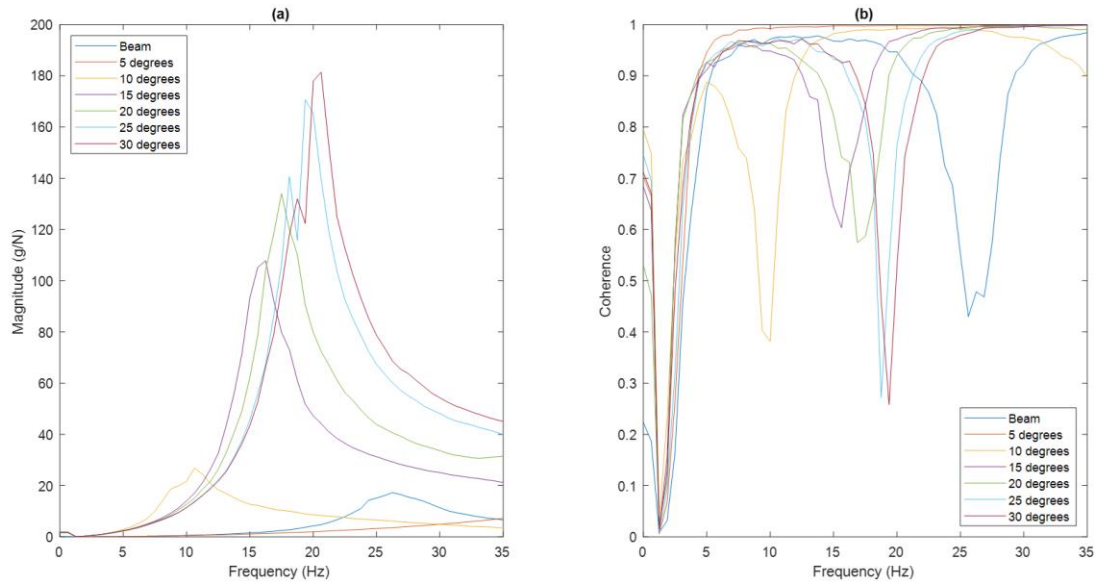


Figure 39: a) A frequency response plot of the single-stage IA coupled to a cantilever beam. b) A coherence plot of the single-stage IA coupled to a cantilever beam.

Figure 39a) illustrates the response of the single-stage IA coupled to a cantilever beam, for six different initial amplifier angles. For an initial amplifier angle of 5 degrees, no distinct resonance is apparent. In contrast, for initial amplifier angles 10, 15, 20, 25, and 30 degrees, the natural frequency of the system is 10.63Hz, 16.25Hz, 17.5Hz, 19.38Hz, and 20.63Hz, respectively. A clear trend is observed whereby an increase in the initial amplifier angle of the mechanism leads to a corresponding rise in the natural frequency of the system. This indicates that there is less effective inertia within the system for larger initial amplifier angles. Furthermore, as the initial amplifier angle increases, the magnitude of the response of the system also increases, with the largest response observed when the initial amplifier angle of the system is 30 degrees. For this case, the magnitude of the response is approximately ten times that of the cantilever beam.

Figure 39b) shows the coherence plot which corresponds to the frequency response plot in Figure 39a). For each test, the coherence drops at the natural frequency of the system. This suggests that the linear correlation between the input and output signals diminishes at each natural frequency, which may be caused by non-linearities within the system.

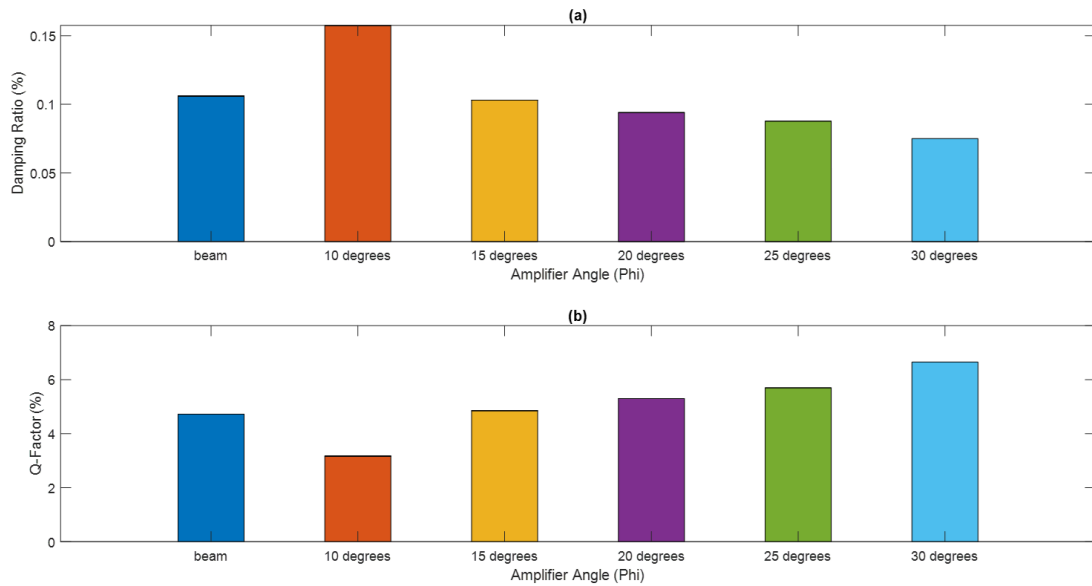


Figure 40: a) A bar chart to show the damping ratio of the single-stage IA coupled to a cantilever beam, for different test conditions. b) A bar chart to show the Q-factor of the single-stage IA coupled to a cantilever beam, for different test conditions. Note that the cantilever beam is displayed for comparison.

Figure 40a) shows that the damping ratio of the system is 0.158%, 0.103%, 0.094%, 0.088% and 0.075%, when the initial amplifier angle of the mechanism is 10, 15, 20, 25 and 30 degrees, respectively. It is worth noting that the damping ratio is not indicated for an initial amplifier angle of 5 degrees as there is no distinct natural frequency shown for this condition. The overall trend indicates that as the initial amplifier angle of the mechanism increases, the damping ratio of the system decreases. Interestingly, for the case of 10 degrees the damping ratio of the system exceeds the damping ratio of the natural beam, which is 0.106%.

Figure 40b) shows the Q-factor of the system to be 3.17%, 4.85%, 5.30%, 5.70% and 6.65%, when the initial amplifier angle of the mechanism is 10, 15, 20, 25 and 30 degrees, respectively. Note that the Q-factor of the system is not given for an initial amplifier angle of 5 degrees because there is no clear natural frequency peak observed. The general trend of the graph shows that as the initial amplifier angle of the mechanism increases, the Q-factor of the system also increases. For the case of an initial amplifier angle of 10 degrees, the Q-factor of the system decreases below the value of the Q-factor for the natural beam.

There is a clear relationship between the Q-factor and the damping ratio of the system. As the Q-factor of the system increases the damping ratio of the system decreases. This phenomenon is accounted for by the relationship expounded in equation (3) of Subsection 2.1.3.

5.2.3.2 Single-Stage Inertial Amplifier Coupled to a Cantilever Beam with Tip Mass

To further assess the influence of the single-stage IA on the behaviour of the cantilever, additional electrodynamic shaker tests are conducted on the system. Each test involves altering the initial amplifier angle of the mechanism between 5 to 30 degrees, in increments of five degrees, but for varying quantities of proof mass added to the tip of the cantilever, specifically 12g, 24g, 36g, and 48g. Note that proof mass is introduced to the cantilever in an effort to stimulate the effects of the IA. The results of these experiments are illustrated in Figure 41 and Figure 42.

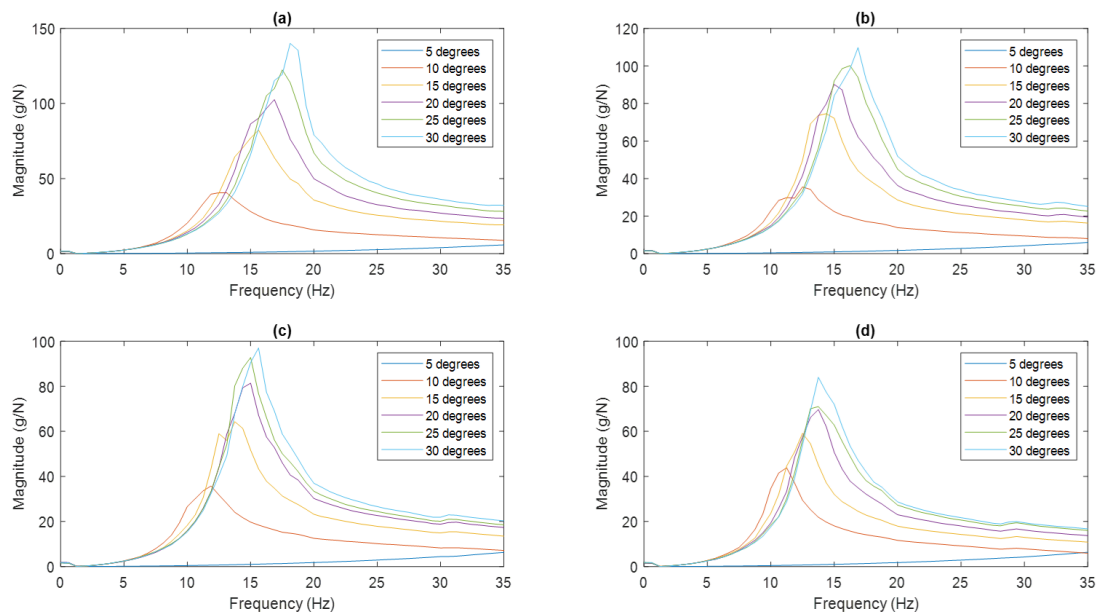


Figure 41: A frequency response plot of the single-stage IA coupled to a cantilever beam with a) 12g, b) 24g, c) 36g, and d) 48g of proof mass added to the tip of the cantilever.

In Figure 41a), b), c) and d), the frequency response of the single-stage IA coupled to a cantilever beam is shown. Twenty-four test conditions are presented, which involve variations of the initial amplifier angle of the mechanism, from 5 to 30 degrees, in increments of five degrees, for various cantilever tip-masses, specifically 12, 24, 36, and 48g. Across all experiments, a distinct trend is shown, whereby an increase in the initial amplifier angle of the system corresponds to a rise in the natural frequency of the system. This trend suggests that the system generates less effective inertia for larger initial amplifier angles. Additionally, for a given initial amplifier angle, the natural frequency of the system decreases as the quantity of cantilever tip mass increases. This relationship is anticipated, as the effective mass of a system is proportional to the square root of the natural frequency of the system, and the inclusion of proof mass augments the effective mass of the system. Furthermore, as the

quantity of cantilever tip mass increases, the magnitude of the response decreases. This is an expected trend, since the motion of the system is dependent on the natural frequency of the system. For a lower natural frequency, the system is less responsive.

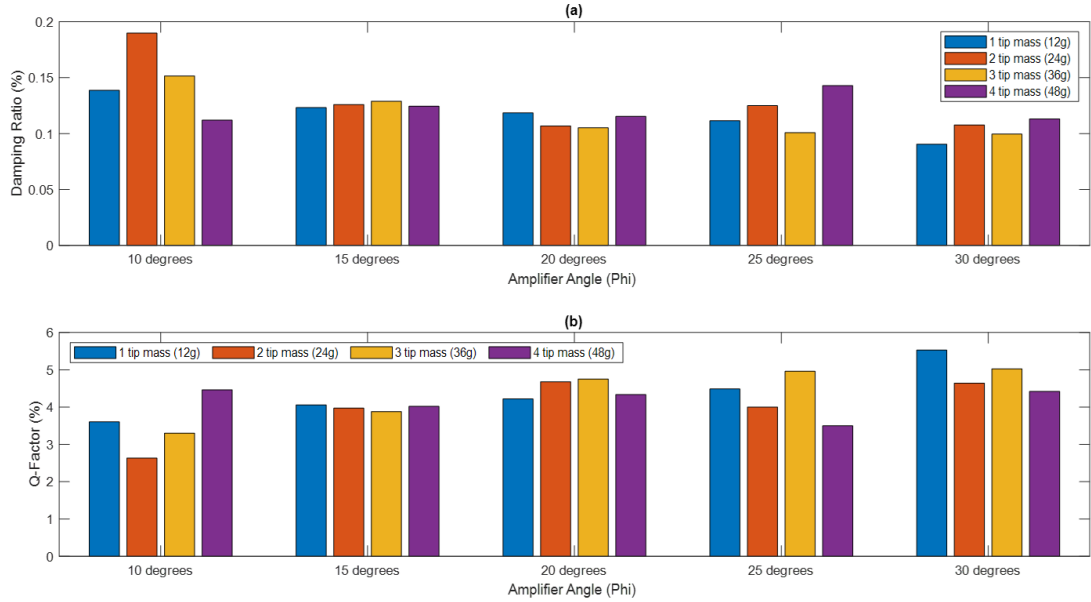


Figure 42: a) A bar chart to show a) the damping ratio, and b) the Q-factor of the single-stage IA coupled to a cantilever beam, when 12g, 24g, 36g and 48g of proof mass has been added to the tip of the cantilever.

Figure 42 a) and b) illustrate the damping ratio and Q-factor characteristics of the single-stage IA when coupled to a cantilever beam, subject to varying initial amplifier angles and tip mass conditions. It is worth noting that the damping ratio of the system exhibits an inverse relationship with the reciprocal of the Q-factor of the system. The damping ratio and Q-factor characteristics are not displayed for an initial amplifier angle of 5 degrees, since there is no clear natural frequency peak in Figure 41a), b), c) and d). When the quantity of proof mass added to the tip of the cantilever is either 12g or 36g, the damping ratio decreases and the Q-factor increases, for increasing initial amplifier angles. For a proof mass of 24g and 48g, there is no distinct observable trend.

5.2.3.3 Single-Stage Inertial Amplifier with Joint Mass Coupled to a Cantilever Beam

To improve the effective inertia of the single-stage IA, a proof mass is added to specific joints of the mechanism, as displayed in Figure 43. For a detailed understanding of the precise joints to which the proof mass is added, refer to Section 3.1.

A sequence of electrodynamic shaker tests are performed on the system, to further assess the influence of the single-stage IA on the behaviour of the cantilever beam. In each test, the initial amplifier angle of the mechanism is adjusted within the range of 5 to 30 degrees, in increments of five degrees, with varying quantities of proof mass, specifically 12g, 24g, 36g, and 48g added to the designated joints of the mechanism. The outcomes of these experiments are presented in Figure 44 and Figure 45.



Figure 43: A photograph of the single-stage IA coupled to a cantilever beam, with 12g of proof mass at each specified joint of the mechanism.

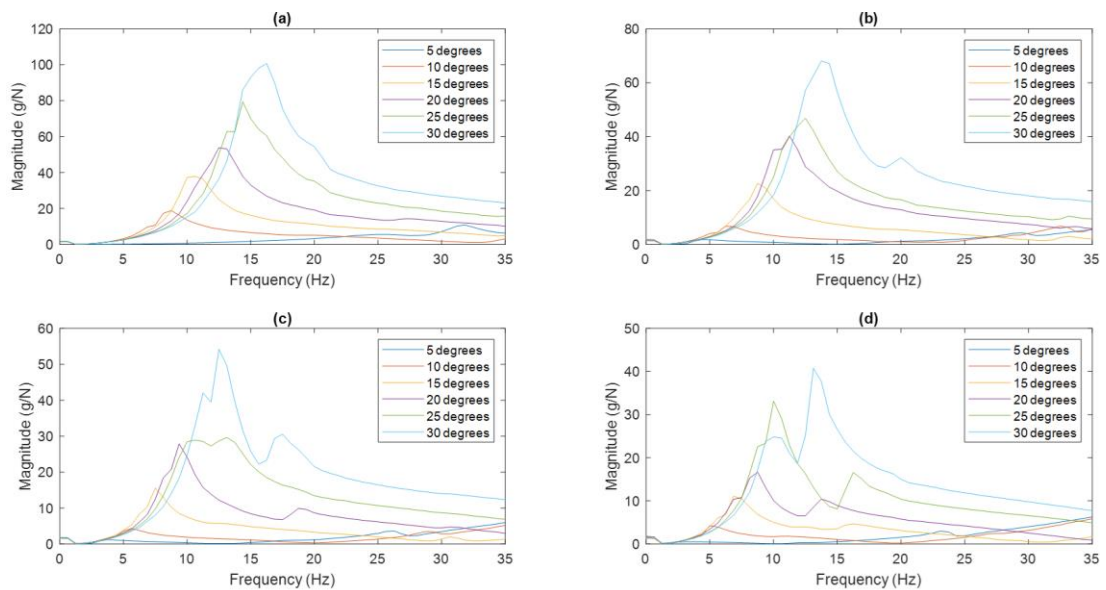


Figure 44: A frequency response plot of the single-stage IA coupled to a cantilever beam with a) 12g, b) 24g, c) 36g, and d) 48g of proof mass added to each specified joint of the mechanism.

In Figure 44a), b), c), and d), the frequency response of the single-stage IA coupled to a cantilever beam is shown; twenty four conditions are presented, which involve variations of the initial amplifier angle of the mechanism, for different quantities of proof mass, specifically

12, 24, 36, and 48g added to each designated joint of the mechanism. Across all experiments, a clear pattern is observed, whereby an increase in the initial amplifier angle of the system corresponds to a rise in the natural frequency of the system. This trend suggests that for larger initial amplifier angles, the system generates less effective inertia. Additionally, for a given initial amplifier angle, the natural frequency of the system decreases as the quantity of joint mass increases. This relationship is expected since the addition of proof mass to the system increases the effective mass of the system. Note that the effective mass of the system is directly proportional to the square root of the natural frequency of the system. Furthermore, as the quantity of joint mass increases, the magnitude of the response decreases, for all initial amplifier angles. This relationship is anticipated since the motion of the system is dependent on the natural frequency of the system. For cases, 36g and 48g of proof mass added to each specific joint of the mechanism, the system becomes slightly unstable, as evidenced by the unsmooth responses in Figure 44c) and d).

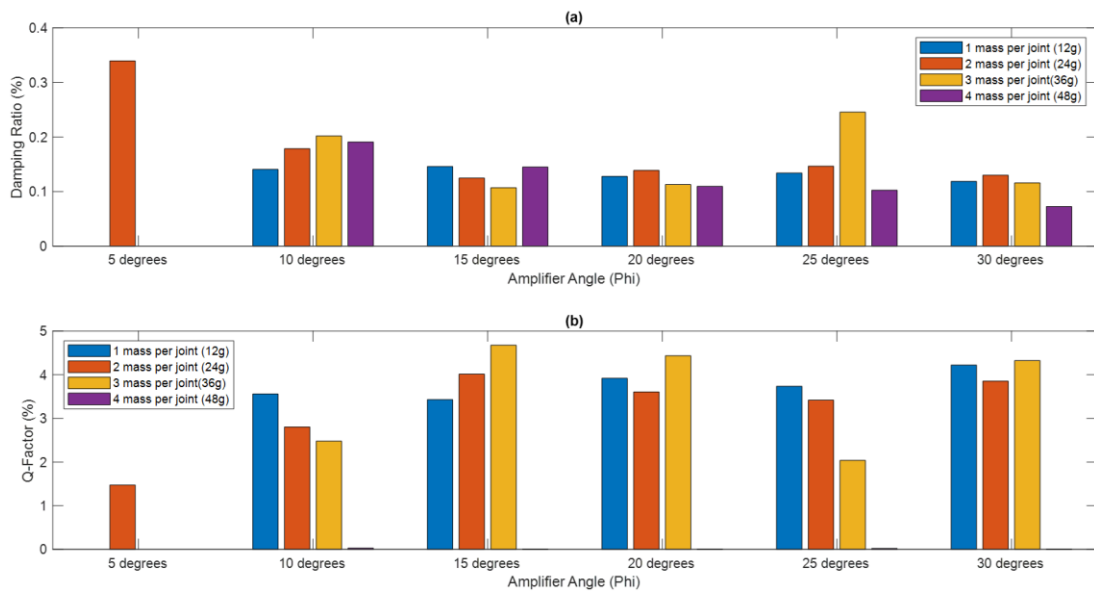


Figure 45: a) A bar chart to show a) the damping ratio, and b) the Q-factor of the single-stage IA coupled to a cantilever beam, when 12g, 24g, 36g and 48g of proof mass has been added to each specified joint of the mechanism.

Figure 45a) and b) illustrate the damping ratio and Q-factor characteristics of the single-stage IA when coupled to a cantilever beam, subject to varying initial amplifier angles and joint mass conditions. The damping ratio and Q-factor characteristics are not displayed for an initial amplifier angle of 5 degrees, for 12g, 36g and 48g of joint mass, since there is no clear natural frequency peak in Figure 44a), c) and d). When the quantity of proof mass added to each specified joint of the single-stage IA is 48g, the damping ratio decreases and the Q-factor increases, for increasing initial amplifier angles. For a proof mass of 12, 24 and 36g, there is no clear trend observed.

5.2.3.4 Single-Stage Truss Inertial Amplifier Coupled to a Cantilever Beam

Figure 46 shows a photograph of the single-stage truss IA coupled to a cantilever beam. In order to evaluate the dynamic behaviour of the single-stage truss IA when it is coupled to a cantilever beam, a series of electrodynamic shaker tests are performed on the system, utilizing the experimental set-up illustrated in Figure 26a), Subsection 5.1. Each test involves altering the initial amplifier angle of the mechanism from 5 to 30 degrees, in increments of five degrees. Figure 47 and Figure 48 display the results of these experiments. Note that to achieve precise adjustments of the initial amplifier angle of the mechanism, the identical process is implemented as for that of each individual IA, explicitly outlined in Subsection 5.2.1.1 for the single-stage IA.

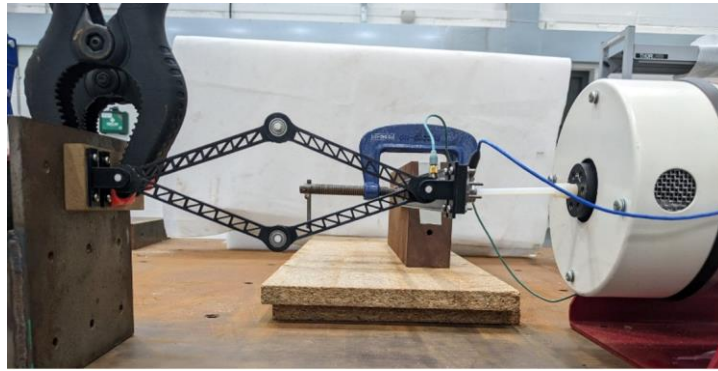


Figure 46: A photograph of the single-stage truss IA with an initial amplifier angle of 20 degrees, coupled to a cantilever beam.

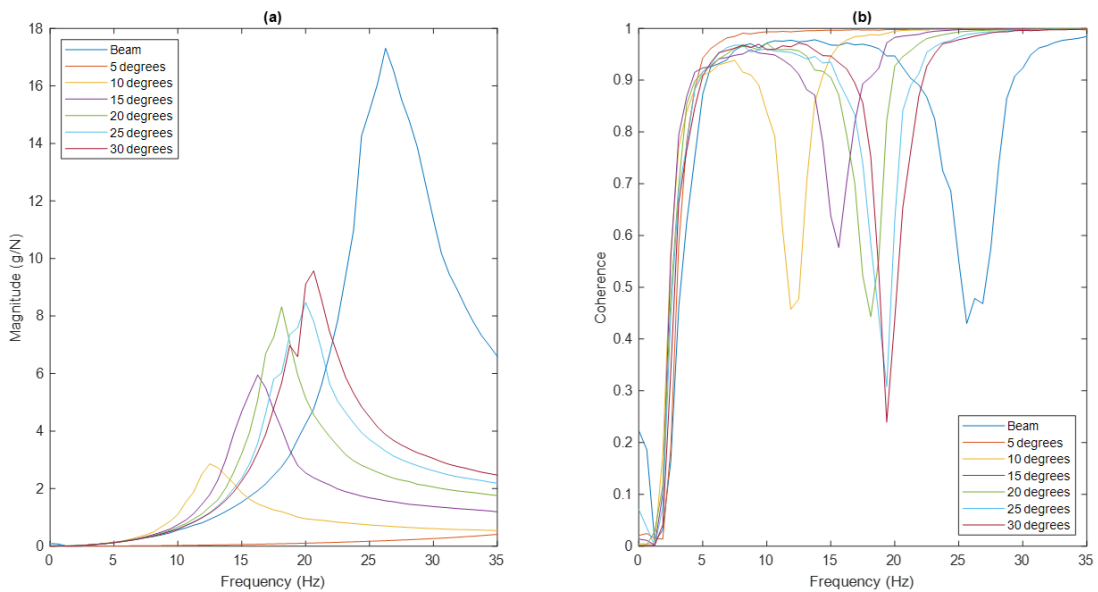


Figure 47: a) A frequency response plot of the single-stage truss IA coupled to a cantilever beam. b) A coherence plot of the single-stage truss IA coupled to a cantilever beam.

Figure 47a) illustrates the frequency response for the single-stage truss IA when coupled to a cantilever beam, for various initial amplifier angles. For an initial amplifier angle of 5 degrees, no distinct natural frequency peak is apparent. In contrast, for initial amplifier angles 10, 15, 20, 25, and 30 degrees, the natural frequency of the system is 12.5Hz, 16.25Hz, 18.13Hz, 20Hz, and 20.63Hz, respectively. A clear trend is observed whereby an increase in the initial amplifier angle of the mechanism leads to a corresponding rise in the natural frequency of the system. This indicates that there is less effective inertia within the system for larger initial amplifier angles. Furthermore, as the initial amplifier angle increases, the magnitude of the response of the system also increases, with the largest response observed when the initial amplifier angle of the system is 30 degrees. The trend observed in this study is consistent with that found in Subsection 5.2.3.1, which examined the single-stage IA coupled to a cantilever beam. In both cases, the natural frequencies occur at approximately the same value. However, unlike the response of the single-stage IA, the magnitude of the response for each initial amplifier angle is lower than that of the cantilever beam.

Figure 47b) illustrates the coherence plot that corresponds to the frequency response plot in Figure 47a). The coherence for each test is not optimal, as it decreases at the natural frequency of the system. This indicates a reduction in the linear correlation between the input and output signals at each natural frequency, which may be attributed to non-linearities within the system.

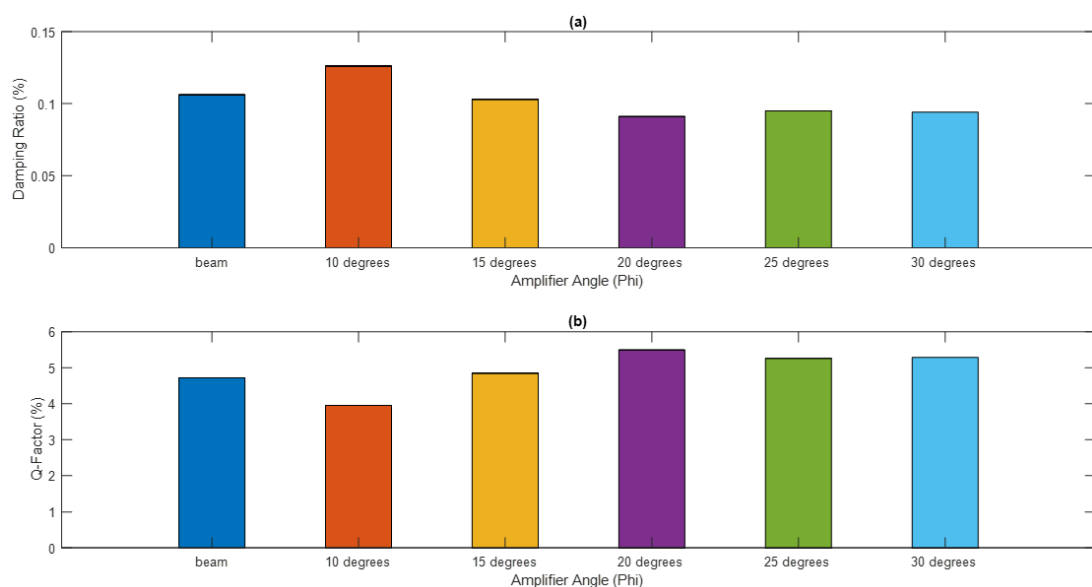


Figure 48: A bar chart to show a) the damping ratio, and b) the Q-factor of the single-stage truss IA coupled to a cantilever beam, for different test conditions.

Figure 48a) shows that the damping ratio of the system is 0.126%, 0.103%, 0.091%, 0.095% and 0.094%, when the initial amplifier angle of the mechanism is 10, 15, 20, 25 and 30 degrees, respectively. It is worth noting that the damping ratio is not shown when the initial amplifier angle of the mechanism is 5 degrees, this is because there is no distinct natural frequency for this condition. The overall trend of the graph indicates that as the initial amplifier angle of the mechanism increases, the damping ratio of the system decreases, except for the cases when the initial amplifier angle is 25 and 30 degrees. For these two cases, the damping ratio slightly increases. Furthermore, the damping ratio of the system surpasses the damping ratio of the cantilever beam, which is 0.106%, only when the initial amplifier of the mechanism is 10 degrees. It is clear that for this particular case, the damping is being amplified to a greater extent than the inertia.

Figure 48b) shows the Q-factor of the system to be 3.96%, 4.85%, 5.49%, 5.26% and 5.29%, when the initial amplifier angle of the mechanism is 10, 15, 20, 25 and 30 degrees, respectively. The Q-factor of the system is not given for an initial amplifier angle of 5 degrees because there is no observable natural frequency peak. The general trend of the graph shows that as the initial amplifier angle of the mechanism increases, the Q-factor of the system also increases, except for when the initial amplifier angle is 25 and 30 degrees. For these two cases, the Q-factor slightly decreases. Note that the relationship for the Q-factor of the system is directly proportional to the reciprocal of the damping ratio of the system.

5.2.3.5 Single-Stage Truss Inertial Amplifier Coupled to a Cantilever Beam with Tip Mass

To further assess the influence of the single-stage truss IA on the behaviour of the cantilever beam, additional electrodynamic shaker tests are conducted on the system. Each test involves altering the initial amplifier angle of the mechanism between 5 to 30 degrees, in increments of five degrees, but for varying quantities of proof mass added to the tip of the cantilever, specifically 12g, 24g, 36g, and 48g. Note that proof mass is introduced to the cantilever, as shown in Figure 36 Subsection 5.2.2, in an effort to stimulate the effects of the IA. The results of these experiments are illustrated in Figure 49 and Figure 50.

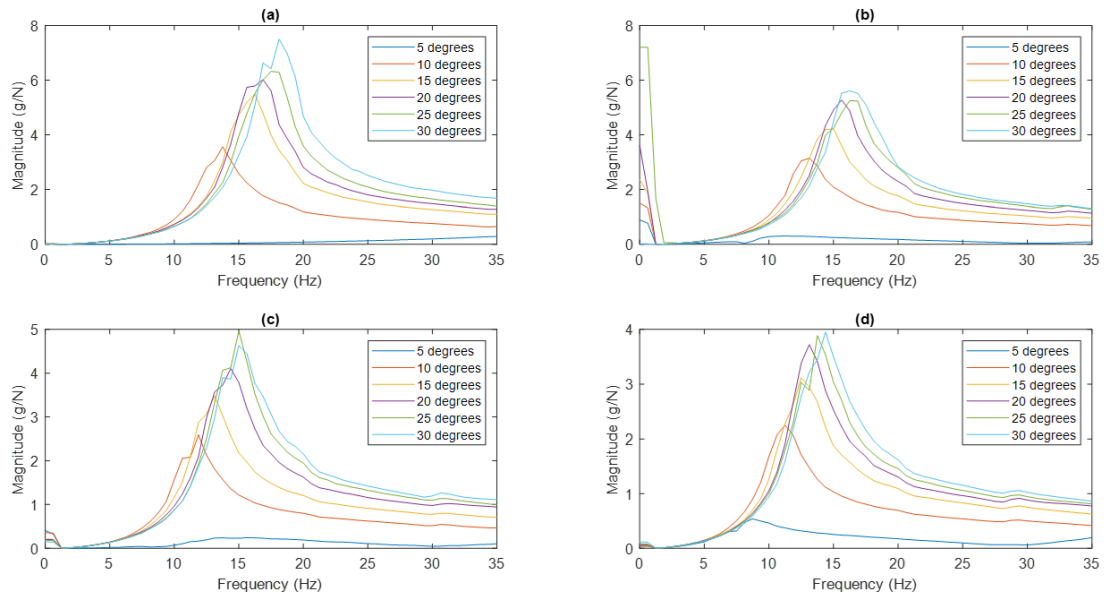


Figure 49: A frequency response plot of the single-stage truss IA coupled to a cantilever beam with a) 12g, b) 24g, c) 36g, and d) 48g of proof mass added to the tip of the cantilever.

In Figure 49 a), b), c) and d), the frequency response of the single-stage truss IA coupled to a cantilever beam is shown. Twenty-four test conditions are presented, which involve variations of the initial amplifier angle of the mechanism, from 5 to 30 degrees, in increments of five degrees, for various cantilever tip-masses, specifically 12, 24, 36, and 48g. The trends observed in each response graph, are consistent with those outlined in Figure 41 a), b), c) and d), for the single-stage IA coupled to a cantilever beam with tip mass. The sole distinction between the trends lies in the magnitude of the response for each test, which is considerably lower for the single-stage truss IA coupled to a cantilever beam with tip mass.

The main trends are as follows: as the initial amplifier angle increases, the natural frequency of the system increases. Additionally, for a given initial amplifier angle, the natural frequency of the system decreases as the quantity of cantilever tip mass increases. Furthermore, as the quantity of cantilever tip mass increases, the magnitude of the response decreases.

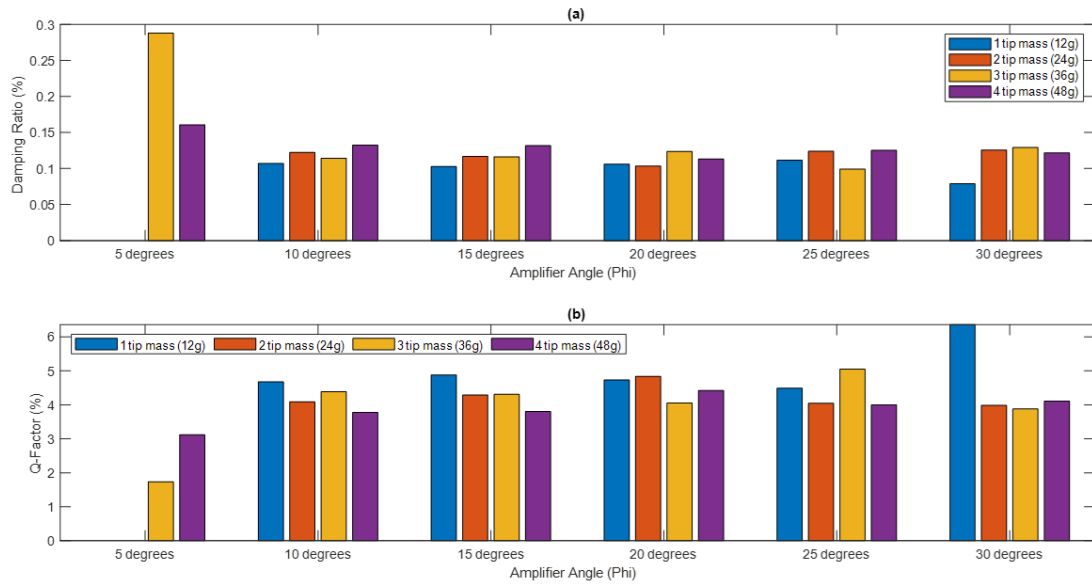


Figure 50: A bar chart to show a) the damping ratio, and b) the Q-factor of the single-stage truss IA coupled to a cantilever beam, when 12g, 24g, 36g and 48g of proof mass has been added to the tip of the cantilever.

Figure 50a) and b) illustrate the damping ratio and Q-factor characteristics of the single-stage truss IA when coupled to a cantilever beam, subject to varying initial amplifier angles and tip mass conditions. It is worth noting that the damping ratio of the system exhibits an inverse relationship with the reciprocal of the Q-factor of the system. The damping ratio and Q-factor characteristics are not displayed for an initial amplifier angle of 5 degrees, for 12g, and 24g of tip mass, since there is no clear natural frequency peak in Figure 49a) and b). When the quantity of proof mass added to the tip of the cantilever is 12g, compared to 24g, 36g and 48g, the damping ratio is lower across each initial amplifier angle. This is expected since the system contains less mass to dissipate energy through friction or other damping mechanisms.

5.2.3.6 Single-Stage Truss Inertial Amplifier with Joint Mass Coupled to a Cantilever Beam

In order to enhance the effective inertia of the single-stage truss IA, a proof mass is incorporated into certain joints of the mechanism. For a comprehensive understanding of the specific joints to which the proof mass is added, please refer to Section 3.1 or view Figure 43, Subsection 5.2.3.3. It is worth noting that the location of the proof mass on the single-stage truss IA is the same as that on the single-stage IA.

A sequence of electrodynamic shaker tests are conducted on the system to further investigate the impact of the single-stage truss IA on the behaviour of the cantilever beam. In each test, the initial amplifier angle of the mechanism is adjusted within the range of 5 to 30 degrees, in

increments of five degrees, with varying quantities of proof mass (specifically 12g, 24g, 36g, and 48g) added to the designated joints of the mechanism. The outcomes of these experiments are demonstrated in Figure 51 and Figure 52.

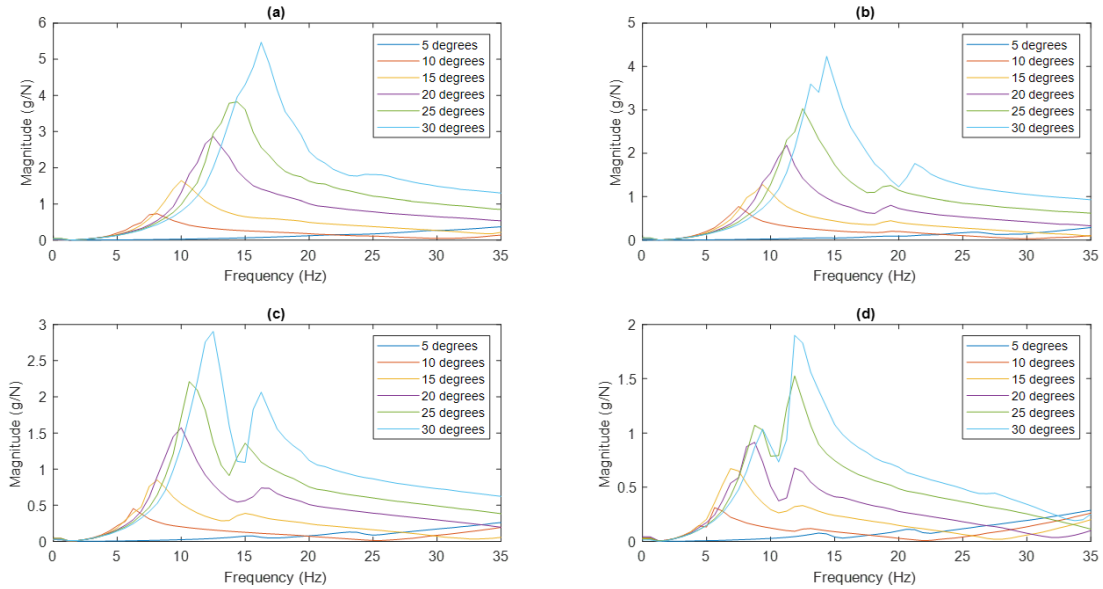


Figure 51: A frequency response plot of the single-stage truss IA coupled to a cantilever beam with a) 12g, b) 24g, c) 36g, and d) 48g of proof mass added to each specified joint of the mechanism.

In Figure 51a), b), c), and d), the frequency response of the single-stage truss IA coupled to a cantilever beam is shown; twenty-four conditions are presented, which involve variations of the initial amplifier angle of the mechanism, for different quantities of proof mass, specifically 12, 24, 36, and 48g added to each designated joint of the mechanism. The trends observed in each response graph, are consistent with those outlined in Figure 44a), b), c) and d), for the single-stage IA with joint mass coupled to a cantilever beam. The sole distinction between these trends lies in the magnitude of the response for each test, which is considerably lower for the single-stage truss IA with joint mass, coupled to a cantilever beam.

The main trends are as follows: as the initial amplifier angle increases, the natural frequency of the system increases. This trend suggests that for larger initial amplifier angles, the system generates less effective inertia. Additionally, for a given initial amplifier angle, the natural frequency of the system decreases slightly as the quantity of joint mass increases. This relationship is expected since the addition of proof mass to the system increases the effective mass of the system. Furthermore, as the quantity of joint mass increases, the magnitude of the response decreases, for all initial amplifier angles. For cases, 36g and 48g of proof mass added

to each specific joint of the mechanism, the system becomes slightly unstable, as evidenced by the unsmooth responses in Figure 51c) and d).

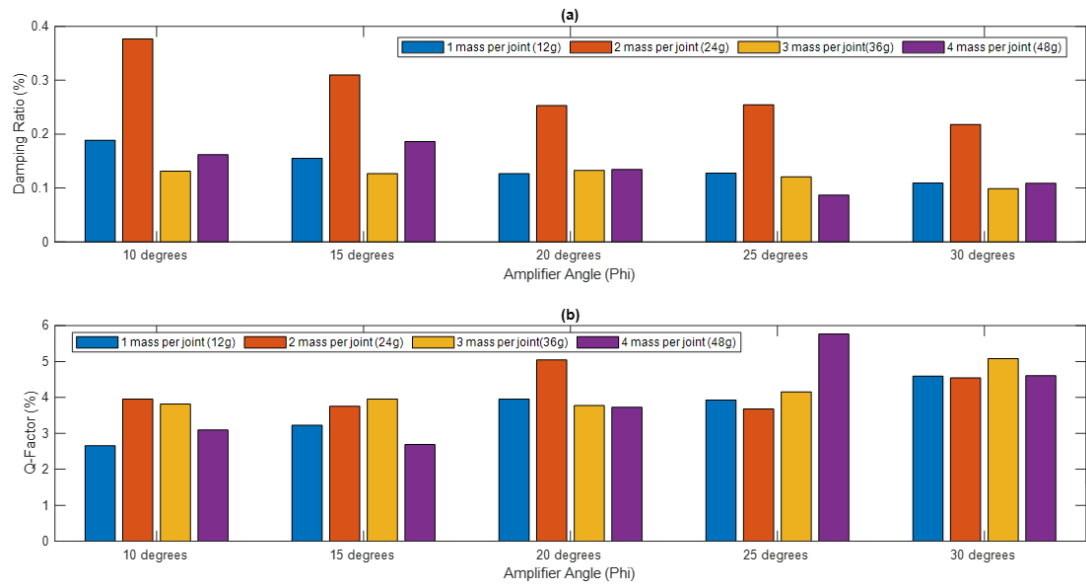


Figure 52: A bar chart to show a) the damping ratio, and b) the Q-factor of the single-stage truss IA coupled to a cantilever beam, when 12g, 24g, 36g and 48g of proof mass has been added to each specified joint of the mechanism.

Figure 52a) and b) illustrate the damping ratio and Q-factor characteristics of the single-stage truss IA when coupled to a cantilever beam, subject to different initial amplifier angles and joint mass conditions. It is worth noting that the damping ratio of the system exhibits an inverse relationship with the reciprocal of the Q-factor of the system. The damping ratio and Q-factor characteristics are not displayed for an initial amplifier angle of 5 degrees, since there is no clear natural frequency peak, for this initial amplifier angle in Figure 51 a), b), c) and d). When the quantity of proof mass added to each specified joint of the single-stage truss IA is 12g, or 24g, the damping ratio decreases and the Q-factor increases, for increasing initial amplifier angles. When the quantity of proof mass added to the mechanism is 36g, the damping ratio remains fairly consistent for different initial amplifier angles. However, for a proof mass of 48g there is no clear trend observed.

5.2.3.7 Compound Inertial Amplifier Coupled to a Cantilever Beam

Figure 53 shows a photograph of the compound IA coupled to a cantilever beam. In order to evaluate the dynamic behaviour of the compound IA when coupled to a cantilever beam, a series of electrodynamic shaker tests are performed on the system, utilizing the experimental set-up illustrated in Figure 26a), Subsection 5.1. Each test involves altering the initial amplifier angle of the primary mechanism from 10 to 30 degrees, in increments of five degrees. Note

that in order to achieve precise adjustments of the initial amplifier angle of the mechanism, the identical process is implemented as for that of each individual IA, explicitly outlined in Subsection 5.2.1.1 for the single-stage IA. The response of the compound IA when coupled to a cantilever beam can be seen in Figure 54 and Figure 55.

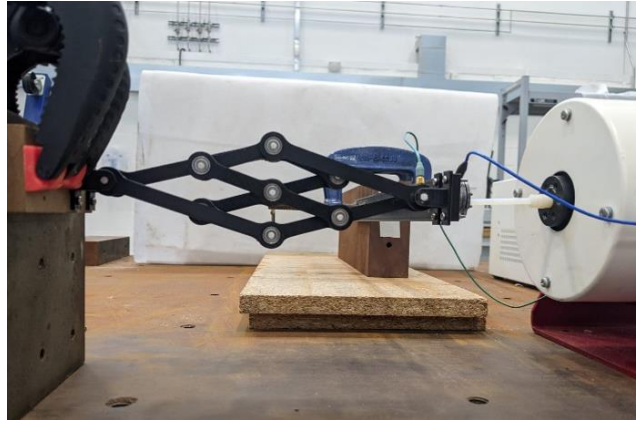


Figure 53: A photograph of the compound IA coupled to a cantilever beam.

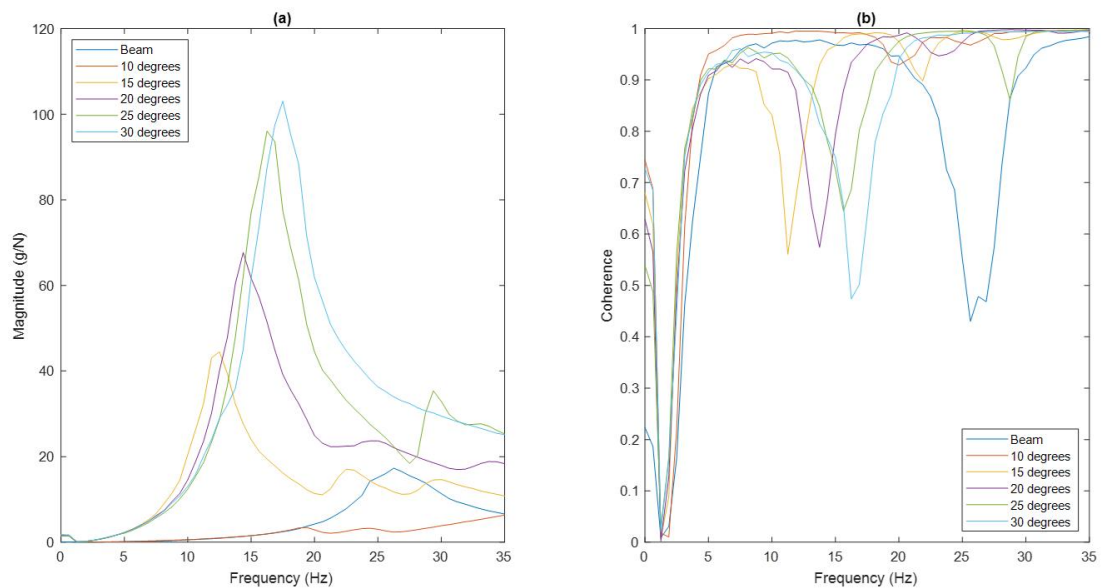


Figure 54: a) A frequency response plot of the compound IA coupled to a cantilever beam. b) A coherence plot of the compound IA coupled to a cantilever beam.

Figure 54a) illustrates the response of the compound IA when coupled to a cantilever beam, for various initial amplifier angles, 10, 15, 20, 25, and 30 degrees. For an initial amplifier angle of 10 degrees, no distinct resonance is apparent. In contrast, for initial amplifier angles 15, 20, 25, and 30 degrees, the natural frequency of the system is 12.5 Hz, 14.38 Hz, 16.25 Hz, and 17.5 Hz, respectively. A clear trend is observed whereby an increase in the initial amplifier angle of the mechanism leads to a corresponding rise in the natural frequency of the system.

This indicates that there is less effective inertia within the system for larger initial amplifier angles. Furthermore, as the initial amplifier angle increases, the magnitude of the response of the system also increases, with the largest response observed when the initial amplifier angle of the system is 30 degrees. For this case, the magnitude of the response is approximately five times that of the cantilever beam.

Figure 54b) shows the coherence plot which corresponds to the frequency response plot in Figure 54a). For each test, the coherence drops at the natural frequency of the system. This suggests that the linear correlation between the input and output signals diminishes at each natural frequency, which may be caused by non-linearities within the system.

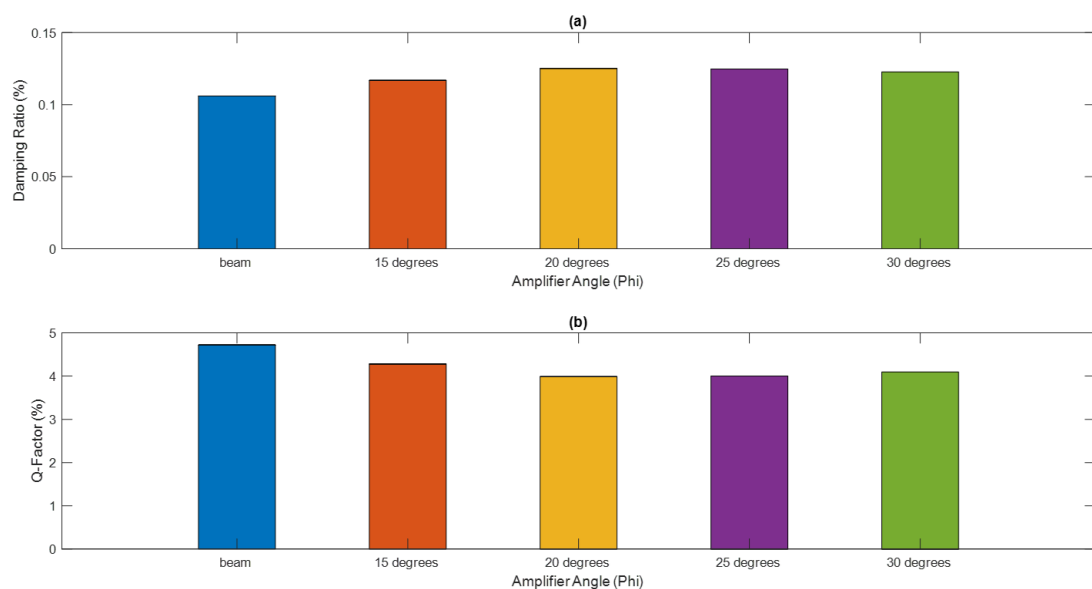


Figure 55: A bar chart to show a) the damping ratio, and b) the Q -factor of the compound IA coupled to a cantilever beam, for different test conditions.

In Figure 55a), the damping ratio of the system is presented as 0.117%, 0.125%, 0.125%, and 0.123% for initial amplifier angles of 15, 20, 25, and 30 degrees, respectively. Notably, no damping ratio is provided for an initial amplifier angle of 10 degrees due to the absence of a distinct natural frequency under this condition. The data trend indicates that an increase in the initial amplifier angle of the mechanism results in a corresponding increase in the damping ratio of the system, except for when the initial amplifier angle is 25 and 30 degrees. In these two cases, the damping ratio remains constant and slightly decreases, respectively. Overall, the damping ratio of the system does not degrade significantly compared to that of the unaltered beam.

In Figure 55b) the Q-factor of the system is shown as 4.28%, 3.99%, 4.00% and 4.10%, when the initial amplifier angle of the mechanism is 15, 20, 25 and 30 degrees, respectively. The Q-factor of the system is not given for an initial amplifier angle of 10 degrees because there is no observable natural frequency peak. The general trend of the graph shows that as the initial amplifier angle of the mechanism increases, the Q-factor of the system decreases, except for when the initial amplifier angle is 25 and 30 degrees. For these two cases, the Q-factor remains constant and slightly increases, respectively. Note that the Q-factor of the system is directly proportional to the reciprocal of the damping ratio of the system.

5.2.3.8 Compound Inertial Amplifier Coupled to a Cantilever Beam with Tip Mass

To further assess the influence of the compound IA on the behaviour of the cantilever, additional electrodynamic shaker tests are conducted on the system. Each test involves altering the initial amplifier angle of the primary mechanism between 10 to 30 degrees, in increments of five degrees, but for varying quantities of proof mass added to the tip of the cantilever, specifically 12g, 24g, 36g, and 48g. Note that proof mass is introduced to the cantilever, as shown in Figure 36 Subsection 5.2.2, in an effort to stimulate the effects of the IA. The results of these experiments are illustrated in Figure 56 and Figure 57.

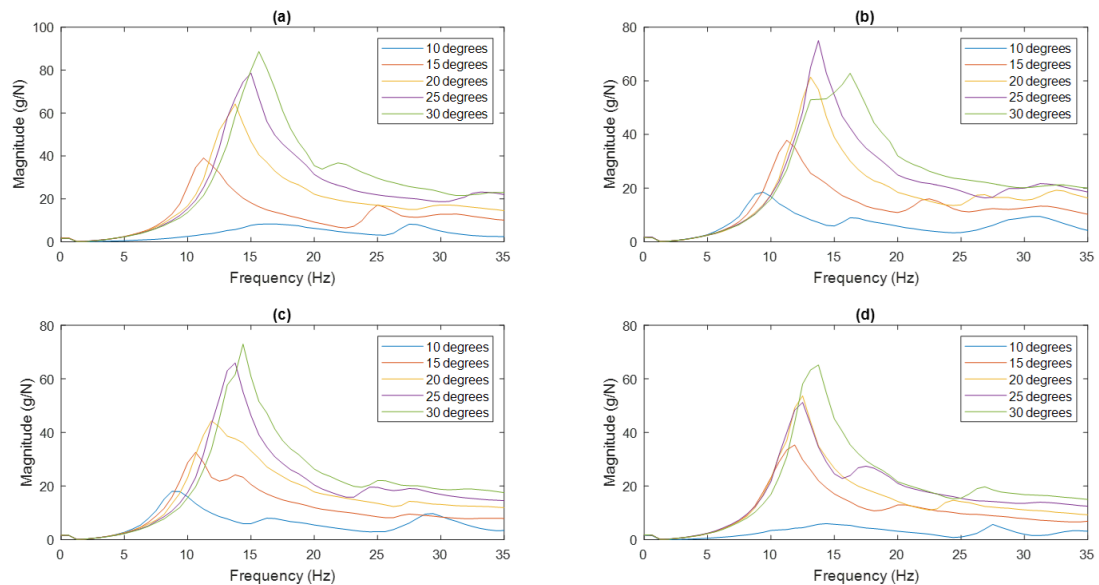


Figure 56: A frequency response plot of the compound IA coupled to a cantilever beam with a) 12g, b) 24g, c) 36g, and d) 48g of proof mass added to the tip of the cantilever.

In Figure 56a), b), c) and d), the frequency response of the compound IA coupled to a cantilever beam is shown. Twenty test conditions are presented, which involve variations of the initial amplifier angle of the mechanism, from 10 to 30 degrees, in increments of five degrees, for various cantilever tip-masses, specifically 12, 24, 36, and 48g. When 12 or 36g of proof mass is added to the tip of the cantilever a clear trend is shown, whereby an increase in the initial amplifier angle of the system corresponds to a rise in the natural frequency of the system. Similarly, when 24g of proof mass is added to the tip of the cantilever, the aforementioned trend is evident, although there is an exception when the initial amplifier angle of the compound IA is 30 degrees. Likewise, the addition of 48g of proof mass to the tip of the cantilever yields the same pattern, with an exception when the initial amplifier angle of the mechanism is 25 degrees. Another notable observation is that for a fixed initial amplifier angle, the natural frequency of the system typically decreases as the quantity of cantilever tip mass increases. Furthermore, unlike the single-stage and single-stage truss IAs, when coupled to a cantilever beam with tip mass, the quantity of proof mass has no real relationship with the magnitude of the system's response.

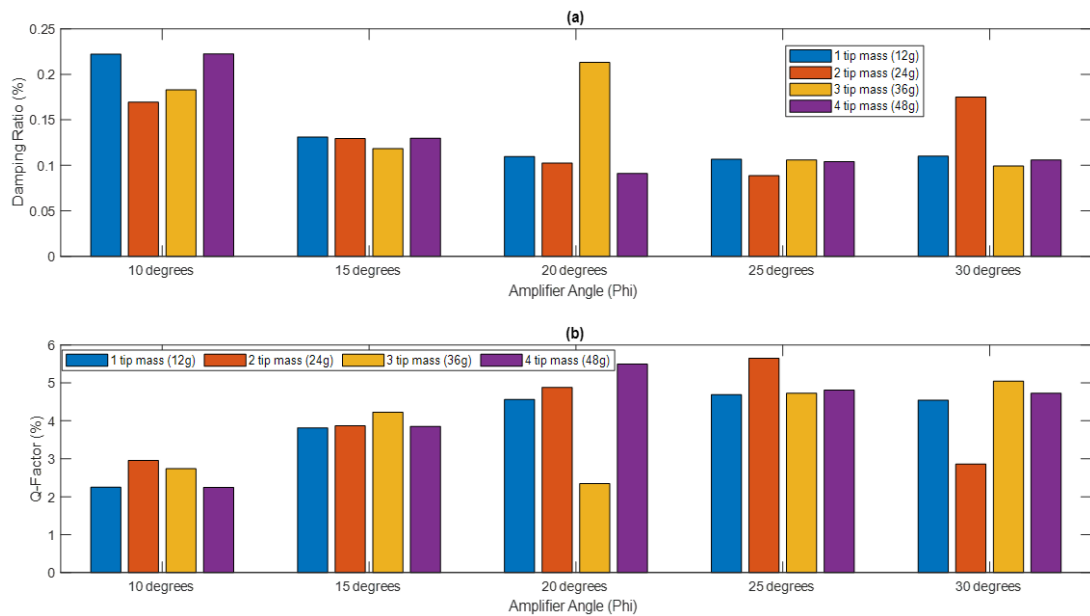


Figure 57: A bar chart to show a) the damping ratio, and b) the Q-factor of the compound IA coupled to a cantilever beam, when 12g, 24g, 36g and 48g of proof mass has been added to the tip of the cantilever.

Figure 57a) and b) illustrate the damping ratio and Q-factor characteristics of the compound IA when coupled to a cantilever beam, subject to different initial amplifier angles and tip mass conditions. It is worth noting that the damping ratio of the system exhibits an inverse relationship with the reciprocal of the Q-factor of the system. When the quantity of proof mass

added to the tip of the cantilever is 12g, the damping ratio of the system decreases and the Q-factor of the system increases, for increasing initial amplifier angles. Additionally, when the initial amplifier angle of the compound IA is 15 degrees, there is not much deviation between the damping ratios and Q-factors for different mass quantities.

5.2.3.9 Compound Inertial Amplifier with Joint Mass Coupled to a Cantilever Beam

To improve the effective inertia of the compound IA, a proof mass is added to specific joints of the mechanism, as displayed in Figure 58. For a detailed understanding of the precise joints to which the proof mass is added, refer to Section 3.2.

A sequence of electrodynamic shaker tests are performed on the system, to further assess the influence of the compound IA on the behaviour of the cantilever beam. In each test, the initial amplifier angle of the primary mechanism is adjusted within the range of 10 to 30 degrees, in increments of five degrees, with varying quantities of proof mass, specifically 12g, 24g, 36g, and 48g added to the designated joints of the mechanism. The outcomes of these experiments are presented in Figure 59 and Figure 60.

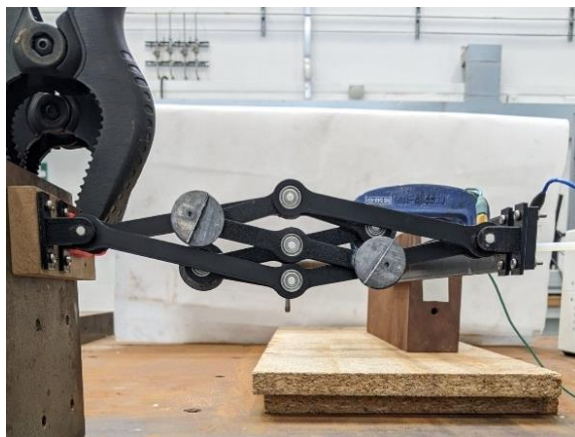


Figure 58: A photograph of the compound IA coupled to a cantilever beam, with 18g of proof mass at each specified joint of the mechanism.

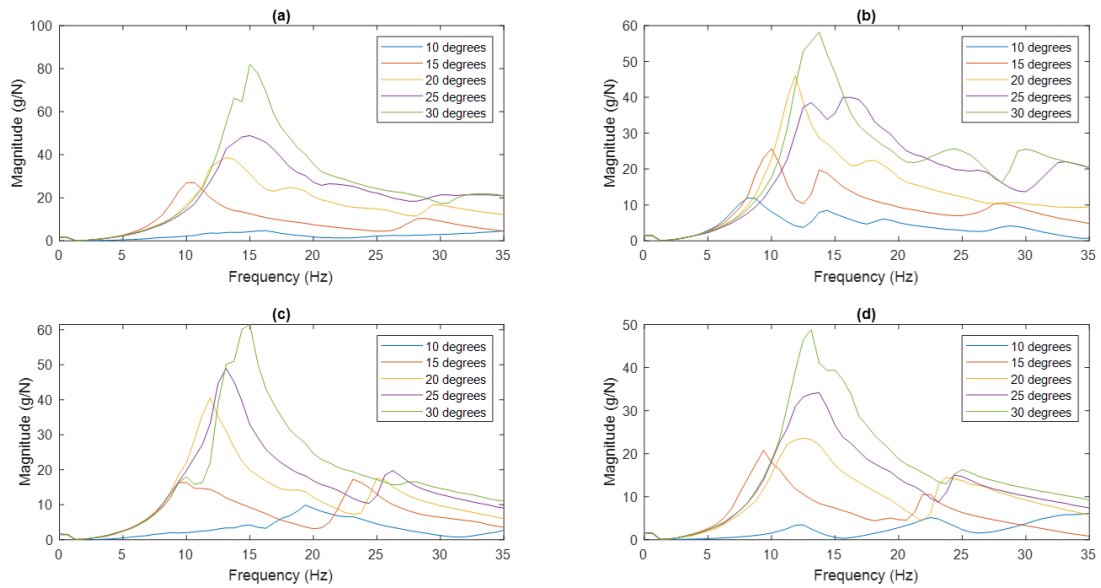


Figure 59: A frequency response plot of the compound IA coupled to a cantilever beam with a) 6g, b) 12g, c) 18g, and d) 24g of proof mass added to each specified joint of the mechanism.

In Figure 59a), b), c), and d), the frequency response of the compound IA coupled to a cantilever beam is shown; twenty conditions are presented, which involve variations of the initial amplifier angle of the mechanism from 10 to 30 degrees, for different quantities of proof mass, specifically 6, 12, 18, and 24g added to each designated joint of the mechanism. Among all frequency response tests a general trend is shown, whereby an increase in the initial amplifier angle of the mechanism corresponds to a rise in the natural frequency of the system. Additionally, for a given initial amplifier angle, the natural frequency of the system typically decreases as the quantity of proof mass, added to each specified joints of the mechanism, increases. Furthermore, as the quantity of proof mass added to the compound IA increases, the magnitude of the response of the system decreases. Nonetheless, some deviations from these generalised relationships are observed.

When the compound IA has 12g of proof mass, the magnitude of the natural frequency peak is lower for an initial amplifier angle of 25 degrees compared to an initial amplifier angle of 20 degrees. Moreover, even though a clear natural frequency peak is absent when the compound IA features 12g proof mass and an initial amplifier angle of 25 degrees, these conditions yield the highest natural frequency measurement for the system. Similarly, when the compound IA has 24g of proof mass, the natural frequency of the system is lower for an initial amplifier angle 30, compared to an initial amplifier angle of 25 degrees. Furthermore, when the initial amplifier angle of the mechanism is 20 degrees, the magnitude of the response is lower for a proof mass of 6g, compared to a proof mass of 12g.

Across all experiments conducted, the response appears to lack complete smoothness and clarity, suggesting that the compound IA with joint mass may exhibit a slight degree of instability when coupled to a cantilever beam.

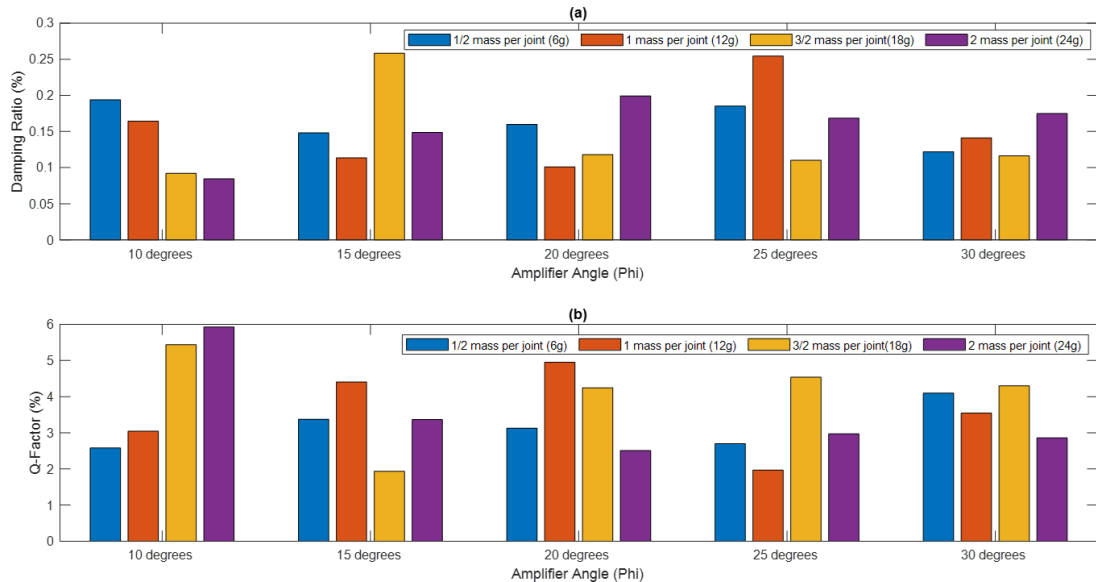


Figure 60: A bar chart to show a) the damping ratio, and b) the Q-factor of the compound IA coupled to a cantilever beam, when 6g, 12g, 18g and 24g of proof mass has been added to each specified joint of the mechanism.

Figure 60a) and b) display the damping ratio and Q-factor characteristics of the compound IA when coupled to a cantilever beam, subject to different initial amplifier angles and joint mass conditions. It is worth noting that the damping ratio of the system exhibits an inverse relationship with the reciprocal of the Q-factor of the system. When the initial amplifier angle of the compound IA is 10 degrees, the damping ratio decreases and the Q-factor increases, for increasing quantities of proof mass, added to each specific joint of the mechanism. This trend is expected since there will be more effective mass within the system, for greater quantities of proof mass, and the damping ratio of the system is inversely proportional to the square root of the effective mass of the system. However, for other initial amplifier angle conditions, no clear trends are observed for the damping ratio and Q-factor characteristics of the system in response to changes in the quantity of proof mass. This lack of a clear trend may be due to nonlinearities present within the system.

5.2.3.10 Compound Truss Inertial Amplifier Coupled to a Cantilever Beam

In order to evaluate the dynamic behaviour of the compound truss IA when it is coupled to a cantilever beam, a series of electrodynamic shaker tests are performed on the system, utilizing the experimental set-up illustrated in Figure 26a), Subsection 5.1. Each test involves altering the initial amplifier angle of the primary mechanism from 10 to 30 degrees, in increments of five degrees. Figure 61 and Figure 62 display the results of these experiments. Note that to achieve precise adjustments of the initial amplifier angle of the mechanism, the identical process is implemented as for that of each individual IA, explicitly outlined in Subsection 5.2.1.1 for the single-stage IA.

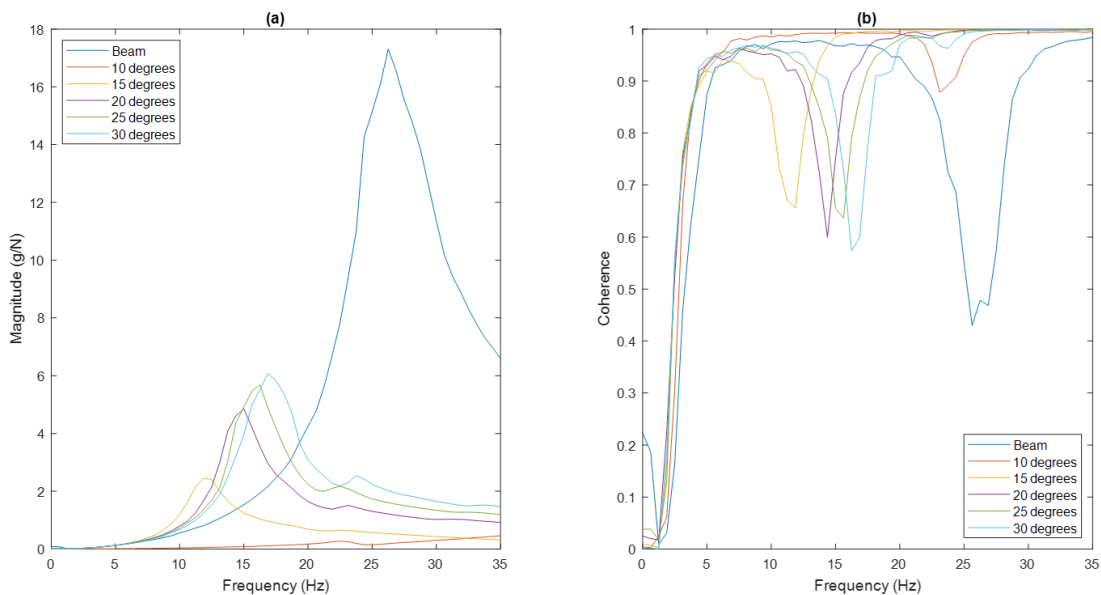


Figure 61: a) A frequency response plot of the compound truss IA coupled to a cantilever beam. b) A coherence plot of the compound truss IA coupled to a cantilever beam.

Figure 61a) illustrates the response of the compound truss IA when coupled to a cantilever beam, for various initial amplifier angles from 10 to 30 degrees. For an initial amplifier angle of 10 degrees, no distinct resonance is apparent. In contrast, for initial amplifier angles 15, 20, 25, and 30 degrees, the natural frequency of the system is 11.88Hz, 15.00Hz, 16.25Hz, 16.88Hz, respectively. A clear trend is observed whereby an increase in the initial amplifier angle of the mechanism leads to a corresponding rise in the natural frequency of the system. This indicates that there is less effective inertia within the system for larger initial amplifier angles. Furthermore, as the initial amplifier angle increases, the magnitude of the response of the system also increases. Each response is consistent with that found in Subsection 5.2.3.7, which examines the compound IA coupled to a cantilever beam. In both cases, the natural frequencies occur at approximately the same values. However, unlike the responses for the

compound IA, the magnitude of the responses for the compound truss IA are lower than that of the cantilever beam.

Figure 61b) shows the coherence plot which corresponds to the frequency response plot in Figure 61a). For each test, the coherence drops at the natural frequency of the system. This suggests that the linear correlation between the input and output signals diminishes at each natural frequency, which may be caused by non-linearities within the system.

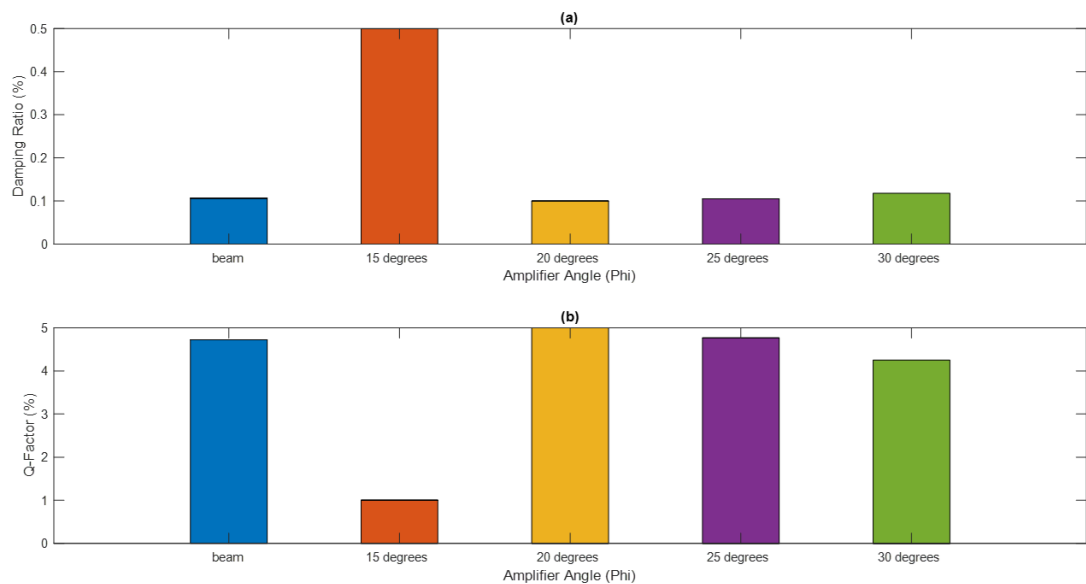


Figure 62: A bar chart to show a) the damping ratio, and b) the Q -factor of the compound truss IA coupled to a cantilever beam, for different test conditions.

In Figure 62a), the damping ratio of the system is presented as 0.499%, 0.100%, 0.105%, and 0.118%, respectively, for initial amplifier angles of 15, 20, 25, and 30 degrees. The damping ratio is not displayed for an initial amplifier angle of 10 degrees because there is no clear natural frequency for this condition. The damping ratio for the compound truss IA with an initial amplifier angle of 20, 25, and 30 degrees, is not much different from that of the cantilever, which has a damping ratio of 0.106%. In contrast, when the initial amplifier angle of the mechanism is 15 degrees the damping ratio is significantly higher.

In Figure 62b), the Q -factor of the system is shown as 3.96%, 4.85%, 5.49%, 5.26% and 5.29%, respectively, for initial amplifier angles of 15, 20, 25 and 30 degrees. The Q -factor is not provided for an initial amplifier angle of 10 degrees because there is no visible natural frequency peak in Figure 61a). The data trend in Figure 62b) demonstrates the inverse relationship to that in Figure 62a) regarding the damping ratio characteristics of the compound

truss IA. This is attributed to the fact that the Q-factor of the system is directly proportional to the reciprocal of the damping ratio of the system.

5.2.3.11 Compound Truss Inertial Amplifier Coupled to a Cantilever Beam with Tip Mass

To further assess the influence of the compound truss IA on the behaviour of the cantilever beam, additional electrodynamic shaker tests are conducted on the system. Each test involves altering the initial amplifier angle of the primary mechanism between 10 to 30 degrees, in increments of five degrees, but for varying quantities of proof mass added to the tip of the cantilever, specifically 12g, 24g, 36g, and 48g. Note that proof mass is introduced to the cantilever, as shown in Figure 36 Subsection 5.2.2, in an effort to stimulate the effects of the IA. The results of these experiments are illustrated in Figure 63 and Figure 64.

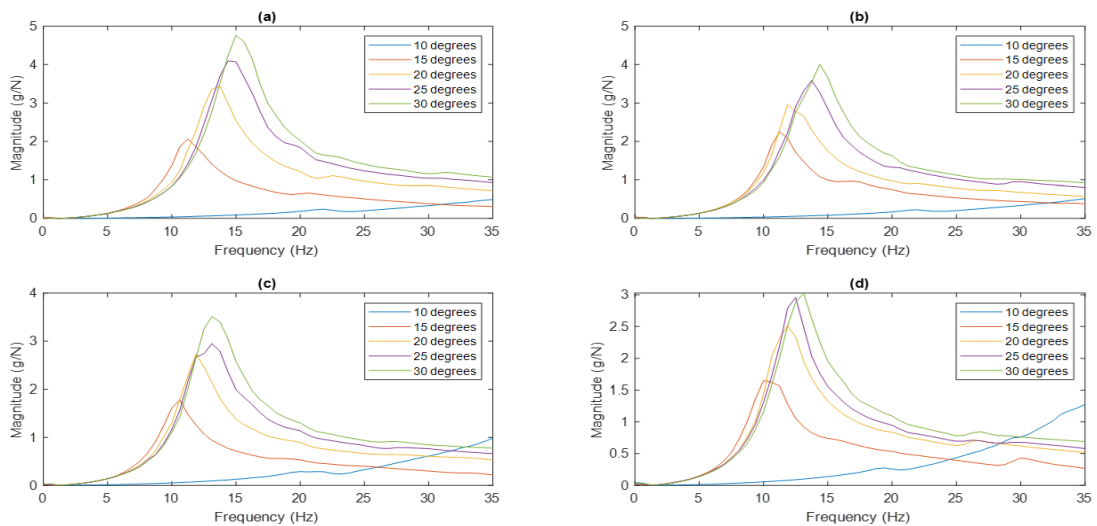


Figure 63: A frequency response plot of the compound truss IA coupled to a cantilever beam with a) 12g, b) 24g, c) 36g, and d) 48g of proof mass added to the tip of the cantilever.

In Figure 63a), b), c) and d), the frequency response of the compound truss IA coupled to a cantilever beam is shown. Twenty test conditions are presented, which involve variations of the initial amplifier angle of the mechanism, from 10 to 30 degrees, in increments of five degrees, for various cantilever tip-masses, specifically 12, 24, 36, and 48g. Across all experiments, a distinct trend is shown, whereby an increase in the initial amplifier angle of the mechanism corresponds to a rise in the natural frequency of the system. This trend suggests that the system generates less effective inertia for larger initial amplifier angles. Additionally,

for a given initial amplifier angle, the natural frequency of the system typically decreases as the quantity of cantilever tip mass increases. This relationship is anticipated, as the effective mass of a system is proportional to the square root of the natural frequency of the system, and the inclusion of proof mass augments the effective mass of the system. Furthermore, as the quantity of cantilever tip mass increases, the magnitude of the response decreases. This is an expected trend, since the motion of the system is dependent on the natural frequency of the system. It should be noted that this system exhibits a considerably lower magnitude frequency response for each test, when compared to the magnitude of the frequency response for the counterpart of this system, the compound IA coupled to a cantilever beam with tip mass, discussed in Subsection 5.2.3.8.

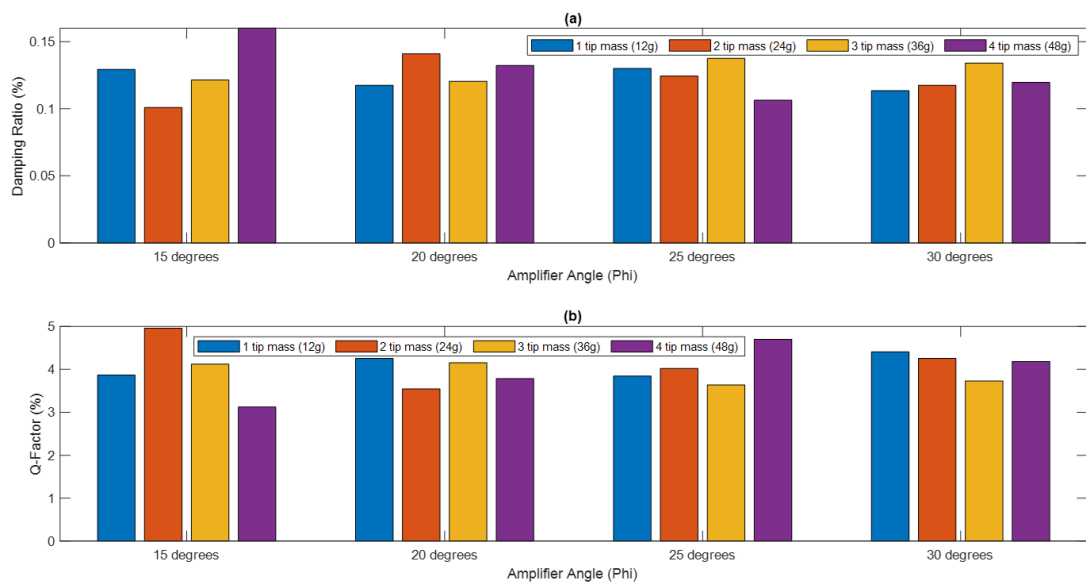


Figure 64: A bar chart to show a) the damping ratio, and b) the Q-factor of the compound truss IA coupled to a cantilever beam, when 12g, 24g, 36g and 48g of proof mass has been added to the tip of the cantilever.

Figure 64a) and b) illustrate the damping ratio and Q-factor characteristics of the compound truss IA when coupled to a cantilever beam, subject to different initial amplifier angles and tip mass conditions. For this system, there is no discernible trend between the quantity of proof mass added to the tip of the cantilever, the initial amplifier angle of the mechanism, and the damping or Q-factor characteristics of the system.

5.2.3.12 Compound Truss Inertial Amplifier with Joint Mass Coupled to a Cantilever Beam

To improve the effective inertia of the compound truss IA, a proof mass is added to specific joints of the mechanism, as displayed in Figure 65. For a detailed understanding of the precise joints to which the proof mass is added, refer to Section 3.2.

A sequence of electrodynamic shaker tests are performed on the system, to further assess the influence of the compound truss IA on the behaviour of the cantilever beam. In each test, the initial amplifier angle of the primary mechanism is adjusted within a range of 10 to 30 degrees, in increments of five degrees, for varying quantities of proof mass, specifically 12g, 24g, 36g, and 48g. The outcomes of these experiments are presented in Figure 66 and Figure 67.

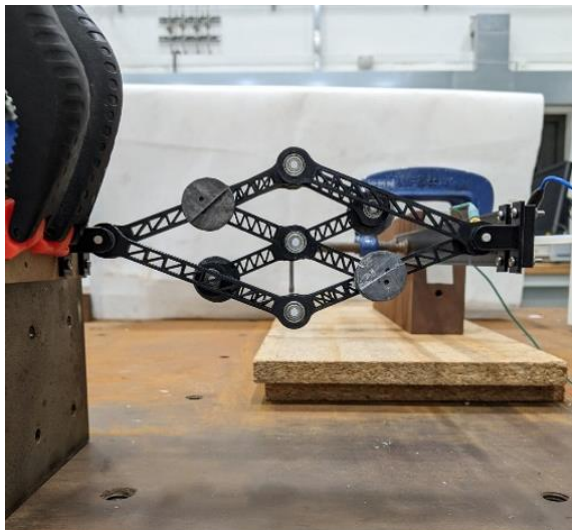


Figure 65: A photograph of the compound truss IA with 18g of proof mass at each specified joint of the mechanism.

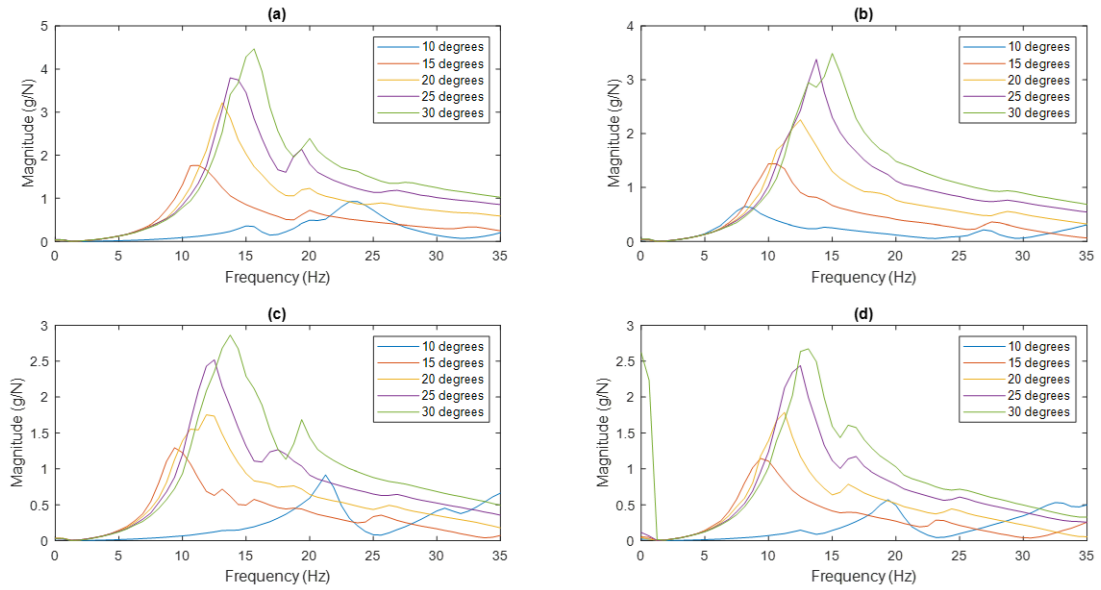


Figure 66: A frequency response plot of the compound truss IA coupled to a cantilever beam with a) 6g, b) 12g, c) 18g, and d) 24g of proof mass added to each specified joint of the mechanism.

In Figure 66a), b), c), and d), the frequency response of the compound truss IA coupled to a cantilever beam is shown; twenty conditions are presented, which involve variations of the initial amplifier angle of the mechanism, for different quantities of proof mass, specifically 6, 12, 18, and 24g added to each designated joint of the mechanism. Among all frequency response tests a general trend is shown, whereby an increase in the initial amplifier angle of the mechanism corresponds to a rise in the natural frequency of the system. Additionally, for a given initial amplifier angle, the natural frequency of the system decreases slightly as the quantity of proof mass added to each specified joints of the mechanism increases. Furthermore, as the quantity of proof mass added to the compound truss IA increases, the magnitude of the response of the system decreases. These trends hold true across all test cases except when the compound truss IA possesses an initial amplifier angle of 10 degrees. In this specific case, no clear patterns are observed between the magnitude of the response of the system and the natural frequency of the system, for different amounts of proof mass.

The compound truss IA with joint mass coupled to a cantilever beam exhibits a considerably lower magnitude response for each test, when compared to the magnitude of the responses for the counterpart of this system, the compound IA with joint mass coupled to a cantilever beam, discussed in Subsection 5.2.3.9. Note that the responses observed for the compound truss IA with joint mass coupled to a cantilever beam are smoother, than those of the compound IA with joint mass coupled to a cantilever beam, therefore the system evaluated here, may be more stable than its solid counterpart.

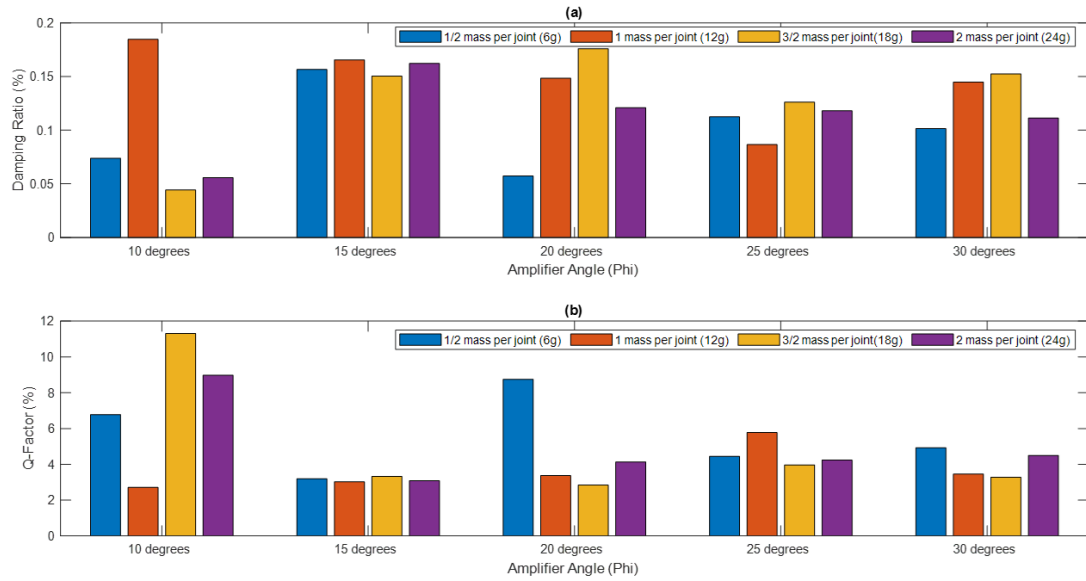


Figure 67: A bar chart to show a) the damping ratio, and b) the Q -factor of the compound truss IA coupled to a cantilever beam, when 6g, 12g, 18g and 24g of proof mass has been added to each specified joint of the mechanism.

Figure 67a) and b) display the damping ratio and Q -factor characteristics of the compound truss IA when coupled to a cantilever beam, subject to different initial amplifier angles and joint mass conditions. It is worth noting that the damping ratio of the system exhibits an inverse relationship with the reciprocal of the Q -factor of the system. When the initial amplifier angle of the compound truss IA is 10 degrees, some quantities of proof mass, specifically 18g, decrease the damping ratio characteristics and increase the Q -factor characteristics of the system, whilst other quantities of proof mass do not. When the initial amplifier angle of the mechanism is 15 degrees, the damping ratio and Q -factor characteristics remain fairly constant for different quantities of proof mass. However, for other initial amplifier angle conditions, no clear trends are observed for the damping ratio and Q -factor characteristics of the system, in response to changes in the quantity of proof mass. This lack of a clear trend may be due to nonlinearities present within the system.

6. Discussion

In the first set of experimental tests, the pure mass effect of each IA is analysed for varying initial amplifier angles. The initial amplifier angle of each IA is chosen as an experimental variable, based on the mathematical analysis conducted in Section 3. The experimental results reveal that the single-stage, single-stage truss, compound, and compound truss IAs exhibit a fairly consistent response across a wide frequency range, regardless of any alterations in effective mass, resonances, or damping effects. This observation suggests that these IAs

possess stability, reliability, and adaptability, making them well-suited for real-life applications such as vibration-based energy harvesting and atomic force microscopy.

However, it is important to note that for the smallest initial amplifier angles, specifically 5 degrees for the single-stage and single-stage truss IAs, and 10 degrees for the compound and compound truss IAs, the frequency response slightly deteriorates compared to the largest initial amplifier angle of 30 degrees. This may indicate an increase in nonlinearity for each device as smaller initial amplifier angles are approached.

On the other hand, the nested and nested truss IAs exhibit an inconsistent mass effect across a range of frequencies, likely due to the complexities and nonlinearities inherent in these mechanisms. As a result, no further tests on the nested and nested truss IAs were presented beyond the pure mass tests, given their instabilities.

For all the IAs examined, a comparison is made between the experimental magnitude of response values and the analytical magnitude of response values, calculated based on the linearized equations of motion derived in Section 3. For the single-stage, single-stage truss, compound, and compound truss IAs, it is observed that the analytical values consistently fall below the experimental values. This discrepancy may be attributed to the nonlinearities present in each IA or the experimental errors involved in determining the initial amplifier angles, which the system appears to be particularly sensitive to. For the nested and nested truss IAs, no clear trend is observed, due to the non-uniform experimental frequency response.

For the second experimental test, the dynamic behaviour of the cantilever beam is evaluated. The natural frequency, damping ratio, and Q-factor characteristics are obtained as 26.25Hz, 0.106%, and 4.71%, respectively. The experimental natural frequency value significantly deviates from the analytical value, 15.08Hz, calculated in Section 4, Subsection 4.1.5 of this work. This discrepancy could be attributed to various factors including, but not limited to, inaccuracies in the material properties, manufacturing methods, boundary conditions, geometrical dimensions of the cantilever, and, or experimental equipment.

The third series of experimental tests showcase the impact of the single-stage, single-stage truss, compound, and compound truss IAs on the dynamic behaviour of the cantilever beam, when subject to varying test conditions. Such conditions encompass modifications to the initial amplifier angle of each mechanism, as well as adjustments to the quantity and position of proof mass within each system. Each IA has the ability to enhance the effective inertia

properties of the cantilever beam, thereby causing changes to its natural frequency, damping ratio, and Q-factor characteristics. These variations are evident through the values presented in Table 13 and Table 14, which can be found in the Appendix, Section 8 - Sub-Section 8.2.

The effective inertia properties of each individual IA can be modified through effective geometrical adjustments, specifically initial amplifier angle changes. This conclusion is drawn based on the observed correlation between the outcomes of each experimental test. The mathematical models derived in Section 3 indicate that the initial amplifier angle of each IA, affects the effective mass characteristics of the respective system, therefore these analytical models can be concluded valid.

Figure 68 graphically illustrates the trend between the initial amplifier angle of each IA and the corresponding natural frequency of the system, thus effective mass relationship. As the initial amplifier angle of each IA increases, the effective mass within each system decreases, leading to an increase in the natural frequency of each system. Additionally, the results show that when coupled to a cantilever beam, the single-stage IA has the most extensive range for altering the first natural frequency, as compared to the other IAs. Furthermore, Figure 68 illustrates that, despite the design variation between corresponding mechanisms, the natural frequency remains relatively constant. This observation suggests that the mass differences, such as the 2g variance between the single stage and single-stage truss IAs, and the 3g difference between the compound and compound truss IAs, have minimal effect on the overall performance of each IA.

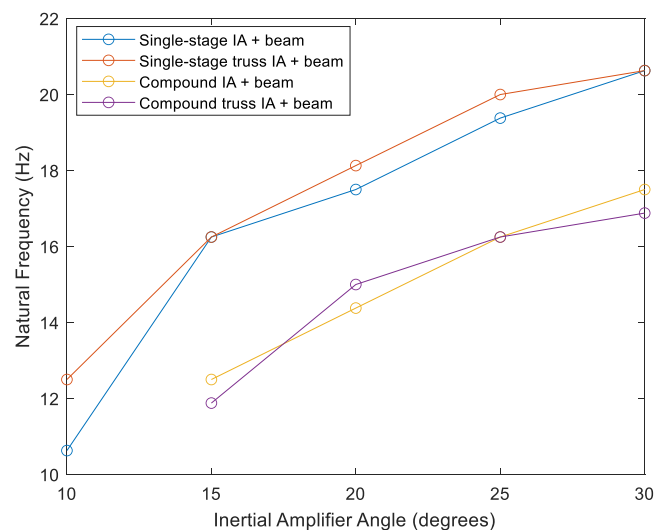


Figure 68: A graph to show the natural frequency of the single-stage, single-stage truss, compound, and compound truss IAs when coupled to a cantilever beam, for varying initial amplifier angles.

The corresponding damping ratio and Q-factor characteristics for the natural frequency values shown in Figure 68 are displayed in Figure 69a) Figure 69b), respectively. As stated throughout this study, the damping ratio characteristics are inversely proportional to the Q-factor characteristics for each system. It is desirable to have a low damping ratio for each experimentally tested system, since a low damping ratio indicates that the system's oscillations can be sustained over a long period of time. The results in Figure 69a) indicate that the lowest damping ratio is achieved by the single-stage IA with an initial amplifier angle of 30 degrees, when coupled to a cantilever beam. The highest damping ratio is obtained when the compound truss IA is coupled to a cantilever beam, with an initial amplifier angle of 15 degrees. Note that this response deviates from the uniform trend shown in Figure 69a). Correspondingly, Figure 69b) highlights that the compound truss IA boasts the most extensive Q-factor range, when compared to the other IA configurations. This finding suggests that the compound truss IA would be the most suitable IA for use in tapping mode atomic force microscopy applications.

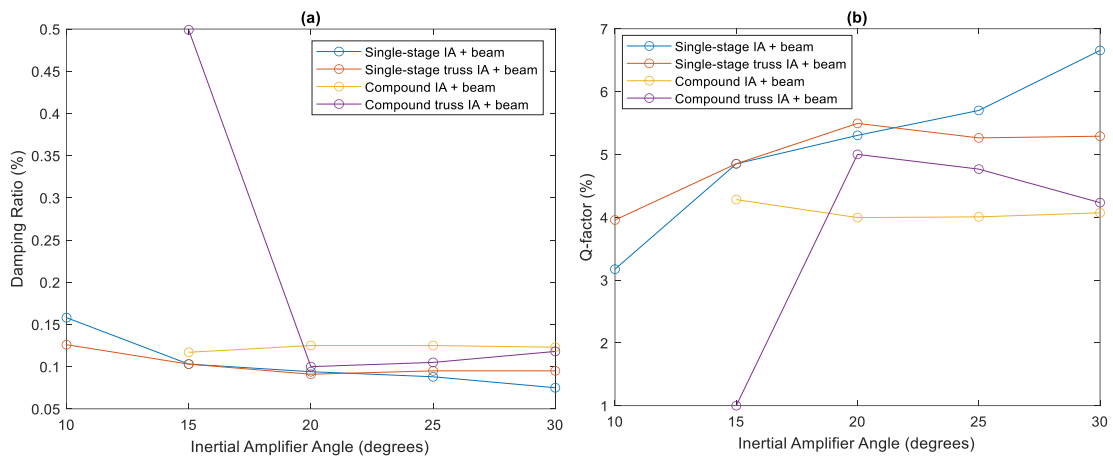


Figure 69: A graph to show a) the damping ratio, and b) the Q-factor of the single-stage, single-stage truss, compound, and compound truss IAs when coupled to a cantilever beam, for varying initial amplifier angles.

In Figure 70 a comparison of the results is shown for each IA coupled to a cantilever beam, when subject to varying quantities of proof mass, added to the tip of the cantilever. According to the data, there is a reliable pattern indicating that as the initial amplifier angle of each IA increases, the damping ratio of the respective system decreases. This trend is unexpected, since the effective mass of each IA decreases for larger initial amplifier angles, which should theoretically lead to an increase in the damping ratio of each system. The same relationship can be observed in Figure 71, which shows a comparison of the results for each IA coupled to a cantilever beam and subject to varying quantities of proof mass, added to each specified joint

of the mechanism. This phenomenon is also shown in the behaviour of the inerter, whereby achieving a purely inertial or apparent mass effect is challenging because of the significant amount of damping introduced into the system [126]. It appears that when the effective mass of each IA is amplified, the effective damping of the system is also amplified.

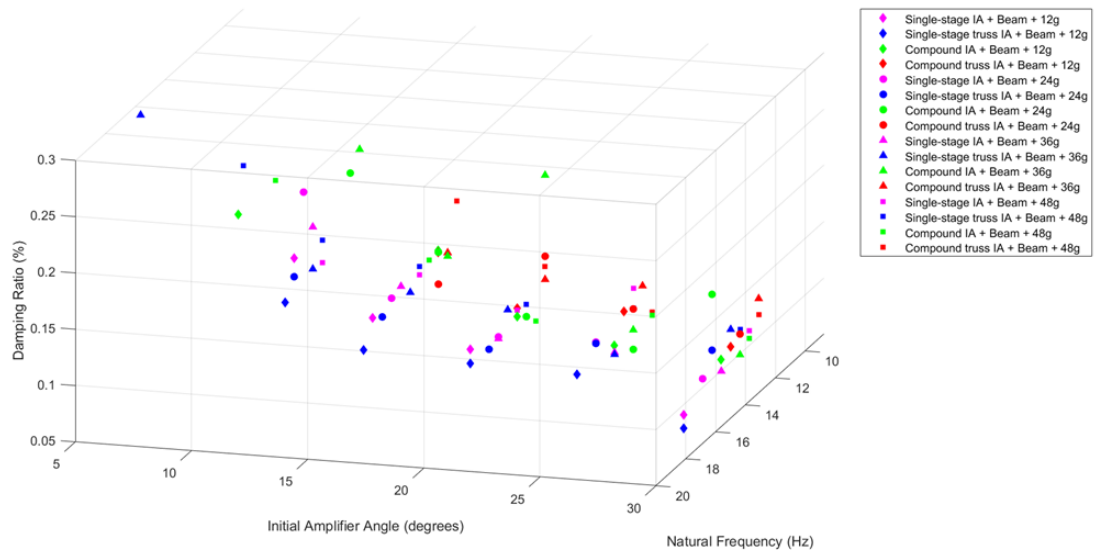


Figure 70: A graph to show the damping ratio and natural frequency characteristics for each IA coupled to a cantilever beam, corresponding to different initial amplifier angles for each IA and varying quantities of proof mass added to tip of the cantilever.

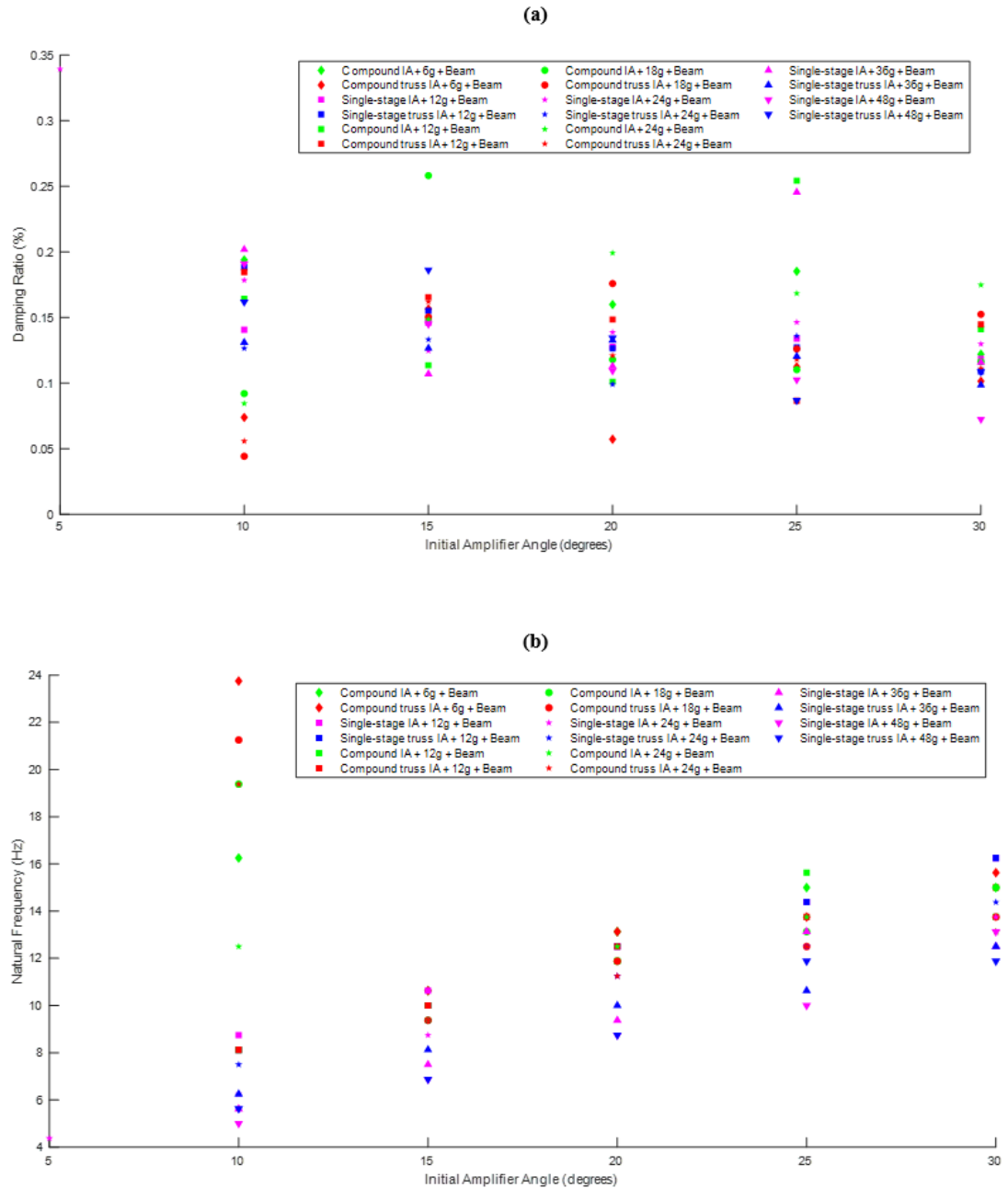


Figure 71: A graph to show a) the damping ratio characteristics, and b) the natural frequency characteristics for each IA when coupled to a cantilever beam, corresponding to different initial amplifier angles and varying quantities of proof mass added to the specified joints of each mechanism.

Furthermore, the findings presented in Table 13 which can be found in the Appendix, Section 8 - Sub-Section 8.2, demonstrate that when each IA is coupled to a cantilever beam, with proof mass added to the tip of the cantilever, the natural frequency peak shifts to a lower region, when compared to the natural frequency of the standard cantilever beam. As the quantity of proof mass increases from 0g to 48g in increments of 12g, the natural frequency of the system deviates further away from the natural frequency of the standalone cantilever. The most

significant alteration of the natural frequency is recorded at 8.75Hz, which is given by the single-stage truss IA with an initial amplifier angle of 5 degrees, when 48g of proof mass is added to the tip of the cantilever.

Additionally, the data presented in Table 14 of the Appendix, Section 8 - Sub-Section 8.2, shows that when each IA is coupled to a cantilever beam with proof mass added to each specified joint of the mechanism, the natural frequency peak shifts to an even lower frequency region, when compared to each configuration where proof mass is located at the tip of the cantilever of each system. As the quantity of proof mass added to the joints of each IA increases from 0g to 24g for the compound and compound truss IAs, and 0g to 48g for the single-stage and single-stage truss IAs, the natural frequency of the system deviates further away from the natural frequency of the standalone cantilever. The most significant alteration of the natural frequency is recorded at 5.00Hz, which is given by the single-stage IA with an initial amplifier angle of 10 degrees, when 48g of proof mass is added to the specified joints of the mechanism.

Among all experimental tests conducted, the addition of proof mass to the joints of each IA exerts the most significant impact on the natural frequency of the cantilever beam. The most significant deviations in damping ratio and Q-factor characteristics from the value of the cantilever beam are recorded to be 0.50% and 1.00%, respectively, when the compound truss IA is coupled to the cantilever beam with an initial amplifier angle of 15 degrees, and 0g of proof mass is added to the system. However, as mentioned previously, the trend in damping ratio and therefore Q-factor, due the inverse proportionality between these dynamic characteristics, is unexpected. This unusual trend may stem from the damping present within the joints of each IA, which is possibly being amplified along with the mass.

Overall, based on the natural frequency and effective mass modifications, the single-stage IA is shown to be the most effective IA, followed by the single-stage truss, compound, and compound truss IAs.

6.1 Limitations

The current work is subject to a significant limitation that warrants consideration. During experimental testing, certain initial amplifier angles are not measurable for the compound, compound truss, nested, and nested truss IAs. The lowest measurable initial amplifier angle for the compound and compound truss IAs is 10 degrees, and for the nested and nested truss

IAs it is 25 degrees. The root cause of this limitation is attributed to the dimensions, more specifically the width, of the inner arms of the aforementioned IAs. The inner arms form the internal mechanisms of the IAs, and they prevent certain initial amplifier angles from being measured due to the presence of interference. This is a crucial limitation, since the findings in this work show that more effective inertia is generated for smaller initial amplifier angles of each IA. Consequently, it is not possible to fully comprehend the behaviour of the compound, compound truss, nested, and nested truss IAs for smaller initial amplifier angles.

In the current study, the dimensions of the arms are based on the size of the commercial 694ZZ bearings. For smaller initial amplifier angles to be attained, the width of the inner arms of each IA, and thus the size of the bearings, must be reduced.

6.2 Future Work

To further the work presented in this thesis, there are several areas that could be improved and expanded upon. Firstly, the width of the arms of each IA could be resized, to allow small initial amplifier angles to be measurable, particularly for the compound, compound truss, nested, and nested truss IAs. The dimensions of the arms could be resized based on smaller bearings, such as the 683ZZ deep groove ball bearings with dimensions of 3mmx7mmx3mm. By doing so, the distance to the point of intersection of the arms would increase, which in turn, would enable smaller measurable initial amplifier angles to be achieved. This would facilitate a more accurate and reliable evaluation of the performance of each IA.

Secondly, the experimental testing approach could be refined. Non-linear tests could be conducted on each IA, to provide a comprehensive understanding of the full non-linear behaviour of each mechanism. Furthermore, multiple modes of vibration could be studied, to assess the performance of each IA across a range of resonances. Additionally, each IA could be coupled to a different dynamic system, this would provide a means to evaluate the reliability and robustness of each individual IA. By evaluating the performance of each IA under various scenarios, it would be possible to identify potential weaknesses or failure modes and develop appropriate mitigation strategies.

Thirdly, the analytical models could be improved. The models are currently derived based on several assumptions, which assume the mass of the components to be negligible, except for the proof mass located at each specified joint of the mechanisms, and the arms to move frictionlessly around each pin joint. Removing these assumptions from the analytical models

would allow for the development of more accurate mathematical models, leading to a more precise prediction of the behaviour of each IA. To aid in the creation of these models, simulations could be carried out, and these simulations could additionally facilitate an investigation into the complete nonlinear behaviour displayed by each IA.

7. Conclusion

In this work six novel IA mechanisms are developed. Each IA is analytically analysed, designed, physically realised, and experimentally tested.

The Lagrangian equation is utilised to derive the equations of motion for the single-stage, compound, and nested IAs. It should be noted that the resulting dynamic equations are identical amongst corresponding mechanisms, for example, the single-stage and the single-stage truss IAs. The equations of motion reveal that the behaviour of each IA can be altered by manipulating the geometrical characteristics of the respective mechanism, particularly the initial amplifier angle. Thus, during experimental testing, the initial amplifier angle is selected as the parameter to be tuned. Additionally, the analysis in Section 3 shows that each IA becomes highly non-linear as small initial amplifier angles are approached. Note that small initial amplifier angles are required for high inertial amplification factors.

Subsequent to the analytical analysis, the design of each IA is undertaken. The design process utilises the modelling software Solidworks, to create all constituent component parts for each IA, and to simulate the assemblies of these parts. This procedure guarantees the functionality of each IA upon physical realisation. Following the design process, the designed components are additively manufactured, and any required commercial components are procured. Once all component parts for each IA are acquired, the parts are assembled to bring each IA to fruition.

Each IA is then experimentally tested. Two sets of electrodynamic shaker tests are conducted. The experimental results show that the single-stage, single-stage truss, compound, and compound truss IAs all have the ability to enhance the effective mass characteristics of the cantilever beam, thereby causing changes to its the underlying natural frequency, damping ratio, and Q-factor properties. A trend among the experimental data is shown, in which a reduction in the initial amplifier angle of each IA results in an increase in the effective mass of the system. This, in turn, influences the natural frequency of each system to decrease.

Furthermore, the results demonstrate that when each IA is coupled to a cantilever beam, with proof mass added to the tip of the cantilever, the natural frequency peak shifts to a lower region, when compared to the natural frequency of the standalone cantilever beam. As the quantity of proof mass increases from 0g to 48g in increments of 12g, the natural frequency of the system deviates further away from the natural frequency of the standalone cantilever. When proof mass is affixed to specific joints of each IA, the first natural frequency peak of the system shifts to an even lower region, compared to each system with proof mass applied to the tip of the cantilever, and the bare beam. As the quantity of proof mass added to the joints of each IA increases from 0g to 24g for the compound and compound truss IAs, and 0g to 48g for the single-stage and single-stage truss IAs, the natural frequency of the system deviates further away from the natural frequency of the cantilever. As a result, this work shows that the incorporation of proof mass at the joints of each individual IA, has the most significant impact on the natural frequency of the cantilever beam. Based on the natural frequency and effective mass modifications, the single-stage IA is concluded to be the most effective IA, followed by the single-stage truss, compound, and compound truss IAs.

It is expected that as the effective mass of each IA increases for decreasing initial amplifier angles, the damping ratio and Q-factor for each system would decrease and increase, respectively. However, the experimental data for each test shows that as the initial amplifier angle of each IA decreases, the damping ratio increases and the Q-factor decreases, for each respective system. This is an unexpected trend, which is attributed to the amplification effects of each IA. It appears that when the effective mass of each IA is amplified, the effective damping of the system is also amplified. A similar phenomenon is exhibited by the inerter.

In conclusion, the findings presented in this thesis offer significant contributions towards the comprehension of IAs, in terms of both behaviour and performance. The outcomes can be used to inform future research and the development of IA mechanisms, ultimately leading to notable advancements in their efficacy. This, in turn, will further develop applications which require dynamic tuning like atomic force microscopy and vibration-based energy harvesting.

8. Appendix

8.1 Equations

Compound IA

The vertical distance between joint e) and joint b) of the compound IA is related by

$$\bar{z}_e = z_e - z_b \quad 121$$

The mass at joint e) of the compound IA moves vertically as z_e and horizontally as x_e which is related to \bar{z}_e and x_b by

$$l_2^2 = \left(\frac{w_1}{2} - x_b\right)^2 + \left(\frac{h_2}{2} + \bar{z}_e\right)^2 \quad 122$$

By rearranging equation (122) in terms of \bar{z}_e the equation becomes

$$\bar{z}_e = \sqrt{l_2^2 - \left(\frac{w_1}{2} - x_b\right)^2} - \frac{h_2}{2} \quad 123$$

To obtain the equation for the vertical displacement of joint e) equation 123 can be substituted into equation 121.

The vertical distance between joint f) and joint b) of the compound IA is related by

$$\bar{z}_f = z_f - z_b = -\bar{z}_e \quad 124$$

The mass at joint f) of the compound IA moves vertically as z_f and horizontally as x_f which is related to \bar{z}_f and x_b by

$$l_2^2 = \left(\frac{w_1}{2} - x_b\right)^2 + \left(\frac{h_2}{2} - \bar{z}_f\right)^2 \quad 125$$

By rearranging equation (125) in terms of \bar{z}_f the equation follows as

$$\bar{z}_f = \frac{h_2}{2} - \sqrt{l_2^2 - \left(\frac{w_1}{2} - x_b\right)^2} \quad 126$$

To obtain the equation for the vertical displacement of joint f) equation 126 can be substituted into equation 124.

Below are the derivatives required to satisfy equation 58 in Section 3.2, sub-section 3.2.2.

$$\frac{\partial x_e}{\partial z} = \frac{\partial x_f}{\partial z} = \frac{1}{4} \frac{\frac{h_1}{2} + \frac{z}{2}}{\sqrt{l_1^2 - \left(\frac{h_1}{2} + \frac{z}{2}\right)^2}} \quad 127$$

$$\frac{\partial^2 x_e}{\partial z^2} = \frac{\partial^2 x_f}{\partial z^2} = \frac{1}{8\sqrt{l_1^2 - \left(\frac{h_1}{2} + \frac{z}{2}\right)^2}} + \frac{\left(\frac{h_1}{2} + \frac{z}{2}\right)^2}{8\left(l_1^2 - \left(\frac{h_1}{2} + \frac{z}{2}\right)^2\right)^{3/2}} \quad 128$$

$$\frac{\partial z_e}{\partial z} = \frac{\left(\sqrt{l_1^2 - \left(\frac{h_1}{2} + \frac{z}{2}\right)^2} - \frac{w_1}{2}\right)\left(\frac{h_1}{2} + \frac{z}{2}\right)}{2\sqrt{l_2^2 - \left(\sqrt{l_1^2 - \left(\frac{h_1}{2} + \frac{z}{2}\right)^2} - \frac{w_1}{2}\right)^2} \sqrt{l_1^2 - \left(\frac{h_1}{2} + \frac{z}{2}\right)^2}} + \frac{1}{2} \quad 129$$

$$\begin{aligned} \frac{\partial^2 z_e}{\partial z^2} = & \frac{\sqrt{l_1^2 - \left(\frac{h_1}{2} + \frac{z}{2}\right)^2} - \frac{w_1}{2}}{4\sqrt{l_2^2 - \left(\sqrt{l_1^2 - \left(\frac{h_1}{2} + \frac{z}{2}\right)^2} - \frac{w_1}{2}\right)^2} \sqrt{l_1^2 - \left(\frac{h_1}{2} + \frac{z}{2}\right)^2}} + \\ & \frac{\left(\sqrt{l_1^2 - \left(\frac{h_1}{2} + \frac{z}{2}\right)^2} - \frac{w_1}{2}\right)\left(\frac{h_1}{2} + \frac{z}{2}\right)^2}{4\sqrt{l_2^2 - \left(\sqrt{l_1^2 - \left(\frac{h_1}{2} + \frac{z}{2}\right)^2} - \frac{w_1}{2}\right)^2} \left(l_1^2 - \left(\frac{h_1}{2} + \frac{z}{2}\right)^2\right)^{3/2}} - \\ & \frac{\left(\frac{h_1}{2} + \frac{z}{2}\right)^2}{4\sqrt{l_2^2 - \left(\sqrt{l_1^2 - \left(\frac{h_1}{2} + \frac{z}{2}\right)^2} - \frac{w_1}{2}\right)^2} \left(l_1^2 - \left(\frac{h_1}{2} + \frac{z}{2}\right)^2\right)} - \frac{\left(\sqrt{l_1^2 - \left(\frac{h_1}{2} + \frac{z}{2}\right)^2} - \frac{w_1}{2}\right)^2 \left(\frac{h_1}{2} + \frac{z}{2}\right)^2}{4\left(l_2^2 - \left(\sqrt{l_1^2 - \left(\frac{h_1}{2} + \frac{z}{2}\right)^2} - \frac{w_1}{2}\right)^2\right)^{3/2} \left(l_1^2 - \left(\frac{h_1}{2} + \frac{z}{2}\right)^2\right)} \quad 130 \end{aligned}$$

$$\frac{\partial z_f}{\partial z} = \frac{\left(\frac{w_1}{2} - \sqrt{l_1^2 - \left(\frac{h_1}{2} + \frac{z}{2}\right)^2}\right)\left(\frac{h_1}{2} + \frac{z}{2}\right)}{2\sqrt{l_2^2 - \left(\frac{w_1}{2} - \sqrt{l_1^2 - \left(\frac{h_1}{2} + \frac{z}{2}\right)^2}\right)^2} \sqrt{l_1^2 - \left(\frac{h_1}{2} + \frac{z}{2}\right)^2}} + \frac{1}{2} \quad 131$$

$$\begin{aligned}
\frac{\partial^2 z_f}{\partial z^2} &= \frac{\left(\frac{h_1+z}{2}\right)^2}{4\sqrt{l_2^2 - \left(\sqrt{l_1^2 - \left(\frac{h_1+z}{2}\right)^2} - \frac{w_1}{2}\right)^2} \left(l_1^2 - \left(\frac{h_1+z}{2}\right)^2\right)} + \\
&\quad \frac{\left(\sqrt{l_1^2 - \left(\frac{h_1+z}{2}\right)^2} - \frac{w_1}{2}\right)^2 \left(\frac{h_1+z}{2}\right)^2}{4\left(l_2^2 - \left(\sqrt{l_1^2 - \left(\frac{h_1+z}{2}\right)^2} - \frac{w_1}{2}\right)^2\right)^{3/2} \left(l_1^2 - \left(\frac{h_1+z}{2}\right)^2\right)} \\
&\quad - \frac{\frac{\sqrt{l_1^2 - \left(\frac{h_1+z}{2}\right)^2} - \frac{w_1}{2}}{4\sqrt{l_2^2 - \left(\sqrt{l_1^2 - \left(\frac{h_1+z}{2}\right)^2} - \frac{w_1}{2}\right)^2} \sqrt{l_1^2 - \left(\frac{h_1+z}{2}\right)^2}}}{4\sqrt{l_2^2 - \left(\sqrt{l_1^2 - \left(\frac{h_1+z}{2}\right)^2} - \frac{w_1}{2}\right)^2} \left(l_1^2 - \left(\frac{h_1+z}{2}\right)^2\right)^{3/2}} - \frac{\left(\sqrt{l_1^2 - \left(\frac{h_1+z}{2}\right)^2} - \frac{w_1}{2}\right)\left(\frac{h_1+z}{2}\right)^2}{4\sqrt{l_2^2 - \left(\sqrt{l_1^2 - \left(\frac{h_1+z}{2}\right)^2} - \frac{w_1}{2}\right)^2} \left(l_1^2 - \left(\frac{h_1+z}{2}\right)^2\right)^{3/2}}
\end{aligned} \tag{132}$$

It is also useful to have

$$\frac{\partial x_e}{\partial z} \cdot \frac{\partial x_e}{\partial z} = \frac{\partial x_f}{\partial z} \cdot \frac{\partial x_f}{\partial z} = -\frac{\left(\frac{h_1+z}{2}\right)^2}{16\left(\left(\frac{h_1+z}{2}\right)^2 - l_1^2\right)} \tag{133}$$

$$\frac{\partial x_e}{\partial z} \cdot \frac{\partial^2 x_e}{\partial z^2} = \frac{\partial x_f}{\partial z} \cdot \frac{\partial^2 x_f}{\partial z^2} = \frac{\left(\frac{h_1+z}{2}\right)^3}{32\left(\left(\frac{h_1+z}{2}\right)^2 - l_1^2\right)^2} - \frac{\frac{h_1+z}{2}}{32\left(\left(\frac{h_1+z}{2}\right)^2 - l_1^2\right)} \tag{134}$$

$$\frac{\partial z_e}{\partial z} \cdot \frac{\partial z_e}{\partial z} = \left(\frac{\left(\sqrt{l_1^2 - \left(\frac{h_1+z}{2}\right)^2} - \frac{w_1}{2}\right)\left(\frac{h_1+z}{2}\right)}{2\sqrt{l_2^2 - \left(\sqrt{l_1^2 - \left(\frac{h_1+z}{2}\right)^2} - \frac{w_1}{2}\right)^2} \sqrt{l_1^2 - \left(\frac{h_1+z}{2}\right)^2}} + \frac{1}{2} \right)^2 \tag{135}$$

$$\frac{\partial z_e}{\partial z} \cdot \frac{\partial^2 z_e}{\partial z^2} = \left(\frac{\left(\sqrt{l_1^2 - \left(\frac{h_1+z}{2}\right)^2} - \frac{w_1}{2} \right) \left(\frac{h_1+z}{2}\right)}{2 \sqrt{l_2^2 - \left(\sqrt{l_1^2 - \left(\frac{h_1+z}{2}\right)^2} - \frac{w_1}{2} \right)^2} \sqrt{l_1^2 - \left(\frac{h_1+z}{2}\right)^2}} + \frac{1}{2} \right) \cdot$$

$$\left(\frac{\sqrt{l_1^2 - \left(\frac{h_1+z}{2}\right)^2} - \frac{w_1}{2}}{4 \sqrt{l_2^2 - \left(\sqrt{l_1^2 - \left(\frac{h_1+z}{2}\right)^2} - \frac{w_1}{2} \right)^2} \sqrt{l_1^2 - \left(\frac{h_1+z}{2}\right)^2}} + \right.$$

$$\frac{\left(\sqrt{l_1^2 - \left(\frac{h_1+z}{2}\right)^2} - \frac{w_1}{2} \right) \left(\frac{h_1+z}{2}\right)^2}{4 \sqrt{l_2^2 - \left(\sqrt{l_1^2 - \left(\frac{h_1+z}{2}\right)^2} - \frac{w_1}{2} \right)^2} \left(l_1^2 - \left(\frac{h_1+z}{2}\right)^2 \right)^{3/2}} - \frac{\left(\frac{h_1+z}{2}\right)^2}{4 \sqrt{l_2^2 - \left(\sqrt{l_1^2 - \left(\frac{h_1+z}{2}\right)^2} - \frac{w_1}{2} \right)^2} \left(l_1^2 - \left(\frac{h_1+z}{2}\right)^2 \right)} -$$

$$\left. \frac{\left(\sqrt{l_1^2 - \left(\frac{h_1+z}{2}\right)^2} - \frac{w_1}{2} \right)^2 \left(\frac{h_1+z}{2}\right)^2}{4 \left(l_2^2 - \left(\sqrt{l_1^2 - \left(\frac{h_1+z}{2}\right)^2} - \frac{w_1}{2} \right)^2 \right)^{3/2} \left(l_1^2 - \left(\frac{h_1+z}{2}\right)^2 \right)} \right)$$

136

$$\frac{\partial z_f}{\partial z} \cdot \frac{\partial z_f}{\partial z} = \left(\frac{\left(\frac{w_1}{2} - \sqrt{l_1^2 - \left(\frac{h_1+z}{2}\right)^2} \right) \left(\frac{h_1+z}{2}\right)}{2 \sqrt{l_2^2 - \left(\frac{w_1}{2} - \sqrt{l_1^2 - \left(\frac{h_1+z}{2}\right)^2} \right)^2} \sqrt{l_1^2 - \left(\frac{h_1+z}{2}\right)^2}} + \frac{1}{2} \right)^2$$

137

$$\frac{\partial z_f}{\partial z} \cdot \frac{\partial^2 z_f}{\partial z^2} = \left(\frac{\left(\frac{w_1}{2} - \sqrt{l_1^2 - \left(\frac{h_1+z}{2}\right)^2} \right) \left(\frac{h_1+z}{2}\right)}{2 \sqrt{l_2^2 - \left(\frac{w_1}{2} - \sqrt{l_1^2 - \left(\frac{h_1+z}{2}\right)^2} \right)^2} \sqrt{l_1^2 - \left(\frac{h_1+z}{2}\right)^2}} + \frac{1}{2} \right) \cdot$$

$$\left(\frac{\left(\frac{h_1+z}{2}\right)^2}{4 \sqrt{l_2^2 - \left(\sqrt{l_1^2 - \left(\frac{h_1+z}{2}\right)^2} - \frac{w_1}{2} \right)^2} \left(l_1^2 - \left(\frac{h_1+z}{2}\right)^2 \right)} + \right.$$

138

$$\frac{\left(\sqrt{l_1^2 - \left(\frac{h_1+z}{2}\right)^2} - \frac{w_1}{2}\right)^2 \left(\frac{h_1+z}{2}\right)^2}{4\left(l_2^2 - \left(\sqrt{l_1^2 - \left(\frac{h_1+z}{2}\right)^2} - \frac{w_1}{2}\right)^2\right)^{3/2} \left(l_1^2 - \left(\frac{h_1+z}{2}\right)^2\right)} - \frac{\sqrt{l_1^2 - \left(\frac{h_1+z}{2}\right)^2} - \frac{w_1}{2}}{4\sqrt{l_2^2 - \left(\sqrt{l_1^2 - \left(\frac{h_1+z}{2}\right)^2} - \frac{w_1}{2}\right)^2} \sqrt{l_1^2 - \left(\frac{h_1+z}{2}\right)^2}} - \left(\frac{\left(\sqrt{l_1^2 - \left(\frac{h_1+z}{2}\right)^2} - \frac{w_1}{2}\right)\left(\frac{h_1+z}{2}\right)^2}{4\sqrt{l_2^2 - \left(\sqrt{l_1^2 - \left(\frac{h_1+z}{2}\right)^2} - \frac{w_1}{2}\right)^2} \left(l_1^2 - \left(\frac{h_1+z}{2}\right)^2\right)^{3/2}}\right)$$

Nested IA

The vertical distance between joint g) and joint b) of the nested IA is given by

$$\bar{z}_g = z_g - z_b \quad 139$$

Joint g moves vertically as z_g and horizontally as x_g which is related to \bar{z}_g and x_b by

$$l_2^2 = (w_1 - x_b)^2 + \left(\frac{h_2}{2} + \bar{z}_g\right)^2 \quad 140$$

By rearranging equation (140) in terms of \bar{z}_g the equation follows as

$$\bar{z}_g = \sqrt{l_2^2 - (w_1 - x_b)^2} - \frac{h_2}{2} \quad 141$$

To obtain the equation for the vertical displacement of joint g) equation 141 can be substituted into equation 139.

The vertical distance between joint j) and joint b) of the nested IA is related by

$$\bar{z}_j = z_j - z_b = -\bar{z}_g \quad 142$$

Joint j) moves vertically as z_j and horizontally as x_j which is related to \bar{z}_j and x_b by

$$l_2^2 = (w_1 - x_b)^2 + \left(\frac{h_2}{2} - \bar{z}_j\right)^2 \quad 143$$

By rearranging equation (143) in terms of \bar{z}_j the equation follows as

$$\bar{z}_j = \frac{h_2}{2} - \sqrt{l_2^2 - (w_1 - x_b)^2} \quad 144$$

To obtain the equation for the vertical displacement of joint j) equation 144 can be substituted into equation 142.

Below are the derivatives required to satisfy equation 80 in Section 3.2, sub-section 3.3.2.

$$\frac{\partial x_i}{\partial z} = \frac{\frac{h_1}{2} + \frac{z}{2}}{2\sqrt{l_1^2 - \left(\frac{h_1}{2} + \frac{z}{2}\right)^2 - l_2^2 + l_3^2}} \quad 145$$

$$\frac{\partial^2 x_i}{\partial z^2} = \frac{\left(\frac{h_1}{2} + \frac{z}{2}\right)^2}{4\left(l_1^2 - \left(\frac{h_1}{2} + \frac{z}{2}\right)^2 - l_2^2 + l_3^2\right)^{3/2}} + \frac{1}{4\sqrt{l_1^2 - \left(\frac{h_1}{2} + \frac{z}{2}\right)^2 - l_2^2 + l_3^2}} \quad 146$$

$$\frac{\partial z_i}{\partial z} = \frac{1}{2} \quad 147$$

$$\frac{\partial^2 z_i}{\partial z^2} = 0 \quad 148$$

It is also useful to have

$$\frac{\partial x_i}{\partial z} \cdot \frac{\partial x_i}{\partial z} = -\frac{\left(\frac{h_1}{2} + \frac{z}{2}\right)^2}{4\left(\left(\frac{h_1}{2} + \frac{z}{2}\right)^2 - l_1^2 + l_2^2 - l_3^2\right)} \quad 149$$

$$\frac{\partial x_i}{\partial z} \cdot \frac{\partial^2 x_i}{\partial z^2} = \frac{(l_3^2 - l_2^2 + l_1^2)(z + h_1)}{(4(l_3^2 - l_2^2 + l_1^2) - (z + h_1)^2)^2} \quad 150$$

$$\frac{\partial z_i}{\partial z} \cdot \frac{\partial z_i}{\partial z} = \frac{1}{4} \quad 151$$

$$\frac{\partial z_i}{\partial z} \cdot \frac{\partial^2 z_i}{\partial z^2} = 0 \quad 152$$

8.2 Natural frequency, damping ratio, and Q-factor characteristics for each system shown in Subsections 5.2.1 and 5.2.3.

Table 13: A table to show the natural frequencies, damping ratios and Q-factor values for each IA coupled to a cantilever beam, corresponding to different initial amplifier angles for each IA and varying quantities of proof mass added to the tip of the cantilever. It is worth noting that the data for the cantilever beam is included for comparative analysis.

	0g Tip Mass			12g Tip Mass			24g Tip Mass			36g Tip Mass			48g Tip Mass		
	ω_1 (Hz)	ξ (%)	Q (%)	ω_1 (Hz)	ξ (%)	Q (%)	ω_1 (Hz)	ξ (%)	Q (%)	ω_1 (Hz)	ξ (%)	Q (%)	ω_1 (Hz)	ξ (%)	Q (%)
Cantilever Beam	26.25	0.11	4.71	22.50	0.11	4.61	20.00	0.11	4.38	18.13	0.09	5.51	16.25	0.14	3.53
Single-Stage IA + Beam	/	/	/	/	/	/	/	/	/	/	/	/	/	/	/
Single-Stage Truss IA + Beam	/	/	/	/	/	/	/	/	/	15.63	0.29	1.74	8.75	0.16	3.11
Compound IA + Beam	/	/	/	/	/	/	/	/	/	/	/	/	/	/	/
Compound Truss IA + Beam	/	/	/	/	/	/	/	/	/	/	/	/	/	/	/
Single-Stage IA + Beam	10.63	0.16	3.17	13.13	0.14	3.60	12.50	0.19	2.63	11.88	0.15	3.30	11.25	0.11	4.46
Single-Stage Truss IA + Beam	12.50	0.13	3.96	13.75	0.11	4.67	13.13	0.12	4.09	11.88	0.11	4.38	11.25	0.13	3.78
Compound IA + Beam	/	/	/	16.88	0.22	2.25	9.38	0.17	2.95	8.75	0.18	2.73	14.38	0.22	2.25
Compound Truss IA + Beam	/	/	/	/	/	/	/	/	/	/	/	/	/	/	/
Single-Stage IA + Beam	16.25	0.10	4.85	15.63	0.12	4.06	14.38	0.13	3.97	13.75	0.13	3.88	12.50	0.12	4.02
Single-Stage Truss IA + Beam	16.25	0.10	4.85	16.25	0.10	4.88	15.00	0.12	4.29	13.13	0.12	4.31	12.50	0.13	3.80
Compound IA + Beam	12.50	0.12	4.28	11.25	0.13	3.81	11.25	0.13	3.87	10.63	0.12	4.23	11.88	0.13	3.85
Compound Truss IA + Beam	11.88	0.50	1.00	11.25	0.13	3.87	11.25	0.10	4.96	10.63	0.12	4.12	10.00	0.16	3.13
Single-Stage IA + Beam	17.50	0.09	5.30	16.88	0.12	4.22	15.00	0.11	4.68	15.00	0.11	4.75	13.75	0.12	4.34
Single-Stage Truss IA + Beam	18.13	0.09	5.49	16.88	0.11	4.73	15.63	0.10	4.84	14.38	0.12	4.05	13.13	0.11	4.42
Compound IA + Beam	14.38	0.13	3.99	13.75	0.11	4.56	13.13	0.10	4.88	11.88	0.21	2.35	12.50	0.09	5.49
Compound Truss IA + Beam	15.00	0.10	5.00	13.75	0.12	4.26	11.88	0.14	3.55	11.88	0.12	4.15	11.88	0.13	3.78
Single-Stage IA + Beam	19.38	0.09	5.70	17.50	0.11	4.49	16.25	0.12	4.00	15.00	0.10	4.96	13.75	0.14	3.50
Single-Stage Truss IA + Beam	20.00	0.10	5.26	17.50	0.11	4.49	16.25	0.12	4.04	15.00	0.10	5.05	13.75	0.13	4.00
Compound IA + Beam	16.25	0.12	4.01	15.00	0.11	4.69	13.75	0.09	5.65	13.75	0.11	4.73	12.50	0.10	4.81
Compound Truss IA + Beam	16.25	0.10	4.77	14.38	0.13	3.84	13.75	0.12	4.02	13.13	0.14	3.64	12.50	0.11	4.70
Single-Stage IA + Beam	20.63	0.08	6.65	18.13	0.09	5.53	16.88	0.11	4.64	15.63	0.10	5.03	13.75	0.11	4.42
Single-Stage Truss IA + Beam	20.63	0.09	5.29	18.13	0.08	6.36	16.25	0.13	3.98	15.00	0.13	3.88	14.38	0.12	4.11
Compound IA + Beam	17.50	0.12	4.07	15.63	0.11	4.54	16.25	0.18	2.86	14.38	0.10	5.05	13.75	0.11	4.73
Compound Truss IA + Beam	16.88	0.12	4.25	15.00	0.11	4.41	14.38	0.12	4.25	13.13	0.13	3.73	13.13	0.12	4.18

Table 14: A table to show a comprehensive breakdown of the natural frequencies, damping ratios, and Q-factor values for each IA coupled to a cantilever beam. The table is arranged according to the initial amplifier angles measured for each IA and the varying quantities of proof mass added to each specified joint of the IA. It is worth noting that the data for the cantilever beam is included for comparative analysis.

	0g Joint Mass			6g Joint Mass			12g Joint Mass			18g Joint Mass			24g Joint Mass			36g Joint Mass			48g Joint Mass			
	ω_1 (Hz)	ξ (%)	Q (%)	ω_1 (Hz)	ξ (%)	Q (%)	ω_1 (Hz)	ξ (%)	Q (%)	ω_1 (Hz)	ξ (%)	Q (%)	ω_1 (Hz)	ξ (%)	Q (%)	ω_1 (Hz)	ξ (%)	Q (%)	ω_1 (Hz)	ξ (%)	Q (%)	
Cantilever Beam	26.25	0.11	4.71	/	/	/	22.50	0.11	4.61	/	/	/	20.00	0.11	4.38	18.13	0.09	5.51	16.25	0.14	3.53	
Single-Stage IA + Beam	/	/	/	/	/	/	/	/	/	/	/	/	4.38	0.34	1.47	/	/	/	/	/	/	/
Single-Stage Truss IA + Beam	/	/	/	/	/	/	/	/	/	/	/	/	/	/	/	/	/	/	/	/	/	/
Compound IA + Beam	/	/	/	/	/	/	/	/	/	/	/	/	/	/	/	/	/	/	/	/	/	/
Compound Truss IA + Beam	/	/	/	/	/	/	/	/	/	/	/	/	/	/	/	/	/	/	/	/	/	/
$\phi_i = 5$ degrees	Single-Stage IA + Beam	10.63	0.16	3.17	/	/	8.75	0.14	3.56	/	/	/	6.25	0.18	2.80	5.63	0.20	2.48	5.00	0.19	2.62	
	Single-Stage Truss IA + Beam	12.50	0.13	3.96	/	/	8.13	0.19	2.66	/	/	/	7.50	0.13	3.95	6.25	0.13	3.82	5.63	0.16	3.09	
	Compound IA + Beam	/	/	/	16.25	0.19	2.58	8.13	0.16	3.04	19.38	0.09	5.43	12.50	0.08	5.92	/	/	/	/	/	/
	Compound Truss IA + Beam	/	/	/	23.75	0.07	6.77	8.13	0.18	2.71	21.25	0.04	11.30	19.38	0.06	8.97	/	/	/	/	/	/
$\phi_i = 10$ degrees	Single-Stage IA + Beam	16.25	0.10	4.85	/	/	10.63	0.15	3.43	/	/	/	8.75	0.12	4.01	7.50	0.11	4.68	6.88	0.14	3.45	
	Single-Stage Truss IA + Beam	16.25	0.10	4.85	/	/	10.00	0.16	3.23	/	/	/	9.38	0.13	3.75	8.13	0.13	3.95	6.88	0.19	2.69	
	Compound IA + Beam	12.50	0.12	4.28	10.63	0.15	3.37	10.00	0.11	4.41	9.38	0.26	1.94	9.38	0.15	3.37	/	/	/	/	/	/
	Compound Truss IA + Beam	11.88	0.50	1.00	10.63	0.16	3.19	10.00	0.17	3.02	9.38	0.15	3.32	9.38	0.16	3.08	/	/	/	/	/	/
$\phi_i = 15$ degrees	Single-Stage IA + Beam	17.50	0.09	5.30	/	/	12.50	0.13	3.92	/	/	/	11.25	0.14	3.60	9.38	0.11	4.43	8.75	0.11	4.57	
	Single-Stage Truss IA + Beam	18.13	0.09	5.49	/	/	12.50	0.13	3.96	/	/	/	11.25	0.10	5.04	10.00	0.13	3.77	8.75	0.13	3.72	
	Compound IA + Beam	14.38	0.13	3.99	13.13	0.16	3.13	11.88	0.10	4.95	11.88	0.12	4.24	12.50	0.20	2.51	/	/	/	/	/	/
	Compound Truss IA + Beam	15.00	0.10	5.00	13.13	0.06	8.75	12.50	0.15	3.37	11.88	0.18	2.84	11.25	0.12	4.14	/	/	/	/	/	/
$\phi_i = 20$ degrees	Single-Stage IA + Beam	19.38	0.09	5.70	/	/	14.38	0.13	3.74	/	/	/	12.50	0.15	3.42	13.13	0.25	2.04	10.00	0.10	4.88	
	Single-Stage Truss IA + Beam	20.00	0.10	5.26	/	/	14.38	0.13	3.93	/	/	/	12.50	0.14	3.68	10.63	0.12	4.15	11.88	0.09	5.77	
	Compound IA + Beam	16.25	0.12	4.01	15.00	0.19	2.70	15.63	0.25	1.97	13.13	0.11	4.54	13.75	0.17	2.97	/	/	/	/	/	/
	Compound Truss IA + Beam	16.25	0.10	4.77	13.75	0.11	4.45	13.75	0.09	5.78	12.50	0.13	3.97	12.50	0.12	4.24	/	/	/	/	/	/
$\phi_i = 25$ degrees	Single-Stage IA + Beam	20.63	0.08	6.65	/	/	16.25	0.12	4.22	/	/	/	13.75	0.13	3.85	12.50	0.12	4.32	13.13	0.07	6.91	
	Single-Stage Truss IA + Beam	20.63	0.09	5.29	/	/	16.25	0.11	4.59	/	/	/	14.38	0.11	4.54	12.50	0.10	5.08	11.88	0.11	4.60	
	Compound IA + Beam	17.50	0.12	4.07	15.00	0.12	4.10	13.75	0.14	3.54	15.00	0.12	4.30	13.13	0.17	2.86	/	/	/	/	/	
	Compound Truss IA + Beam	16.88	0.12	4.25	15.63	0.10	4.93	15.00	0.14	3.46	13.75	0.15	3.28	13.13	0.11	4.50	/	/	/	/	/	/

9. Bibliography

1. Piersol A, Paez T. Harris' Shock and Vibration Handbook. McGraw-Hill; 2009.
2. Frahm H. Device for Damping Vibrations of Bodies. 1911 Apr. 18.
3. Watts P. On a method of reducing the rolling of ships at sea. Transactions of the Royal Institution of Naval Architects: 1883-12. 1883 Mar 16.
4. Wagg DJ. A review of the mechanical inerter: historical context, physical realisations and nonlinear applications. Nonlinear Dynamics. 2021 Mar 1.
5. Yang F, Sedaghati R, Esmailzadeh E. Vibration suppression of structures using tuned mass damper technology: A state-of-the-art review. Journal of Vibration and Control. 2022 Apr 1;28(7–8):812–36.
6. Ormondroyd J, Den Hartog JP. The theory of the dynamic vibration absorber. The American Society of Mechanical Engineers, Journal of Applied Mechanics 50(7): 9–22. 1928.
7. Den Hartog JP. Mechanical Vibrations. 2nd edition. London: McGraw-Hill; 1940.
8. Brock JE. A Note on the Damped Vibration Absorber. The American Society of Mechanical Engineers, Journal of Applied Mechanics. 1946;13(4): A284–A284.
9. Den Hartog JP. Mechanical Vibrations. 4th edition. New York: McGraw-Hill; 1956.
10. Thompson AG. Optimum tuning and damping of a dynamic vibration absorber applied to a force excited and damped primary system. Journal of Sound and Vibration. 1981;77(3):403–15.
11. Randall SE, Halsted III DM, Taylor DL. Optimum Vibration Absorbers for Linear Damped Systems. Journal of Mechanical Design. 1981 Oct 1;103(4):908–13.
12. Warburton GB. Optimum absorber parameters for various combinations of response and excitation parameters. Earthquake Engineering & Structural Dynamics. 1982 May 1;10(3):381–401.
13. Warburton GB, Ayorinde EO. Optimum absorber parameters for simple systems. Earthquake Engineering & Structural Dynamics. 1980 Jan 1;8(3):197–217.

14. Tsai HC, Lin GC. Optimum tuned-mass dampers for minimizing steady-state response of support-excited and damped systems. *Earthquake Engineering & Structural Dynamics*. 1993 Nov 1;22(11):957–73.
15. Alhassan MA, Al-Rousan RZ, Al-Khasawneh SI. Control of Vibrations of Common Pedestrian Bridges in Jordan Using Tuned Mass Dampers. *Procedia Manufacturing*. 2020; 44:36–43
16. Pinkaew T, Lukkunaprasit P, Chatupote P. Seismic effectiveness of tuned mass dampers for damage reduction of structures. *Engineering Structures*. 2003;25(1):39–46.
17. Liu J, Li D, Yu P. Study on optimization algorithm of tuned mass damper parameters to reduce vehicle-bridge coupled vibration. *PLoS One*. 2019 Apr 23;14(4): e0215773.
18. Anand S, Kalyan Raj AH, Kartik B, Dhanushkodi DM. Tuned Mass Dampers in Passenger Cars. 2007.
19. Ho W, Wong B, England D. Tuned Mass Damper for Rail Noise Control. *Noise and Vibration Mitigation for Rail Transportation Systems*. Tokyo: Springer Japan; 2012. p. 89–96.
20. Ghassempour M, Failla G, Arena F. Vibration mitigation in offshore wind turbines via tuned mass damper. *Engineering Structures*. 2019; 183:610–36.
21. Jain PC, Mukherjee A, Krishna Y. Tuned mass dampers for flight vehicle components subjected to rocket noise. *Aerospace Science and Technology*. 2011;15(3):175–82.
22. Cinquemani S, Braghin F, Resta F. Semi active tunable mass damper for helicopters. In: *Society of Photo-Optical Instrumentation Engineers Conference Series*. 2017. p. 1016431.
23. Poon DCK, Shieh S song, Joseph LM, Chang CC. Structural Design of Taipei 101, the World's Tallest Building. *Council on Tall Buildings and Urban Habitat; Seoul Conference*. 2004.
24. Tuan AY, Shang GQ. Vibration Control in a 101-Storey Building Using a Tuned Mass Damper. *Journal of Applied Science and Engineering*. 2014;17(2):141–56.
25. Flannelly WG. Dynamic antiresonant vibration isolator. United States patent US 3,322,379. 1967 May 30.

26. Liu N, Li C, Yin C, Dong X, Hua H. Application of a dynamic antiresonant vibration isolator to minimize the vibration transmission in underwater vehicles. *Journal of Vibration and Control*. 2018 Sep 1;24(17):3819–29.
27. Barys M, Zalewski R. Analysis of inertial amplification mechanism with smart spring-damper for attenuation of beam vibrations. In: *MATEC Web of Conferences*. Édition Diffusion Presse Sciences; 2018.
28. Liu C, Chen L, Lee HP, Yang Y, Zhang X. A review of the inerter and inerter-based vibration isolation: Theory, devices, and applications. *Journal of the Franklin Institute*. 2022;359(14):7677–707.
29. Yang J, Jiang JZ, Neild SA. Dynamic analysis and performance evaluation of nonlinear inerter-based vibration isolators. *Nonlinear Dynamics*. 2020;99(3):1823–39.
30. Alujevic N, Cakmak D, Wolf H, Jokic M. An inerter-based active vibration isolation system. In: *MATEC Web of Conferences*. Édition Diffusion Presse Sciences; 2018.
31. Kuhnert WM, Gonçalves PJP, Ledezma-Ramirez DF, Brennan MJ. Inerter-like devices used for vibration isolation: A historical perspective. *Journal of the Franklin Institute*. 2021;358(1):1070–86.
32. Alotta G, Failla G. Improved inerter-based vibration absorbers. *International Journal of Mechanical Sciences*. 2021; 192:106087.
33. Shen Y, Chen L, Yang X, Shi D, Yang J. Improved design of dynamic vibration absorber by using the inerter and its application in vehicle suspension. *Journal of Sound and Vibration*. 2016; 361:148–58.
34. Lazar IF, Neild SA, Wagg DJ. Using an inerter-based device for structural vibration suppression. *Earthquake Engineering & Structural Dynamics*. 2014 Jul 10;43(8):1129–47.
35. Smith MC. The Inerter: A Retrospective. *Annual Review of Control Robotics, and Autonomous Systems*. 2020 May 3;3(1):361–91.
36. Moraes F de H, Silveira M, Gonçalves PJP. On the dynamics of a vibration isolator with geometrically nonlinear inerter. *Nonlinear Dynamics*. 2018;93(3):1325–40.
37. Scheibe F, Smith MC. Analytical solutions for optimal ride comfort and tyre grip for passive vehicle suspensions. *Vehicle System Dynamics*. 2009 Oct 1;47(10):1229–52.

38. Li P, Lam J, Cheung KC. Control of vehicle suspension using an adaptive inerter. *Proceedings of the Institution of Mechanical Engineers, Part D: Journal of Automobile Engineering*. 2015 Mar 19;229(14):1934–43.
39. Wang FC, Liao MK, Liao BH, Su WJ, Chan HA. The performance improvements of train suspension systems with mechanical networks employing inerters. *Vehicle System Dynamics*. 2009 Jul 1;47(7):805–30.
40. Zhu M, Zhang SY, Jiang JZ, Macdonald J, Neild S, Antunes P, et al. Enhancing pantograph-catenary dynamic performance using an inertance-integrated damping system. *Vehicle System Dynamics*. 2022 Jun 3;60(6):1909–32.
41. Li Y, Jiang JZ, Neild S. Inerter-Based Configurations for Main-Landing-Gear Shimmy Suppression. *Journal of Aircraft*. 2016 Oct 14;54(2):684–93.
42. Dong X, Liu Y, Chen MZQ. Application of inerter to aircraft landing gear suspension. In: 2015 34th Chinese Control Conference. 2015. p. 2066–71.
43. De Domenico D, Deastra P, Ricciardi G, Sims ND, Wagg DJ. Novel fluid inerter based tuned mass dampers for optimised structural control of base-isolated buildings. *Journal of Franklin Institute*. 2019 Sep 1;356(14):7626–49.
44. Zhao Z, Zhang R, Jiang Y, Pan C. Seismic response mitigation of structures with a friction pendulum inerter system. *Engineering Structures*. 2019; 193:110–20.
45. Marian L, Giaralis A. Optimal design of a novel tuned mass-damper-inerter (TMDI) passive vibration control configuration for stochastically support-excited structural systems. *Probabilistic Engineering Mechanics*. 2014 Oct 1;38:156–64.
46. Zhang Z, Høeg C. Inerter-enhanced tuned mass damper for vibration damping of floating offshore wind turbines. *Ocean Engineering*. 2021 Mar 1;223.
47. Adhikari S. Inertial amplifier configurations for vibration control and mitigation. *Journal of The Franklin Institute*. 2021.
48. Cheng Z, Palermo A, Shi Z, Marzani A. Enhanced tuned mass damper using an inertial amplification mechanism. *Journal of Sound and Vibration*. 2020 Jun 9;475.
49. Faraj R, Jankowski Ł, Graczykowski C, Holnicki-Szulc J. Can the inerter be a successful shock-absorber? The case of a ball-screw inerter with a variable thread lead. *Journal of Franklin Institute*. 2019;356(14):7855–72.

50. Taniker S, Yilmaz C. Generating ultra wide vibration stop bands by a novel inertial amplification mechanism topology with flexure hinges. *International Journal of Solids and Structures*. 2017 Feb 1;106–107:129–38.
51. Cheng Z, Palermo A, Shi Z, Marzani A. Corrigendum to ‘Enhanced tuned mass damper using an inertial amplification mechanism’ [*Journal of Sound and Vibration* 475 (2020) 115267]. *Journal of Sound and Vibration*. 2020; 481:115433.
52. Yilmaz C, Hulbert GM, Kikuchi N. Phononic band gaps induced by inertial amplification in periodic media. *Physical Review B - Condensed Matter and Material Physics*. 2007 Aug 28;76(5).
53. Li X, Guo M, Dong S. A flex-compressive-mode piezoelectric transducer for mechanical vibration/strain energy harvesting. *Institute of Electrical and Electronics Engineers Transactions on Ultrasonics, Ferroelectrics, and Frequency Control*. 2011 Apr;58(4):698–703.
54. Adhikari S, Banerjee A. Enhanced low-frequency vibration energy harvesting with inertial amplifiers. *Journal of Intelligent Material Systems and Structures*. 2022 Apr 1;33(6):822–38.
55. Fairbairn MW, Moheimani SOR. Quality factor enhancement of an Atomic Force Microscope micro-cantilever using piezoelectric shunt control. In: 2012 Institute of Electrical and Electronics Engineers/American Society of Mechanical Engineers International Conference on Advanced Intelligent Mechatronics. 2012. p. 556–61.
56. Cammarano A, Neild SA, Burrow SG, Inman DJ. The bandwidth of optimized nonlinear vibration-based energy harvesters. *Smart Materials and Structures*. 2014 May 1;23(5):055019.
57. YUAN H, WAN M, YANG Y. Design of a tunable mass damper for mitigating vibrations in milling of cylindrical parts. *Chinese Journal of Aeronautics*. 2019;32(3):748–58.
58. Kolluru K, Axinte D, Becker A. A solution for minimising vibrations in milling of thin walled casings by applying dampers to workpiece surface. *CIRP Annals*. 2013;62(1):415–8.
59. Smith R. Changing the effective mass to control resonance problems. *Sound and Vibration*. 2001; 35:14–7.

60. Haraguchi R, Asai T. Enhanced power absorption of a point absorber wave energy converter using a tuned inertial mass. *Energy*. 2020; 202:117740.
61. Binnig G, Quate CF, Gerber Ch. Atomic Force Microscope. *Physical Review Letters*. 1986 Mar 3;56(9):930–3.
62. Haugstad G. *Atomic Force Microscopy: Understanding Basic Modes and Advanced Applications*. Wiley; 2012.
63. Duman M, Ebner A, Rankl C, Tang J, Chtcheglova LA, Wildling L, et al. Atomic Force Microscopy (AFM) for Topography and Recognition Imaging at Single Molecule Level. In: *Encyclopedia of Biophysics*. Berlin, Heidelberg: Springer Berlin Heidelberg; 2013. p. 102–12.
64. Cumpson P, Clifford C, Portoles J, Johnstone J, Munz M. Cantilever Spring-Constant Calibration in Atomic Force Microscopy. *NanoScience and Technology*. 2008 Jan 1;
65. Rugar D, Hansma P. Atomic Force Microscopy. *Physics Today*. 1990 Oct;43(10):23–30.
66. Eaton P, West P. *Atomic Force Microscopy Peter Eaton and Paul West*. In 2010.
67. Bowen R, Hilal N. *Atomic Force Microscopy in Process Engineering: An Introduction to AFM for Improved Processes and Products*. Elsevier Science; 2009. (Butterworth-Heinemann/ICHEME series).
68. Shinato KW, Huang F, Jin Y. Principle and application of atomic force microscopy (AFM) for nanoscale investigation of metal corrosion. 2020;38(5):423–32.
69. Bettini E, Eriksson T, Boström M, Leygraf C, Pan J. Influence of metal carbides on dissolution behavior of biomedical CoCrMo alloy: SEM, TEM and AFM studies. *Electrochimica Acta*. 2011;56(25):9413–9.
70. Magonov SN. *Atomic Force Microscopy in Analysis of Polymers*. In: *Encyclopedia of Analytical Chemistry*. 2006.
71. Ochoa NA, Prádanos P, Palacio L, Pagliero C, Marchese J, Hernández A. Pore size distributions based on AFM imaging and retention of multidisperse polymer solutes: Characterisation of polyethersulfone UF membranes with dopes containing different PVP. *Journal of Membrane Science*. 2001;187(1):227–37.

72. Roa JJ, Oncins G, Díaz J, Capdevila XG, Sanz F, Segarra M. Study of the friction, adhesion and mechanical properties of single crystals, ceramics and ceramic coatings by AFM. *Journal of the European Ceramic Society*. 2011;31(4):429–49.
73. Roa JJ, Oncins G, Dias FT, Vieira VN, Schaf J, Segarra M. AFM as an alternative for Young's modulus determination in ceramic materials in elastic deformation regime. *Physica C: Superconductivity*. 2011;471(17):544–8.
74. Katan AJ, Dekker C. High-Speed AFM Reveals the Dynamics of Single Biomolecules at the Nanometer Scale. *Cell*. 2011;147(5):979–82.
75. Fotiadis D, Scheuring S, Müller SA, Engel A, Müller DJ. Imaging and manipulation of biological structures with the AFM. *Micron*. 2002;33(4):385–97.
76. Cross SE, Jin YS, Tondre J, Wong R, Rao J, Gimzewski JK. AFM-based analysis of human metastatic cancer cells. *Nanotechnology*. 2008 Sep 24;19(38):384003.
77. Li QS, Lee GYH, Ong CN, Lim CT. AFM indentation study of breast cancer cells. *Biochemical and Biophysical Research Communications*. 2008;374(4):609–13.
78. Farré M, Barceló D. Chapter 1 - Introduction to the Analysis and Risk of Nanomaterials in Environmental and Food Samples. In: Farré M, Barceló D, editors. *Comprehensive Analytical Chemistry*. Elsevier; 2012. p. 1–32.
79. Etzler FM, Drelich J. Chapter 6 - Atomic Force Microscopy for Characterization of Surfaces, Particles, and Their Interactions. In: Kohli R, Mittal KL, editors. *Developments in Surface Contamination and Cleaning*. Oxford: William Andrew Publishing; 2012. p. 307–31.
80. Sansoz F, Gang T. A force-matching method for quantitative hardness measurements by atomic force microscopy with diamond-tipped sapphire cantilevers. *Ultramicroscopy*. 2010;111 1:11–9.
81. Custance O, Perez R, Morita S. Atomic force microscopy as a tool for atom manipulation. *Nature Nanotechnology*. 2009;4(12):803–10.
82. Bamidele J, Lee SH, Kinoshita Y, Turanský R, Naitoh Y, Li YJ, et al. Vertical atomic manipulation with dynamic atomic-force microscopy without tip change via a multi-step mechanism. *Nature Communications*. 2014;5(1):4476.

83. Marinello F, Balcon M, Schiavuta P, Carmignato S, Savio E. Thermal drift study on different commercial scanning probe microscopes during the initial warming-up phase. *Measurement Science and Technology*. 2011 Aug 8; 22:094016.
84. Schumacher Z, Miyahara Y, Aeschmann L, Grütter P. Improved atomic force microscopy cantilever performance by partial reflective coating. *Beilstein journal of nanotechnology*. 2015; 6:1450–6.
85. Nasrabadi HM, Mahdavi M, Moheimani SOR. Q Control of an AFM Microcantilever With Double-Stack AlN Sensors and Actuators. *Institute of Electrical and Electronics Engineers Sensors Journal*. 2022;22(5):3957–64.
86. Fairbairn M, Moheimani SOR. Resonant control of an atomic force microscope micro-cantilever for active Q control. *Review of Scientific Instruments*. 2012 Aug;83(8):083708.
87. Dong X, Peng Z, Zhang W, Hua H, Meng G. Research on Spillover Effects for Vibration Control of Piezoelectric Smart Structures by ANSYS. Sun W, editor. *Mathematical Problems in Engineering* 2014; 2014:870940.
88. Ahmed A, Azam A, Wang Y, Zhang Z, Li N, Jia C, et al. Additively manufactured nano-mechanical energy harvesting systems: advancements, potential applications, challenges and future perspectives. *Nano Convergence*. 2021 Dec 1;8(1):37.
89. Shi B, Li Z, Fan Y. Implantable Energy-Harvesting Devices. *Advanced Materials*. 2018 Nov;30(44):1801511.
90. Cojocariu B, Hill A, Escudero A, Xiao H, Wang X. Piezoelectric Vibration Energy Harvester: Design and Prototype. In: *Volume 12: Vibration, Acoustics and Wave Propagation*. American Society of Mechanical Engineers; 2012. p. 451–60.
91. Páez-Montoro A, García-Valderas M, Olías-Ruíz E, López-Ongil C. Solar Energy Harvesting to Improve Capabilities of Wearable Devices. *Sensors*. 2022 May 23;22(10):3950.
92. Wang H, Park JD, Ren ZJ. Practical Energy Harvesting for Microbial Fuel Cells: A Review. *Environmental Science & Technology*. 2015 Mar 17;49(6):3267–77.
93. Wang L, Fei Z, Qi Y, Zhang C, Zhao L, Jiang Z, et al. Overview of Human Kinetic Energy Harvesting and Application. *ACS Applied Energy Materials*. 2022 Jun 27;5(6):7091–114.

94. Abdin Z, Alim MA, Saidur R, Islam MR, Rashmi W, Mekhilef S, et al. Solar energy harvesting with the application of nanotechnology. *Renewable and Sustainable Energy Reviews*. 2013 Oct; 26:837–52.
95. Kishore R, Priya S. A Review on Low-Grade Thermal Energy Harvesting: Materials, Methods and Devices. *Materials*. 2018 Aug 14;11(8):1433.
96. Wonoyudo BD, Febrawi T. Electrical Energy from Vibration of a Washing Machine. *Applied Mechanics and Materials*. 2014 Jan; 493:349–53.
97. Qi L, Pan H, Pan Y, Luo D, Yan J, Zhang Z. A review of vibration energy harvesting in rail transportation field. *iScience*. 2022 Mar;25(3):103849.
98. Waterbury AC, Wright PK. Vibration energy harvesting to power condition monitoring sensors for industrial and manufacturing equipment. *Proceedings of the Institution of Mechanical Engineers, Part C: Journal of Mechanical Engineering Science*. 2013 Jun 17;227(6):1187–202.
99. Williams CB, Yates RB. Analysis of a micro-electric generator for microsystems. *Sensors and Actuators A: Physical*. 1996 Mar;52(1–3):8–11.
100. Mohanty A, Parida S, Behera RK, Roy T. Vibration energy harvesting: A review. *Journal of Advanced Dielectrics*. 2019 Aug 8;09(04):1930001.
101. Carlson L, Cloutier T, Kalka-Riffel A, Patel K, Pawlak K. Harvesting Vibrational Energy. 2019 Mar.
102. Wei C, Jing X. A comprehensive review on vibration energy harvesting: Modelling and realization. *Renewable and Sustainable Energy Reviews*. 2017 Jul; 74:1–18.
103. Florentino HR, Freire RCS, Catunda SYC, Sa AVS, Atunda DG. Energy harvesting circuit using variable capacitor for power systems. In: 2011 Institute of Electrical and Electronics Engineers International Instrumentation and Measurement Technology Conference. Institute of Electrical and Electronics Engineers; 2011. p. 1–4.
104. De Pasquale G. Energy harvesters for powering wireless systems *. In: *Handbook of Mems for Wireless and Mobile Applications*. Woodhead Publishing Series in Electronic and Optical Materials; 2013. p. 345–400.
105. Muscat A, Bhattacharya S, Zhu Y. Electromagnetic Vibrational Energy Harvesters: A Review. *Sensors*. 2022 Jul 25;22(15):5555.

106. Gao C, Zeng Z, Peng S, Shuai C. Magnetostrictive alloys: Promising materials for biomedical applications. *Bioactive Materials*. 2022 Feb; 8:177–95.
107. Bhatnagar V, Owende P. Energy harvesting for assistive and mobile applications. *Energy Science & Engineering*. 2015 May 17;3(3):153–73.
108. Xue T, Williams S, Rantz R, Halim MA, Roundy S. System Modeling, Characterization, and Design Considerations for Generators in Commercial Watches With Application to Energy Harvesting for Wearables. *Institute of Electrical and Electronics Engineers/American Society of Mechanical Engineers Transactions on Mechatronics*. 2018 Oct;23(5):2515–24.
109. Xie F, Qian X, Li N, Cui D, Zhang H, Xu Z. An experimental study on a piezoelectric vibration energy harvester for self-powered cardiac pacemakers. *Annals of Translational Medicine*. 2021 May;9(10):880–880.
110. Sun H, Yin M, Wei W, Li J, Wang H, Jin X. MEMS based energy harvesting for the Internet of Things: a survey. *Microsystem Technologies*. 2018 Jul 7;24(7):2853–69.
111. Xingfa Shen, Zhi Wang, Youxian Sun. Wireless sensor networks for industrial applications. In: *Fifth World Congress on Intelligent Control and Automation (Institute of Electrical and Electronics Engineers Cat No04EX788)*; p. 3636–40.
112. Lu Y, Savvaris A, Tsourdos A, Bevilacqua M. Vibration energy harvesters for wireless sensor networks for aircraft health monitoring. In: *2016 Institute of Electrical and Electronics Engineers Metrology for Aerospace*. 2016. p. 25–32.
113. Titirici M. Sustainable Batteries—Quo Vadis? *Advanced Energy Materials*. 2021 Mar 27;11(10):2003700.
114. Cheng C, Drummond R, Duncan SR, Grant PS. Extending the energy-power balance of Li-ion batteries using graded electrodes with precise spatial control of local composition. *Journal of Power Sources*. 2022 Sep; 542:231758.
115. Hu X, Xu L, Lin X, Pecht M. Battery Lifetime Prognostics. *Joule*. 2020 Feb;4(2):310–46.
116. Muthu B, Kamalanathan A. Impact of Used Battery Disposal in the Environment. 2021 Nov 2;5: 1276–86.

117. Yildirim T, Ghayesh MH, Li W, Alici G. A review on performance enhancement techniques for ambient vibration energy harvesters. *Renewable and Sustainable Energy Reviews*. 2017 May; 71:435–49.
118. Romero-Bastida M, López JM. Efficient harmonic oscillator chain energy harvester driven by colored noise. *Scientific Reports*. 2020 Aug 31;10(1):14306.
119. Ibrahim P, Arafa M, Anis Y. An Electromagnetic Vibration Energy Harvester with a Tunable Mass Moment of Inertia. *Sensors*. 2021 Aug 20;21(16):5611.
120. Dong L, Grissom MD, Prasad MG, Fisher FT. Application of mechanical stretch to tune the resonance frequency of hyperelastic membrane-based energy harvesters. *Sensors and Actuators A: Physical*. 2016 Dec; 252:165–73.
121. Ramlan R, Brennan MJ, Mace BR, Kovacic I. Potential benefits of a non-linear stiffness in an energy harvesting device. *Nonlinear Dynamics*. 2010 Mar 28;59(4):545–58.
122. Zhang B, Li B, Fu S, Mao Z, Ding W. Vortex-Induced Vibration (VIV) hydrokinetic energy harvesting based on nonlinear damping. *Renewable Energy*. 2022 Aug; 195:1050–63.
123. Kouritem SA, Bani-Hani MA, Beshir M, Elshabasy MMYB, Altabay WA. Automatic Resonance Tuning Technique for an Ultra-Broadband Piezoelectric Energy Harvester. *Energies (Basel)*. 2022 Oct 3;15(19):7271.
124. Siddiqui SA, Ahmad A, Siddiqui AA, Chaturvedi P. Stability Analysis of a Cantilever Structure using ANSYS and MATLAB. In: 2021 2nd International Conference on Intelligent Engineering and Management. Institute of Electrical and Electronics Engineers; 2021. p. 7–12.
125. Amazon [Internet]. [place unknown] Hand @ 25mm 12g Lead Weights, Pack of 20 [product] [cited 2023 Feb 7] Available from: <https://www.amazon.co.uk/HAND-25mm-Lead-Weights-Pack/dp/B00CXT9ZKM>
126. Xu T, Li Y, Lai T, Zheng J. A simplified design method of tuned inerter damper for damped civil structures: Theory, validation, and application. *Structural Control and Health Monitoring*. 2021 Sep 26;28(9).